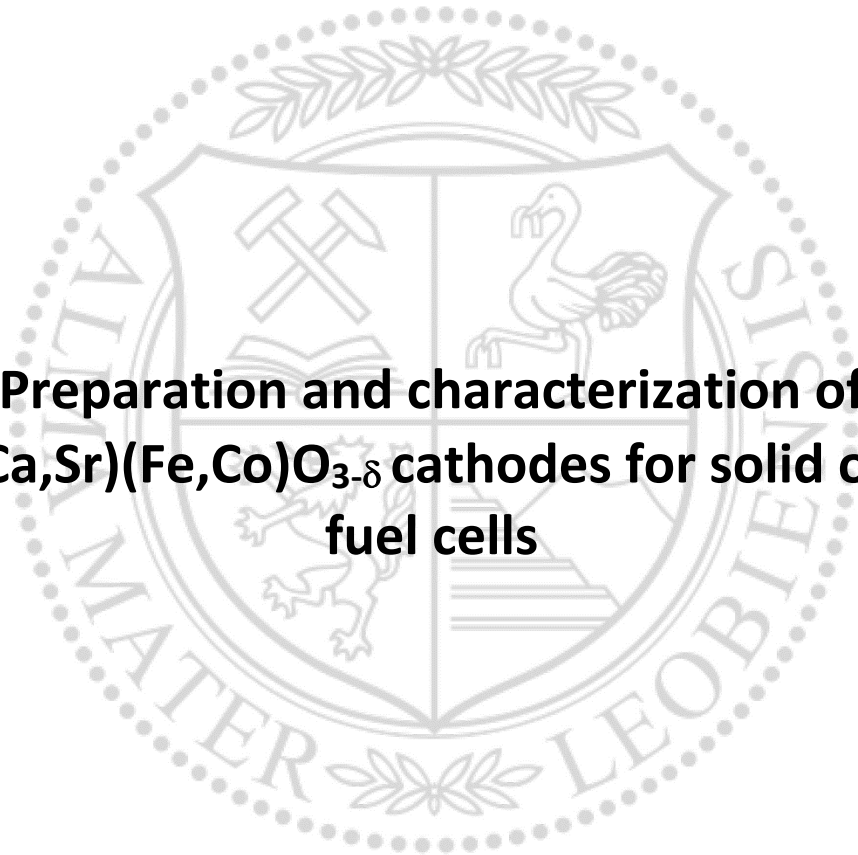




Chair of Physical Chemistry

Master Thesis



**Preparation and characterization of
(La,Ca,Sr)(Fe,Co)O_{3-δ} cathodes for solid oxide
fuel cells**

Mario Karl Micu-Budisteanu, BSc

März 2021

This Master Thesis was supervised by Assoc. Prof. DI Dr. mont. Edith Bucher and DI Dr. mont. Christian Berger from the Chair of Physical Chemistry at Montanuniversitaet Leoben, Austria, and by Hon.-Prof. Dr.-Ing. Norbert H. Menzler and Dr. rer. nat. Christian Lenser from the Institute of Energy and Climate Research - Materials Synthesis and Processing (IEK-1) at Forschungszentrum Jülich, Germany.

Danksagung

Einleitend möchte ich meinen Dank den Betreuern an der Montanuniversität Leoben aussprechen, Frau Assoz. Prof. Dipl.-Ing. Dr. mont. Edith Bucher und Herrn Dipl.-Ing. Dr. mont. Christian Berger, die mich seit meiner Bakkalaureatsarbeit am Lehrstuhl für Physikalische Chemie unterstützten sowie förderten und immer eine offene Tür für meine Anliegen aller Art hatten. Dabei darf ich Christian mit Freude nicht nur einen Mentor, sondern auch einen Freund nennen.

Ebenso danke ich Herrn Univ.-Prof. Dipl.-Ing. Dr. techn. Werner Sitte, dass er mir die Arbeit am Lehrstuhl für Physikalische Chemie ermöglichte.

Weiters gilt mein Dank den Betreuern am Forschungszentrum Jülich, Herrn Hon.-Prof. Dr.-Ing. Norbert H. Menzler und Herrn Dr. rer. nat. Christian Lenser, die mir tatkräftig mit Anregungen und Ideen halfen und deren Einschätzungen immer zielführend waren, sowohl in fachlicher als auch in persönlicher Hinsicht. Ebenfalls möchte ich Herrn Werner Herzhof für seine Hilfe danken.

Mein herzlichster Dank gilt meinen Eltern Michael und Dagmar, ohne die ich diese Zeilen nicht schreiben könnte und die nicht nur mein Studium, sondern auch meine Persönlichkeit und meine Interessen trotz allem immer förderten und mir ein sorgenfreies Studium ermöglichten.

In dieser Danksagung darf auch Lisa nicht fehlen, der ich seit vielen Jahren verbunden bin und die trotz Entfernung doch immer bei mir war. Niemand beschreibt diesen Seelenzustand besser als der große Ernst Jünger: „Dass ein einziger Mensch, in der Tiefe erfasst und aus ihr spendend, uns mehr gewährt und größeren Reichtum schenkt, als Cäsar, als Alexander je erobern konnten, das wurde mir offenbar. Dort ist unser Königreich, die beste der Monarchien, die beste Republik. Dort ist unser Garten, unser Glück.“

Eidesstattliche Erklärung

Ich erkläre an Eides statt, dass ich diese Arbeit selbständig verfasst, andere als die angegebenen Quellen und Hilfsmittel nicht benutzt, und mich auch sonst keiner unerlaubten Hilfsmittel bedient habe.

Ich erkläre, dass ich die Richtlinien des Senats der Montanuniversität Leoben zu "Gute wissenschaftliche Praxis" gelesen, verstanden und befolgt habe.

Weiters erkläre ich, dass die elektronische und gedruckte Version der eingereichten wissenschaftlichen Abschlussarbeit formal und inhaltlich identisch ist.

Affidavit

I declare on oath that I wrote this thesis independently, did not use other than the specified sources and aids, and did not otherwise use any unauthorized aids.

I declare that I have read, understood, and complied with the guidelines of the senate of the Montanuniversitaet Leoben for "Good Scientific Practice".

Furthermore, I declare that the electronic and printed version of the submitted thesis are identical, both, formally and with regard to content.

Datum

Unterschrift

„Das flücht'ge Lob, des Tages Ruhm,
Magst du dem Eitlen gönnen,
Das aber sei dein Heiligtum:
Vor dir bestehen können.“

Theodor Fontane

Table of Content

1. Motivation	9
2. Introduction	10
3. Theory	11
3.1. Fuel Cells	11
3.2. Solid Oxide Fuel Cells	13
3.3. Perovskites	14
4. Experimental	15
4.1. Synthesis and Powder Processing	15
4.2. Screen Printing	17
4.3. Preparation of Dense Samples	22
4.4. Button Cells	23
4.5. 50x50 mm ² Anode Supported Cells	23
4.6. Crystal Structure and Chemical Composition	24
4.6.1 X-ray Diffraction and Rietveld Refinement	24
4.6.2 Inductively Coupled Plasma Atomic Emission Spectroscopy	25
4.7. Thermal Properties	26
4.7.1 Thermal Expansion Coefficient	26
4.7.2 Differential Scanning Calorimetry	27
4.7.3 Combustion Analysis	28
4.8. Electrical Properties	29
4.8.1 Electronic Conductivity	29
4.9. Oxygen Exchange Kinetics	31
4.9.1 Chemical Surface Exchange Coefficient and Chemical Diffusion Coefficient of oxygen	32
4.10. Electrochemical Properties	33
4.10.1 Electrochemical Impedance Spectroscopy	33
5. Results and Discussion	36
5.1. Crystal Structure	36
5.2. Thermal Properties	41
5.3. Electronic Conductivity	46
5.4. Oxygen Exchange Kinetics	47
5.5. Oxygen Non-Stoichiometry	49
5.6. Electrochemical Properties	51
5.6.1 La _{0.8} Ca _{0.2} FeO _{3-δ}	51
5.6.2 La _{0.8} Ca _{0.2} Fe _{0.8} CO _{0.2} O _{3-δ}	58
5.6.3 La _{0.6} Ca _{0.2} Sr _{0.2} FeO _{3-δ}	60
5.6.4 Overview of cell performance	64
6. Summary and Conclusion	66
7. Outlook	66
8. Literature	67
9. Appendix	72
9.1. Synthesis and Powder	72
9.2. Screen printing	74

Kurzfassung

In dieser Arbeit werden neuartige elektronen- und sauerstoffionenleitende Kathodenmaterialien für Festelektrolytbrennstoffzellen hinsichtlich Kristallstruktur, sowie Masse- und Ladungstransporteigenschaften untersucht. Aktuelle Arbeiten zeigen, dass Verbindungen aus der Reihe $(\text{La,Ca})\text{FeO}_{3-\delta}$ eine äußerst rasche Sauerstoffaustauschkinetik und hohe Langzeitstabilität unter kritischen Betriebsbedingungen (z.B. SO_2 -Vergiftung) besitzen. Durch gezielte Substitution mit Sr bzw. Co sollen ausgehend von $\text{La}_{0.8}\text{Ca}_{0.2}\text{FeO}_{3-\delta}$ neue Verbindungen hergestellt und charakterisiert werden. In Kooperation mit dem Forschungszentrum Jülich (FZJ) sollen Zellen mit Lufterlektroden aus den an der Montanuniversität Leoben (MUL) hergestellten Kathodenmaterialien präpariert und elektrochemisch charakterisiert werden.

Neben dem auf Materialebene bereits gut untersuchten Perowskit $\text{La}_{0.8}\text{Ca}_{0.2}\text{FeO}_{3-\delta}$ (LCF82), der eine sehr rasche Sauerstoffaustauschkinetik und gute Stabilität gegenüber SO_2 -Vergiftung besitzt, sollen Materialien mit Sr- bzw. Co-Substitution untersucht werden. Die Verbindungen $\text{La}_{0.6}\text{Ca}_{0.2}\text{Sr}_{0.2}\text{FeO}_{3-\delta}$ (LCSF622) und $\text{La}_{0.8}\text{Ca}_{0.2}\text{Fe}_{0.8}\text{Co}_{0.2}\text{O}_{3-\delta}$ (LCFC8282) werden in Hinblick auf Phasenreinheit und Kristallstruktur mittels XRD und Rietveld-Verfeinerung charakterisiert. Die thermischen Ausdehnungskoeffizienten werden mittels Dilatometrie bestimmt. Weiters wird die elektronische Leitfähigkeit und die Sauerstoffaustauschkinetik mittels dc-Leitfähigkeits- und dc-Leitfähigkeitsrelaxationsmessungen untersucht. Anschließend werden Siebdruckpasten hergestellt und rheologisch optimiert, um damit poröse Elektroden auf symmetrischen sowie anodengestützten Zellen herzustellen. Die Zellen werden mittels elektrochemischer Impedanzspektroskopie und Strom-Spannungskennlinien charakterisiert. Post-mortem Analysen an den getesteten Zellen geben Aufschluss über das Sinterverhalten der porösen Elektroden, deren Mikrostruktur und die Schichtanhaftung am Elektrolyten.

Abstract

In this work, novel mixed ionic-electronic conducting cathode materials for solid oxide fuel cells are investigated with respect to crystal structure, as well as mass- and charge transport properties. Recent studies on compounds from the series $(\text{La,Ca})\text{FeO}_{3-\delta}$ show that these materials exhibit exceptionally fast oxygen exchange kinetics and high long-term stability under critical operating conditions (e.g. SO_2 -poisoning). New compounds, obtained by substitution of $\text{La}_{0.8}\text{Ca}_{0.2}\text{FeO}_{3-\delta}$ with Sr or Co, are synthesized and characterized. In cooperation with Forschungszentrum Jülich (FZJ), cells with air electrodes fabricated from materials developed at Montanuniversität Leoben (MUL) are prepared and electrochemically characterized.

In addition to the perovskite $\text{La}_{0.8}\text{Ca}_{0.2}\text{FeO}_{3-\delta}$ (LCF82), which has been well characterized with regard to material properties and exhibits fast oxygen exchange kinetics and good stability against SO_2 -poisoning, materials with Sr- or Co-substitution are investigated. The compounds $\text{La}_{0.6}\text{Ca}_{0.2}\text{Sr}_{0.2}\text{FeO}_{3-\delta}$ (LCSF622) and $\text{La}_{0.8}\text{Ca}_{0.2}\text{Fe}_{0.8}\text{Co}_{0.2}\text{O}_{3-\delta}$ (LCFC8282) are studied with respect to phase purity and crystal structure by means of XRD and Rietveld refinement. Thermal expansion coefficients are determined by dilatometry. Further, the electronic conductivity and the oxygen exchange kinetics are investigated by means of dc-conductivity and dc-conductivity relaxation measurements. Subsequently, screen-printing pastes are fabricated and rheologically optimized, in order to manufacture porous electrodes on symmetrical and anode-supported cells. The cells are characterized by electrochemical impedance spectroscopy and current-voltage curves. Post-mortem analyses provide further insights into the sintering behavior of the porous electrodes, their microstructure, and layer adhesion on the electrolyte.

1. Motivation

Global power consumption has increased annually throughout the last decades, reaching a total primary energy supply of 162 PWh in 2017, which corresponds to 14.000 million tons of oil equivalent (Mtoe), whereas 113 PWh, or 10.000 Mtoe, reached final energy consumption. This difference is due to the losses to other forms of energy during the process of refinement into usable forms of energy, and to the transport from the initial location of supply to customers. In total, coal (38%) and natural gas (23%) still represent the main energy carriers for energy conversion. Out of this 113 PWh, 24 PWh were consumed in form of electricity [1]. Considering the increasing energy demand, the ambitious goal set by policy makers in form of the Paris Agreement (PA) and its geographical subsidiaries, seems utterly ambitious by taking into consideration that Art. 2 § 1 of the PA is legally binding but not directly enforceable, which is in contradiction to its predecessor, the Kyoto protocol [2] [3] [4].

In order to provide the above-mentioned energy demand, the currently predominating process is the combustion of hydrocarbons or coal-fired power stations. Although nowadays highly efficient internal combustion engines or turbines are used, the peak efficiency is limited by the Carnot-cycle. Furthermore, the combustion of hydrocarbons inevitably produces CO₂. At this point, electrochemical energy conversion is virtue, whereby in this case one needs to consider if the hydrogen can be labelled as green, blue or black, depending on the treatment of the CO₂ by-product of the process [5]. Although in terms of overall efficiency and price, battery systems as stationary power systems or mobile units lead the way, the problem of charging and energy density remains. Given this, fuel cell systems represent a promising alternative option.

Solid oxide fuel cell stack-lifetimes of 100,000 h have already been demonstrated under lab-conditions [6]. However, the vulnerability of SOFCs to sulfur, chromium and other critical impurities persist and development of novel electrode materials with improved resistance to surface poisoning remains a challenge. The results on the base-material presented in this work, La_{0.8}Ca_{0.2}FeO_{3-δ} (LCF82), show that both at 700°C in fresh as well as in degraded state (O₂-Ar with 2 ppm SO₂ atmosphere), the chemical surface exchange coefficient k_{chem} exhibits higher values than comparable state-of-the-art La_{0.6}Sr_{0.4}CoO_{3-δ} (LSC) cathodes [7]. In the present work, two novel compounds derived from LCF82 – La_{0.8}Ca_{0.2}Fe_{0.8}Co_{0.2}O_{3-δ} (LCFC8282) and La_{0.6}Sr_{0.2}Ca_{0.2}FeO_{3-δ} (LCSF622) – are investigated, in order to determine if substitution can further enhance reliability and electrochemical properties.

2. Introduction

One of the primary purposes of the cathode of an SOFC is the oxygen reduction reaction, which proceeds via the steps of surface adsorption of molecular oxygen, dissociation, reduction and incorporation of oxygen ions into the bulk. High porosity within the cathode microstructure is preferable, as better distribution of molecular oxygen from the feed gas can take place and this increased gas-transport is crucial to avoid energy losses caused by concentration polarization. High electronic conductivity within the cathode material is necessary, on the one hand since electrons participate in the oxygen reduction, and on the other hand to minimize ohmic loss. In general, electrical conductivities greater than 100 S cm^{-1} are preferred [8]. Further, the thermal expansion coefficient (TEC) of the cathode material should be similar to those of the electrolytes and interconnectors material, as well as other components. The absence of chemical interaction with mentioned components is also vital in order to avoid cell degradation due to the formation of electrically isolating secondary phases. The following types of cathode materials partially fulfil these demands: Noble-metal-based cathodes, perovskite-based cathodes, layered perovskite-based cathodes, spinel oxides and doped ceria [9].

In contrast to noble-metal-based cathodes, perovskite-based cathodes such as $\text{La}_{0.8}\text{Sr}_{0.2}\text{MnO}_{3-\delta}$ show good performance, structural stability and chemical compatibility with zirconia-based electrolytes ($(\text{ZrO}_2)_{0.92}(\text{Y}_2\text{O}_3)_{0.08}$, 8-YSZ) [9]. Due to this, $\text{La}_{0.8}\text{Sr}_{0.2}\text{MnO}_{3-\delta}$ cathodes are nowadays among the most popular materials for commercialized high-temperature SOFCs. However, the tendency towards intermediate-temperature fuel cells reveals that the electrochemical activity in the temperature range around 700°C is not satisfying. For example, a given $\text{La}_{0.8}\text{Sr}_{0.2}\text{MnO}_{3-\delta}$ electrode, which shows a polarization resistance of $0.39 \text{ }\Omega\text{cm}^2$ at 900°C , shows a sharply increased value of $55.7 \text{ }\Omega\text{cm}^2$ at 700°C [10]. It is suggested that for practical application and economic attractiveness, the electrode should have an area-specific electrode polarization resistance of less than $0.15 \text{ }\Omega\text{cm}^2$ at the application temperature, which poses a considerable challenge for operation under intermediate temperature conditions [11]. Mixed ionic-electronic conducting perovskites such as $\text{La}_{0.6}\text{Sr}_{0.4}\text{Co}_{0.2}\text{Fe}_{0.8}\text{O}_{3-\delta}$ (LSCF6428) are cost-efficient and stable – in combination with high catalytic activity for oxygen reduction, especially at reduced temperatures around $700\text{-}800^\circ\text{C}$.

In this present work, mixed conducting perovskite-based cathodes are investigated. The base material is LCF82, which is already well characterized [12]. In this material, the electronic conductivity exceeds the above mentioned necessary 100 Scm^{-1} , but is still significantly below the values for LSCF6428. In terms of the oxygen surface exchange coefficients, LCF82 can be compared to LSCF6428, whereas overall cell performance of LSCF6428 exceeds LCF82. Also presented in this work are two novel compounds derived from the base material – LCFC8282 and LCSF622. In the latter, the aim is to introduce more oxygen vacancies by incorporation of higher concentrations of divalent ions (Sr^{2+} and Ca^{2+}) on trivalent lattice positions (La^{3+}) and therefore improve the oxygen surface exchange coefficients, oxygen diffusion coefficients, and ionic conductivity. In case of LCFC8282, we substituted Fe-ions with Co-ions. The underlying concept is on the one hand to improve electronic conductivity, and on the other hand, to improve the sintering activity since Co is known to be a very sinter-active metal [13].

The powder synthesis, as well as determination of the fundamental electrical and thermal material properties and the oxygen exchange kinetics were carried out at Montanuniversitaet Leoben. The fabrication of screen printing pastes, optimization of the screen printing parameters, and the manufacturing and characterization of button- and $50\times 50 \text{ mm}^2$ cells were conducted at Forschungszentrum Jülich GmbH (FZJ) in Jülich, Germany

3. Theory

3.1. Fuel Cells

A fuel cell is an electrochemical cell consisting of an anode, cathode and an electrolyte, which separates the two electrodes. The electrolyte can be designed as a semi-permeable membrane and can only be permeable for one type of ion. The overall reaction of the fuel cell is



and has a theoretical voltage of 1.229 V at 25°C when liquid H₂O is formed. This reaction generates heat and electrical energy, the latter of which can be tapped as voltage. Since this process is electrochemical, the efficiency is not limited by the Carnot process in contrast to combustion engines, which means that it can be significantly increased. Figure 1 shows a schematic diagram of the losses occurring in a fuel cell [14].

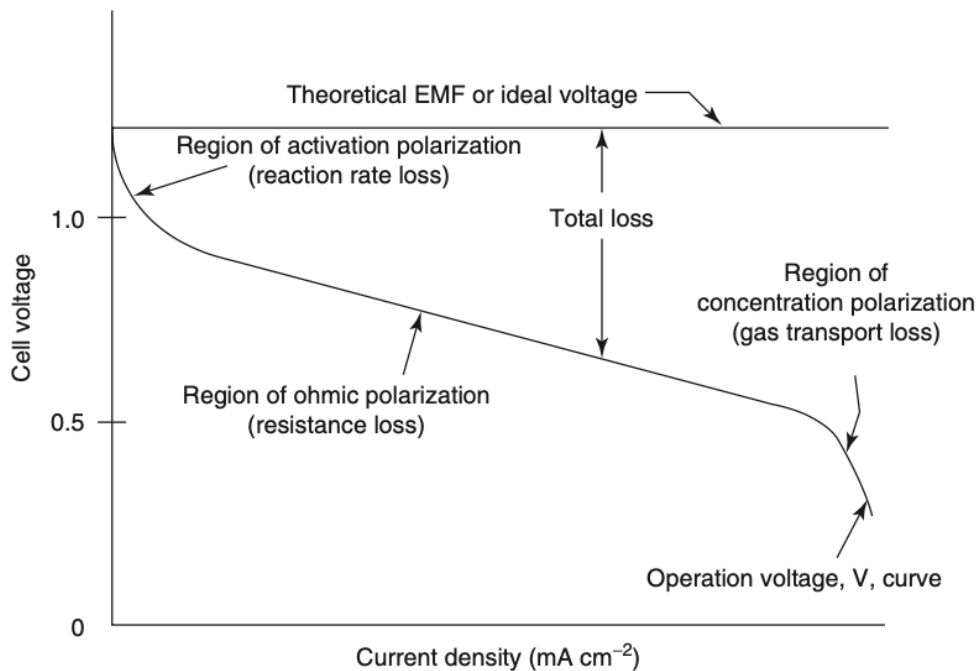


Figure 1: Schematic of the V–I curve for a typical solid oxide fuel cell (SOFC), which shows open-circuit voltage (OCV; theoretical EMF), activation polarization loss, concentration polarization loss, and ohmic loss; EMF represents the electromotive force [14].

As can be seen in the figure above, activation losses dominate in the range of small electrical current densities, and are caused by the required activation energy of the exothermic cell reaction and the electrode processes. The following methods are available to minimize these losses [15]:

- Catalysts
- Increase of the electrode area
- Temperature increase

Based on the last point, fuel cells are categorized by their required operating temperature, resulting in the following classification:

- Low temperature fuel cells up to approx. 100°C
- Medium temperature fuel cells up to approx. 200°C
- High temperature fuel cells above 600°C

Table 1 shows the most common types of fuel cells, their operating temperature, the type of ions transported and their application [15].

Table 1: Properties of different types of fuel cells [15]

Type	Mobile ion	Operating temperature	Application
Alkaline (AFC)	OH ⁻	50-200°C	Use in spacecraft, e.g. Apollo
Proton exchange Membrane (PEMFC)	H ⁺	30-100°C	Vehicles and other mobile applications; Combined heat and power system (CHP)
Direct methanol (DMFC)	H ⁺	20-90°C	Mobile electronic systems with low power for long periods
Phosphoric acid (PAFC)	H ⁺	220°C	Large quantity of 200-kW CHP systems in use
Molten carbonate (MCFC)	CO ₃ ²⁻	650°C	Medium to large CHP systems in the MW range
Solid oxide (SOFC)	O ²⁻	500-1000°C	All types of CHP systems; 2 kW to MW range

3.2. Solid Oxide Fuel Cells

Solid oxide fuel cells (SOFCs) are high-temperature fuel cells with operating temperatures in the range of 500-1000°C, using a ceramic electrolyte (oxygen ion conductor). The high operating temperature leads to special demands regarding gas tightness, ageing and high temperature corrosion of metallic interconnectors. The electrolyte of this cell type consists of an oxygen-ion conducting ceramic, which must at the same time be an electronic insulator. This cell can be used with hydrogen as well as methane and other hydrocarbons as fuel. However, when operating with hydrocarbons and insufficient humidification, carbon produced at the anode is a problem in continuous operation. Figure 2 shows a schematic diagram of how a solid oxide fuel cell works, whereby it is based on oxygen ion conduction [14]:

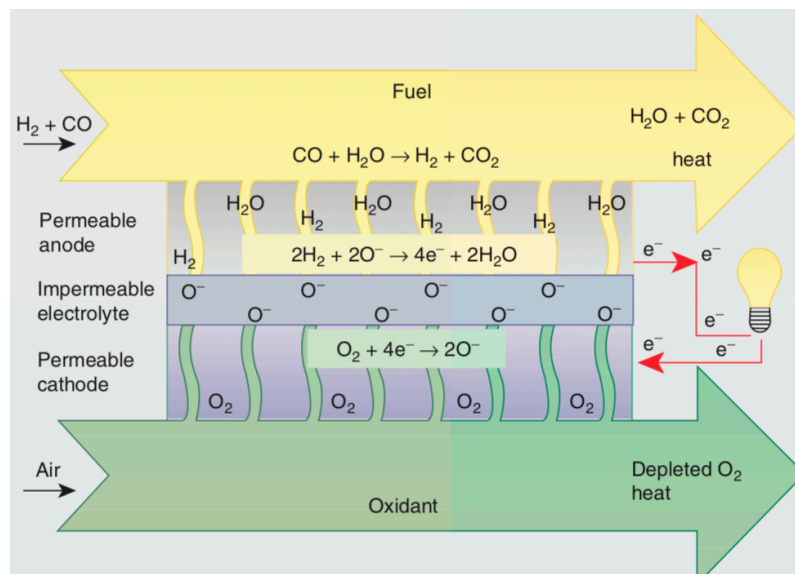


Figure 2: Operating principle of an SOFC [14].

If the cathode material exhibits electronic conductivity and negligible ionic conductivity (e.g. LSM), pores, cathode and electrolyte act as carriers of oxygen, electrons and vacant oxygen sites, respectively. Therefore, the length of the triple phase boundary (TPB) limits the oxygen reduction process. If the material shows mixed ionic-electronic conductivity, such as LSCF and the materials studied in this work, active sites spread also to the cathode surface. From there, oxygen can be transferred into the bulk and the electrolyte through the cathode-electrolyte interface. The microstructure influences this reaction since diatomic oxygen needs to be converted to an intermediate form. For cathodes based on perovskite materials, Figure 3 shows three possible paths for oxygen reduction: the cathode surface path, the cathode volume (bulk) path and the electrolyte surface path, which was described by Fleig [16].

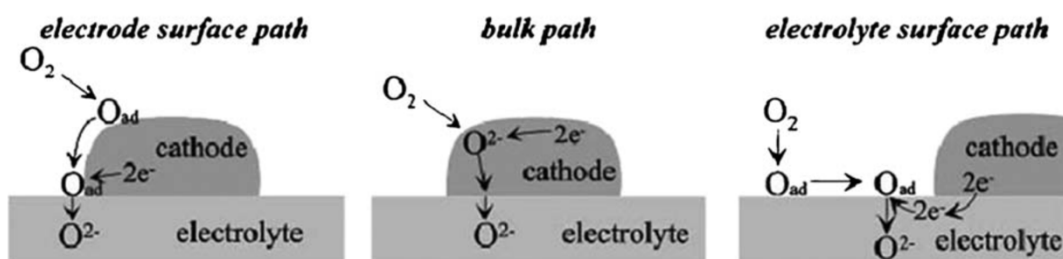


Figure 3: Possible reaction paths in perovskite cathodes for SOFCs [16].

3.3. Perovskites

Perovskites are a class of solids based on the structure ABO_3 , where A and B are metal ions and O is an anion (usually oxygen) or semi-metal. Due to their ionic nature, the electroneutrality condition must be fulfilled. If the partial charges of the ions are given by q_A , q_B and q_O , the rule

$$q_A + q_B = -3q_O \quad \text{Equation 3-2}$$

ensures charge neutrality [17].

Figure 4 shows the structure of $La_{0.8}Ca_{0.2}Fe_{0.8}Co_{0.2}O_{3-\delta}$ (LCFC8282) as an example of a perovskite-type oxide. Here, the blue octahedra represent the six-fold coordination of O-ions (shown in red) around Fe- and Co-ions. La- and Ca-ions are found at the green/blue positions between the $Fe(Co)O_6$ octahedrons. The black line represents the unit cell.

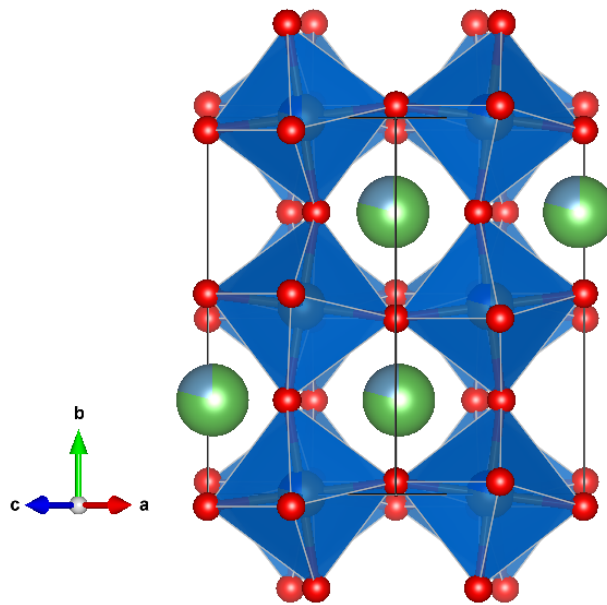


Figure 4: Crystal structure of low-temperature phase of LCFC8282 (perovskite) with the corresponding unit cell [57].

4. Experimental

4.1. Synthesis and Powder Processing

The materials, which are presented in this work, were synthesized using a sol-gel route. For sol-gel syntheses, several methods are available, including

- Pechini method
- Citric acid ethylenediaminetetraacetate method (CA-EDTA method)
- Glycine-nitrate method

Sol-gel methods utilize wet chemical processes and are based on the formation of a solid product from a solution (“sol”) of the reactants (precursors) from which a network of sol particles is formed by hydrolysis and condensation reactions. The resulting viscous state is called “gel”. By this method, it is possible to achieve a much smaller particle sizes in the powder and less porosity after subsequent sintering than by classical ceramic methods such as the solid oxide route [18]. The precursors are usually nitrates or acetates of metal ions [19].

In the course of this work, the CA-EDTA route was chosen since it allows larger quantities (>30 g) to be produced from the metal nitrates without prior titration of the stock solutions. This method is based on the complexation of cations in an aqueous-organic medium and uses inexpensive precursors such as citric acid for polymerization.

EDTA is used to form stable gels with several cations, since it can complex cations. For this purpose, protons are removed from the EDTA by changing the pH value with 25% NH₃, which is why it reacts with cations (i.e. Ba²⁺, Ca²⁺ etc.) and binds them to itself. This transforms the gel into a polymer with a homogeneous distribution of cations. The organic fraction is then eliminated at temperatures of up to 300 °C, forming reactive oxides.

Unlike the CA-EDTA method, the Pechini method uses the ability of α -hydroxycarboxylic acids to form chelate complexes. When these chelate complexes are heated in a polyhydroxy alcohol such as ethylene glycol, polycondensation begins in order to form a polyester [18]. In the glycine-nitrate method, the processes are similar to the CA-EDTA method, but instead of EDTA, glycine takes over the complexation of the cations.

In the last step of all sol-gel synthesis routes, the formed gel, in which the cations are homogeneously distributed, is heated until spontaneous ignition. In the raw ash resulting from combustion, the product (oxide) is already present in mostly amorphous or even partially crystalline form. All synthesized compounds as well as the corresponding reactants can be found in Table 20 and Table 21 in the appendix.

The next step in powder processing is calcination, a process whose purpose is to decarbonize or dehydrate and remove volatile components. A temperature below the melting point of the product phase is chosen, but above the decomposition temperature of the phases to be removed. Above certain temperatures, CO₂ is always formed as reaction gas, which is why calcination vessels in the furnace must not be tightly sealed. The calcination temperature for all of our phases is 1000°C, whereas the calcination time is 4 h and the temperature ramps are 5 K/min for heating up as well as for cooling down. During the calcination, sintering processes already take place, the second step of our powder processing, which is carried out when needed for a given purpose, i.e. for the manufacturing of dense samples or sintering the cathode layer. The driving force of the sintering process is the coalescence of individual grains with a reduction in surface area [20]. Sintering conditions for all dense samples used for the determination of electrical and kinetic properties, which will be described later, are 1100°C for

2 hours with 1 K/min heating and cooling rates. It is to be mentioned that the sintering temperatures for button cells and 50x50 mm² cells differ and are explained in the corresponding chapters. Temperature control plays an important role, since heating and cooling processes must be carried out at certain rates in order to ensure that the samples, which are to be sintered, are homogeneously heated in order to be dense and to avoid thermal stresses during cooling. In contradiction to this, when it comes to button cells and 50x50 mm² cells, the sintering temperature and sinter time tends to be lower in order to obtain a given porosity in combination with sufficient percolation.

After calcination, X-ray diffraction (XRD) is performed to determine phase purity, followed by a milling process. In order to achieve a suitable particle size distribution, one part of calcined powder is mixed with 10 parts of ethanol (EtOH) and 15.75 parts of Ø 3 mm zirconia milling balls, which is then placed on a roller bench for 72 h using 350 rpm. During further studies, it could be evaluated that by using Ø 2 mm zirconia milling balls, the required milling time can be reduced to 48 h. Regarding the necessary rotation speed, it must be considered that out of the “3 Cs” of milling, which are cataract, cascade and centrifuge, cataract is the preferred one for our purpose and the rotation speed needs to be adjusted in order to meet this demand [21]. In Table 2, the particle size distributions (PSD) for all milled powders are enlisted, whereas powders with this PSD have been used for all further experiments and for the fabrication of electrodes on cell substrates. In the case of LSM_cc, the “cc” is the abbreviation for “current collector”.

Table 2: PSD before and after milling

Sample	After calcination [μm]			After milling [μm]		
	d ₁₀	d ₅₀	d ₉₀	d ₁₀	d ₅₀	d ₉₀
LCF82_2	5.98	20.7	40.2	0.162	0.316	0.598
LCF82_3	7.15	21.7	39.9	0.303	0.504	1.54
LCFC8282_2	6.25	21.7	39.5	0.207	0.317	0.541
LCFC8282_3	8.70	25.1	43.8	0.273	0.475	1.41
LCSF622_2	8.33	23.7	41.6	0.220	0.321	0.501
LCSF622_3	7.62	21.4	39.2	0.275	0.534	1.56
LSM_cathode	-	-	-	0.310	1.08	4.67
LSM_cc	-	-	-	7.48	33.0	88.8

The majority of measurements were carried out with a CILAS 1064 L particle size analyzer using laser diffraction, except for the ones ending with “X_3”, which were measured at FZJ using a Retsch LA950 V2. It is important to mention that batches denoted “X_1” and “X_3” contain the same powders, of which “X_1” represents the unmilled state. La_{0.65}Sr_{0.3}MnO₃ (LSM) and gadolinium-doped ceria (GDC20, Treibacher Industrie AG) are commercial powders used by FZJ, which is why no initial PSD is available. The aim of our milling process is to obtain a monomodal PSD in which d₅₀ ~ 300 nm, whereas the powders milled at FZJ have slightly higher grain sizes, which is owed to the in-house standard. Using the Retsch LA950 V2, a refraction index (RI) had to be used, in order to resolve the measured data. A similar (La,Sr)O_x was used as a reference, whereby an RI of 2.40-0.10i satisfactorily fit the data. To further optimize processing

parameters, the specific surface area of the milled powders was measured by the Brunauer-Emmett-Teller (BET) method; the results are displayed in Table 3.

Table 3: Results from BET measurements

Name	Specific surface area [m ² /g]
LCF82_2	3.6
LCFC8282_2	8.1
LCSF622_2	2.2

4.2. Screen Printing

To produce thin films for SOFCs in an economical way, several options are available, i.e. foil casting, wet spraying or screen-printing. Whereas the first method is used for mass production, the latter one is the method of choice for prototyping and small quantities. In this process a high-viscosity paste, which contains a mixture of the cathode material (powder particles), as well as binder and solvent, is squeezed through the mesh openings of a screen and onto the underlying object. The advantages of this process are the low material consumption, reproducibility and continuity. A wide range of patterns can be printed, whereas in our case, circles with a diameter of 8-14 mm have been printed as well as squares with a lateral length of 40 mm, which is the length of the cathode itself, whereas the underlying substrate has a lateral length of 50 mm. The limiting factors are the size and resolution of the screen, which are given by the mesh openings and the evenness of the substrate. One further limitation is the layer thickness, whereas only certain thicknesses are producible as the screen determines the resulting layer thickness [22].

The substrate for all button cells (BCs) prepared for electrochemical impedance spectroscopy was an 8YSZ electrolyte (\varnothing 20 mm) with a GDC20 diffusion barrier layer printed on both sides. The 50x50 mm² cells consist of a Ni-Cermet anode, 8YSZ electrolyte, GDC20 diffusion barrier and the cathode applied by screen-printing. The targeted layer thickness of the cathode in the sintered state is 30-40 μ m. In order to achieve this, a wet ink thickness (WIT), which is actually the theoretical ink volume in cm³/m², of 150 μ m was selected, since the WIT (which evolves to the sintering layer) shrinks to about 1/3 of its initial thickness as a wet film during drying and sintering. The cathodes fabricated from our materials were prepared with a 18-180 mesh, where 18 represents the number of weft and warp threads in the mesh cloth per cm of mesh cloth, whereas 180 indicates the mesh thread thickness in μ m [23]. For thinner films, which were required for LSM cathode layers, a mesh with a higher amount of weft and warp threads and with a lower mesh thread thickness had to be used, which corresponds to a WIT of 34 μ m [24]. A schematic of the mesh structure and the screen-printing process is depicted in Figure 5.

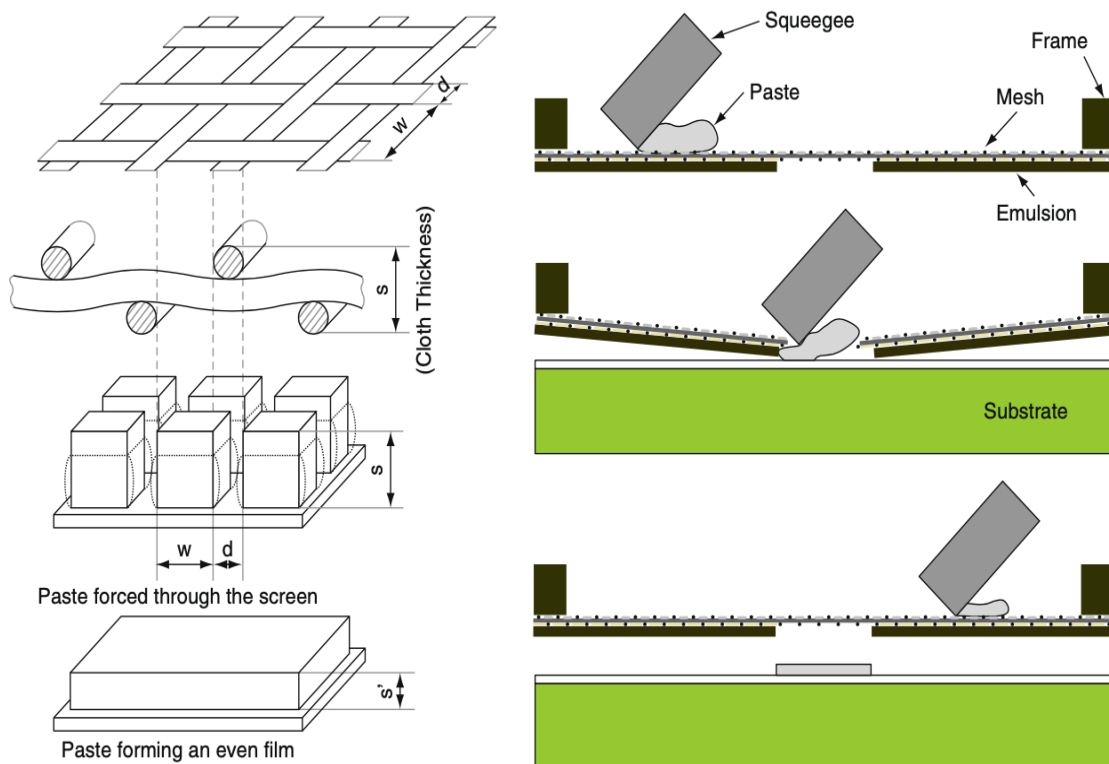


Figure 5: Concept of screen-printing (left); schematic screen-printer (right) [22].

The printing process was conducted on an EKRA E2, whereby polyester screens from KOENEN were used. All samples were dried in a furnace between 40-60°C before sintering. The corresponding meshes, printed pastes and printing parameters are given in Table 25 to Table 29 in the appendix. In order to produce a proficient screen-printing paste, it is vital to optimize the ink vehicle (IV) for the material [25]. As an IV, we used a mixture of terpineol (TP, Sigma Aldrich) and ethyl cellulose (EC, Sigma Aldrich) with a viscosity of 45 centiPoise (cP). The IV consists of 94 wt.% terpineol and 6 wt.% EC, into which then the powder is weighed in and further homogenized using a three-roll mill. This procedure is described in more detail in [26]. During the first attempts, it was necessary to add pure TP to the mixture to reach a printable viscosity state. All manufactured printing pastes with the corresponding weights are listed in Table 4 and Table 5. Since the IV consists of TP and EC, the adjusted mixing ratios can be

calculated out, which results can be seen in the penultimate column of Table 5. For this, the composition of the IV is divided into their true shares (e.g. 6 wt.% EC solved in TP corresponds to a certain in-weight of the ingredients) which is then added to the additional TP in which the IV gets solved, taking into account the percentage shares and calculating them back to absolute weight percentage.

Table 4: Screen-printing pastes with composite powders

Powder 1	Powder 2	Mass [g]			Fraction rel. [wt.%]			Paste name
		IV	P1	P2	IV	P1	P2	
LCF82_3	GDC20	10.0	5.00	5.00	50	25	25	LCF_GDC_50_50
LCF82_3	GDC20	10.0	3.00	7.00	50	35	15	LCF_GDC_70_30

Table 5: Screen-printing pastes with single-phase powders

Powder	Mass [g]			Fraction rel. [wt.%]			Fraction abs. [wt.%]			Paste name
	IV	TP	Cath.	IV	TP	Cath.	TP	EC	Cath.	
LCF82_2	1.67	3.95	8.01	12	29	59	40.5	0.7	58.8	LCF82_V1_3_1
LCF82_2	2.03	4.93	9.95	12	29	59	40.4	0.7	58.9	LCF82_V1_3_2
LCF82_3	2.06	1.65	6.27	20	17	63	36.0	1.2	62.8	LCF82_V3
LCFC8282_2	5.00	-	5.00	50	-	50	47.0	3.0	50.0	LCFC8282_V1
LCFC8282_2	10.00	-	10.00	50	-	50	47.0	3.0	50.0	LCFC8282_V2
LCSF622_2	1.86	4.37	8.88	12	29	59	40.5	0.7	58.8	LCSF622_V1
LSM_cath.	6.25	-	6.25	50	-	50	47.0	3.0	50.0	LSM_cathode
LSM_cur.	6.03	-	6.01	50	-	50	47.0	3.0	50.0	LSM_cc

For the printing, a double squeegee construction was used, which means that the sample is printed twice. The correct positioning of the squeegee is achieved by lowering it onto the screen and placing a sheet of paper between screen and squeegee. Now the distance between squeegee and screen is adjusted with a micrometer screw until the sheet of paper can barely be moved, whereby this calibration happens with both squeegees. Then the squeegees are moved to the initial position and the micrometer screws are additionally adjusted downwards by 2.5 mm in order to overcome the screen gap of 1.5 mm, whereas the remaining 1 mm is considered to counteract the mesh tension to ensure a steady printing outcome. However, individual details like the printing length need to be re-evaluated for every geometry. When printing on both sides of a BC, a drying step in a furnace is required between the two printing

steps. After one layer has been dried, the sample can be put back into the mold with the dried side down, without damage to the surface of the first printed layer. After the second side was printed, one more drying step was carried out previously to the sintering.

To determine the viscosity of selected printing pastes, a rheometer (Anton Paar Physica MCR 301) in combination with a CP25-1 rotating disc was used, in which the rotating disc has a diameter of 50 mm and an angle of 1° (Anton Paar CP25-1). The measuring program is shown in Figure 6, whereby the program is optimized for the printing process the printing process and uses a shear rate of 516 s⁻¹. This shear rate is calculated from various parameters of the printing process, i.e. the speed and width of the squeegee, the tension of the net and the duration of the print [27].

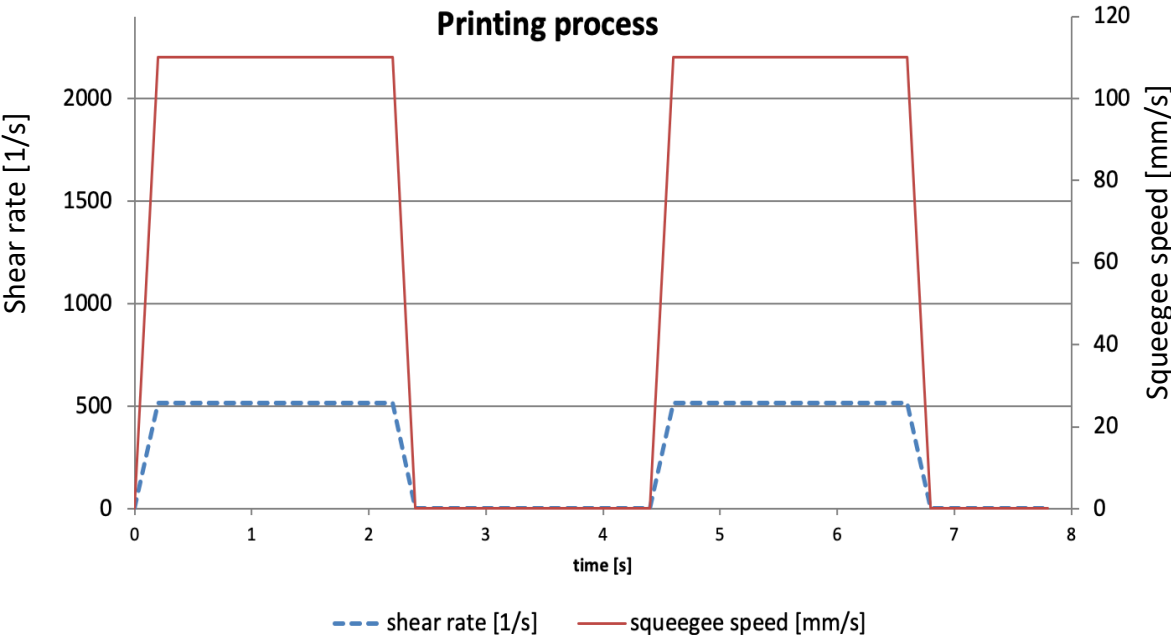


Figure 6: Schematic of the measuring program provided by Werner Herzhof (FZJ).

The red line represents the squeegee speed as it runs the printing program, which was used for all BCs and only got slightly adapted in terms of lower squeegee speed. This program consists of a two-way printing, whereas the left part of the graph represents the first run over, and the right part the second one the way back. In both cases, printing paste is applied onto the sample. The blue-dashed line represents the shear rate, which occurs during the printing process. The results from the rheological measurements for selected shear rates can be found in Figure 7 and Figure 8 in which guidelines for the eyes serve to detect the appearing yield stress, since the overall rheological behaviour can be described as shear thinning with yield [28].

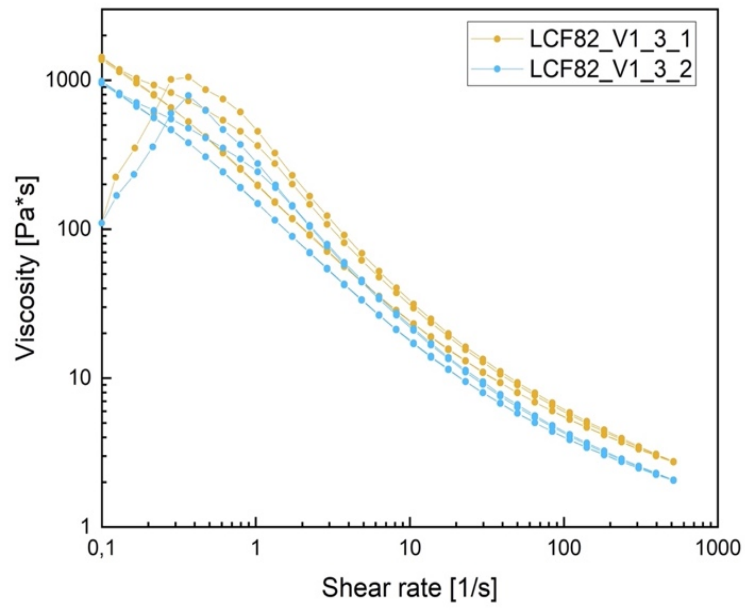


Figure 7: Viscosity of selected printing pastes as a function of shear rate.

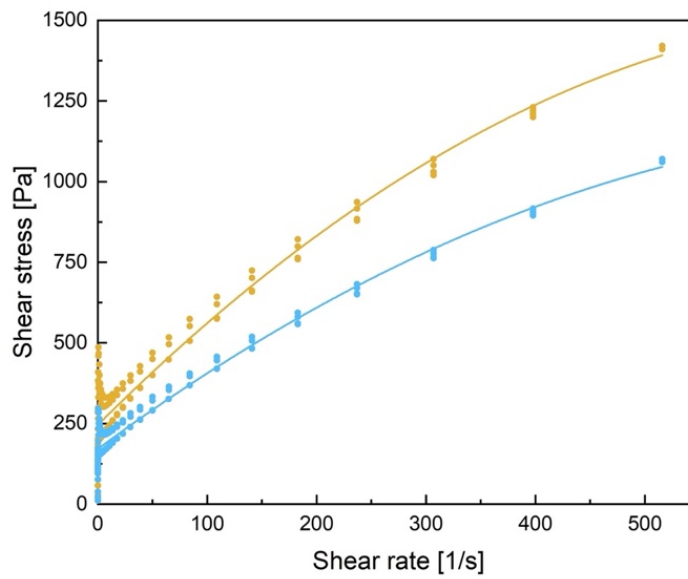
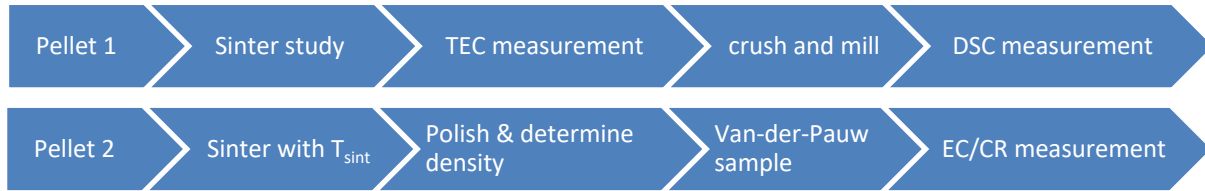


Figure 8: Shear stress of selected printing pastes as a function of shear rate.

4.3. Preparation of Dense Samples

To determine thermal and electrical properties, as well as oxygen exchange kinetics, dense samples were fabricated using milled powder. Two cylindrical pellets, which differ only in their dimensions, are compacted in an isostatic press using 240 kN for 25 min. The different pellets pass through the test paths shown below:



First, pellet 1 is produced to determine the optimum sintering temperature using a dilatometer. For this, the pressed pellet is placed in the dilatometer and heated up to 1100°C using a ramp of 1 K/min. After reaching the maximum temperature, it dwells for 10 h before cooling down to room temperature using a ramp of 1 K/min (complete program conducted in static ambient air). To determine the temperature at which the maximum sintering rate occurs, the second derivative of the curve is considered. This gives a minimum at the inflection point and therefore points to the corresponding temperature of this process, which is described in section 4.1. The sample was then removed, and the ends were grounded off. Then, the length got remeasured and the density was determined again. After this, the sample got reinstalled in the dilatometer and is used for thermal expansion coefficient (TEC) measurements at different oxygen partial pressures (1/0.1/0.01/0.001 bar pO₂). After determining the density of the sintered pellet (target: relative density > 95%), it is crushed in a mortar and differential scanning calorimetry (DSC) is performed.

Pellet 2 is sintered using the optimized temperature (T_{sint}) found in the first test path, and subsequently the surfaces are grinded and polished. After determination of the density (target: relative density > 95%), square samples are cut and further polished for dc-conductivity (relaxation) measurements in four-point van der Pauw (vdP) geometry. The samples are contacted with four gold wires and gold paste, which can be seen in Figure 9. Subsequently, the samples are installed in a reactor to perform dc-conductivity and dc-conductivity relaxation (EC/CR) measurements at different oxygen partial pressures. From these experiments, the electronic conductivity and the oxygen exchange kinetics are obtained [29].

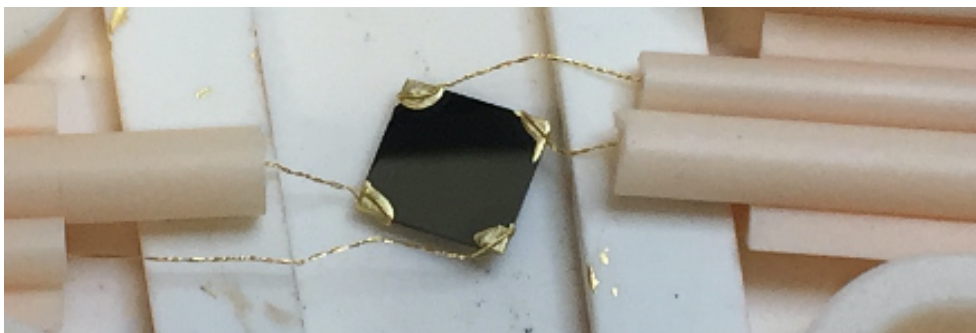


Figure 9: Contacted vdP-sample, the edge length of the sample is approx. 1 cm.

4.4. Button Cells

An electrolyte-supported cell (ESC), which consists of a symmetrical construction of “cathode/GDC20/8-YSZ|sym.” was used for electrochemical impedance spectroscopy (EIS) in ambient air. From these experiments, the polarization losses and the area-specific resistance of the cathode were obtained. Further, the tests are indicative of the adhesion of the cathode to the electrolyte. A schematic illustration of the cells can be seen in Figure 10. All cells were fabricated using the technique described in chapter 4.2. Characteristics of all fabricated BCs, with the corresponding parameters, are displayed in the appendix in Table 22 and Table 26 to Table 28.

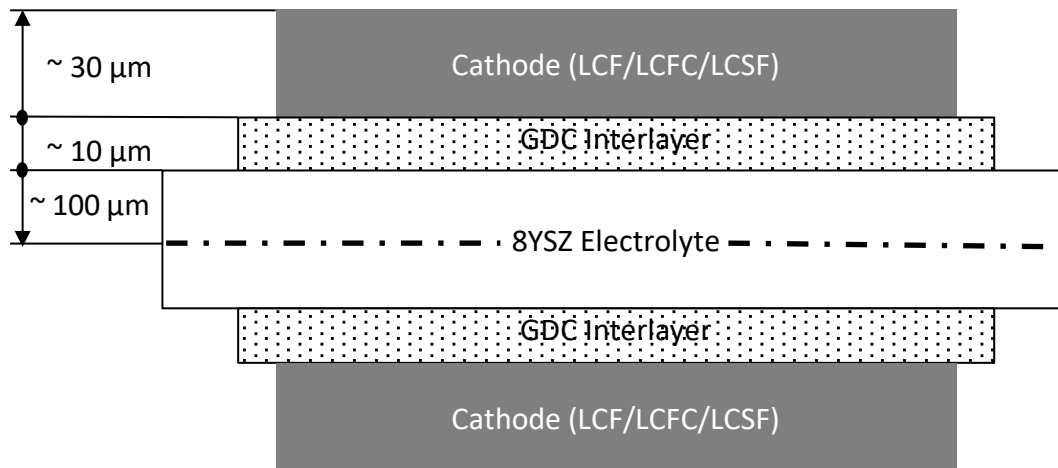


Figure 10: Schematic cross-section of an ESC.

4.5. 50x50 mm² Anode Supported Cells

The quadratic 50x50 mm² cell type, with a lateral substrate length of 50 mm and a corresponding square cathode area with a side length of 40 mm, was produced in order to assess SOFC performance under application-relevant conditions. It consists of a warm-pressed substrate, on which a NiO-cermet anode, an 8-YSZ electrolyte, a GDC20 interlayer and the cathode are printed. Except for the NiO-cermet anode, every layer was screen-printed as described in chapter 4.2. A schematic of the cells can be seen in Figure 11, whereas a real printed cathode is displayed in Figure 12. The characteristics of all fabricated 50x50 mm² cells with the corresponding parameters are displayed in the appendix in Table 23 and Table 29. The cells were tested at the IEK-9 (FZJ) at temperatures of 800-650°C with a fuel gas composition consisting of 20% H₂O and 80% H₂.

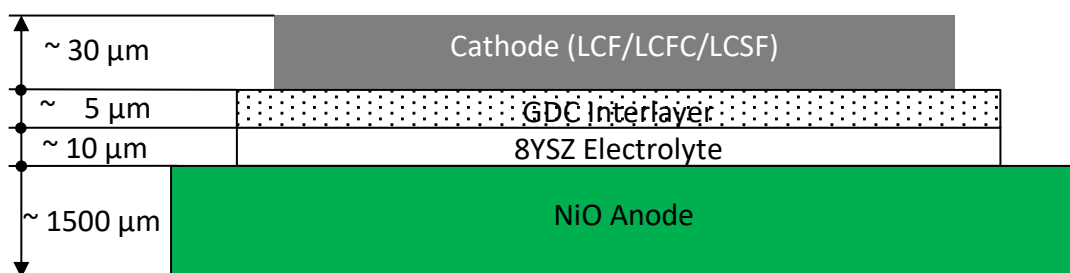


Figure 11: 50x50 mm² ASC.

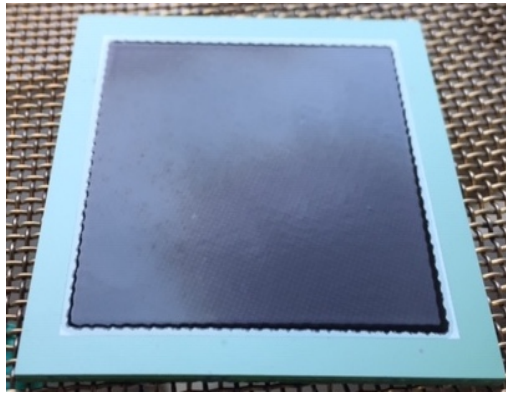


Figure 12: 50x50 mm² ASC with screen-printed LCF82

4.6. Crystal Structure and Chemical Composition

4.6.1 X-ray Diffraction and Rietveld Refinement

X-ray structure analysis has become the most important method for the structure elucidation of crystalline materials and allows the qualitative determination of the crystal structure and the quantitative determination of the phase composition. In order to obtain maximum information from an X-ray powder diffraction pattern, in addition to the individual reflections, the total pattern must also be analyzed over a larger angular range. For this purpose, the line profiles of the diffraction pattern are processed using profile fitting methods, which allows an interpretation of the overall image. The profile fitting method we have chosen is the Rietveld refinement (Rietveld method). Besides measurements in ambient air at room temperature, it is possible to perform X-ray diffraction (XRD) under non-ambient conditions, i.e. high temperatures or different atmospheres. High-temperature XRD (HT-XRD) measurements were realized at FZJ, whereas XRD measurements under ambient conditions were performed at Montanuniversitaet Leoben.

The diffraction of X-rays at a crystal lattice can be described by the Bragg-equation:

$$n\lambda = 2d_{hkl}\sin(\vartheta) \quad \text{Equation 4-1}$$

where n is an integer indicating the diffraction order, λ is the wavelength of the X-rays, d_{hkl} is the lattice plane distance between two parallel lattice planes, and ϑ is the angle between the X-ray beam and the lattice plane, also called Bragg angle. Figure 13 shows how the X-rays are reflected at the lattice planes [30]:

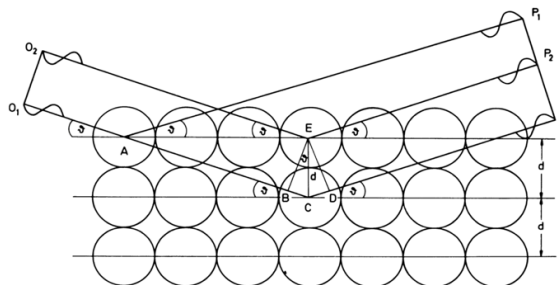


Figure 13: Reflected X-rays at a lattice plane with the corresponding Bragg angle (Bragg's reflection condition) [30].

Diffraction experiments on polycrystalline materials allow far-reaching statements about the atomic structure of the examined material, whereby the double Bragg angle is used to

represent the data in plots. By evaluation of the measurement, the interplanar spacing d_{hkl} can be calculated, since both the wavelength and the Bragg angle are known.

The complete structural information of a polycrystalline material under investigation is contained in its powder diffractogram, which can be regarded as a superposition of the Fourier transform of many crystals in reciprocal space, which are statistically distributed in their orientation [30]. The first and decisive step in profile refinement methods is the systematic decomposition of a given powder diffraction pattern into the parts of the Bragg reflections involved (pattern decomposition) and serves as preparation for the subsequent Rietveld refinement, in which a structure is refined. The decisive factor here is the ability to divide the different Bragg reflections and thus to distinguish overlapping structures from each other. The resulting parameters are mainly related to a structure model, but parameters for sample and instrument effects are also considered.

This structural model is required in advance to the Rietveld refinement and is facilitated in many cases due to similarities with structurally related substances. The choice of a suitable model therefore requires preliminary work in the form of good chemical and physical preliminary investigations of the material to be analyzed.

The actual refinement is carried out using a least-square method until the best possible match between the measured powder diffractogram and the given structural model is found. The choice of the radiation source has no influence on the evaluation but is considered in the form of the atomic scattering factor. Thus, data obtained from measurements with different radiation sources can be combined with each other.

4.6.2 Inductively Coupled Plasma Atomic Emission Spectroscopy

Inductively coupled plasma atomic emission spectroscopy (ICP-AES) is one of the atomic plasma emission spectroscopic methods, together with microwave-induced electrical discharge plasma and other plasma discharges used in chromatographic detection, which allows simultaneous multi-element measurement in combination with a wide dynamic measurement range with good sensitivities and selectivities over background elements. It is crucial for chromatographic instrumentation to include a detection device for qualitative and quantitative determination of the components resolved by the column, whereas the response to the presence of solute in the mobile phase must be immediate and predictable. ICP is the most widely used analytical emission spectrochemical source. Radiofrequency (RF) usually at 27 or 41 MHz produces the discharge, interacting with argon or other gases, which are flowing through a quartz tube within a copper coil. A varying magnetic field is created by the RF generator, which in turn generates a circulating eddy current in the heated gas. At temperatures above 9000 K, a stable and spectrally intense plasma discharge is produced. Liquid sample introduction involves a spray chamber-nebulizer to generate an aerosol, which is carried by the gas into the plasma where solvent is evaporated and the analyte atomized, in which case chemical and molecular interferences can be considered to be negligible. Whereas non-metals usually have lower detection limits and selectivities than metals, which is due to the absence of background in the spectral region monitored and emission intensity in the latter, principal difficulties involve gas chromatographic stabilities at the column temperatures needed for gas chromatography [31].

4.7. Thermal Properties

4.7.1 Thermal Expansion Coefficient

The atoms in a solid body arrange themselves in such a way that their energy is minimal, i.e. the forces acting on them disappear which is the case in the minimum interatomic potential (E_{P0}). The precise calculation of the interatomic potential is not yet possible. Usually, approximate functions are used, which qualitatively have the course shown in Figure 14 and whose values are adapted to measurable material properties. The best-known potential functions are the Morse potential (exponential approximation) and the Lennard-Jones potential (approximation by power law).

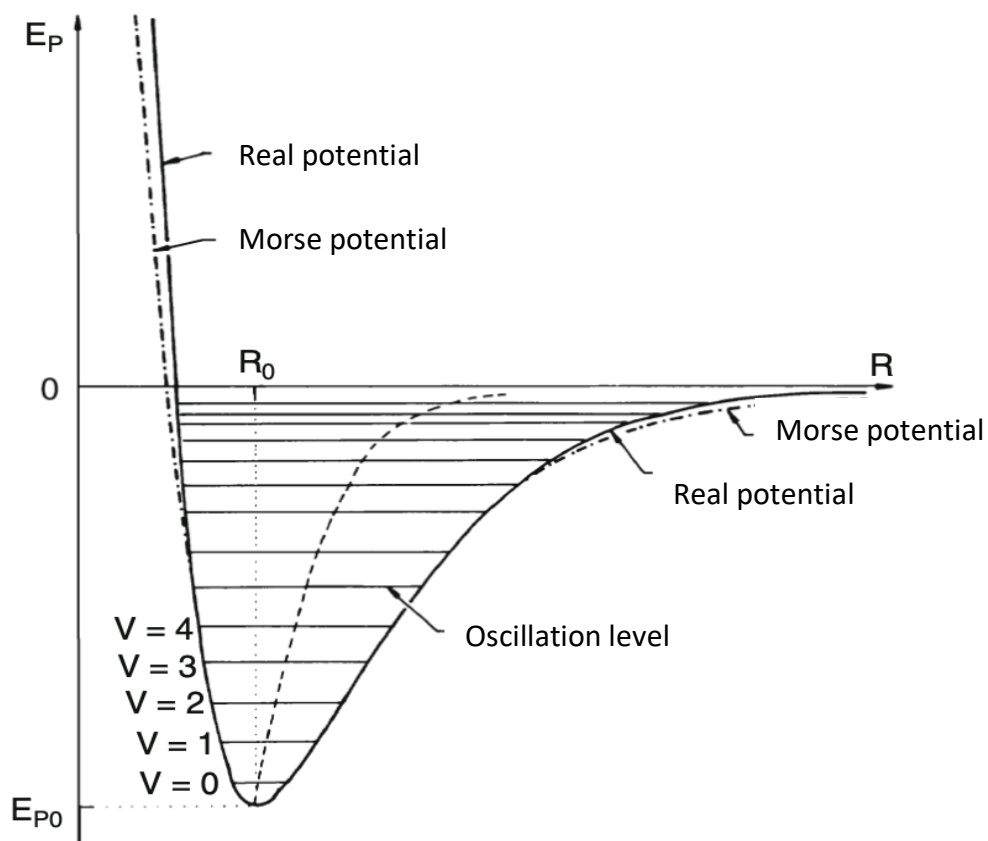


Figure 14: Potential energy of a diatomic molecule plotted over the atomic distance (schematic). Illustration modified from [32].

By supplying heat, the atoms in a solid body are made to vibrate, which we experience as its temperature. The greater the supply of heat, the higher the temperature and the greater the oscillation amplitude of the atoms. If the energy potential of atoms would be symmetrical with respect to its lowest point of energy (harmonic approximation), the center of gravity of the oscillations would be independent of the oscillation amplitude. Thus, the atoms would oscillate around their rest position at $T = 0$ K, independent of the temperature, so that the mean atomic distance would not change with temperature and would remain always at R_0 . This is not observed; however, for temperatures which are not too low ($T > \Theta_D/2$ whereby Θ_D is the Debye temperature), the thermal expansion $\Delta l/l_0$ increases linearly with the temperature, respectively the thermal expansion coefficient (TEC) described by

$$\alpha = \left(\frac{1}{l}\right) \frac{dl}{dT}$$

Equation 4-2

remains constant [32].

The TEC represents a characteristic material property not only for solid materials, but also for every crystal structure in which a given material occurs. To determine TECs, usually dilatometers are used, in our case a Netzsch DIL 402 PC at Montanuniversitaet Leoben. As samples we used "Pellet 1", fabricated as described in chapter 4.3. For the measurement, the pellet was put into the heating chamber of the dilatometer whereby alumina and magnesium oxide plates served as support. All samples were heated up twice from room temperature to 1000°C (without an isothermal unit) using a 1 K/min heating (and cooling) ramp, with a two-hour break between the cycles. whereby this measurement program is carried out in atmospheres with different oxygen partial pressures (1/0.1/0.01/0.001 bar pO₂). The data is then analyzed using the Netzsch Proteus software, with which we can determine the TEC by analyzing the slope of the second heating curve. This can then be displayed as the relative length change of the sample $\Delta l/l_0$ vs. temperature.

4.7.2 Differential Scanning Calorimetry

Differential scanning calorimetry (DSC) measures the difference in the heat-amount as a function of temperature required for increasing the temperature of a sample and a reference, whereby both sample and reference maintain approximately the same temperature throughout the whole experiment. Therefore, DSC measures the change of a property – the heat-flow rate difference – which is normally released due to an alteration of the sample temperature. If no alteration occurs, no change of a heat flow rate difference can be measured (except for possible chemical reaction heat flow rates). In the case of thermally activated reactions or phase transitions, i.e. induced by a regulated gradual change from one stable temperature to another, the temperature of the sample undergoes an alteration due to internal processes and causes the DSC signal, which is then further analyzed. DSC is nowadays a widely spread measuring method used in various areas of research and quality inspection due to its accuracy. Over a wide temperature range, not only thermal effects but also the relevant temperatures and characteristic caloric values can be determined, using sample quantities in the mg range. A typical heat flux DSC test setup is shown in Figure 15 [33].

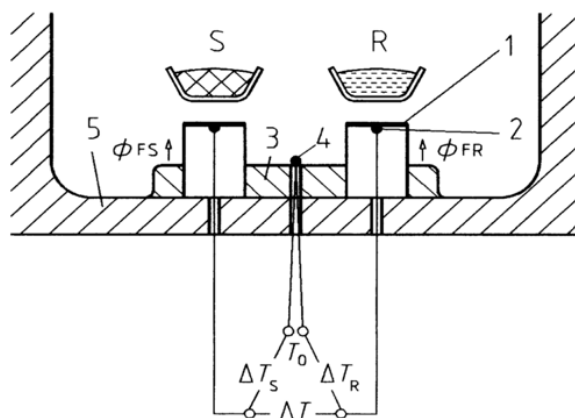


Figure 15: Heat flux DSC with turret-type measuring system (TA Instruments). 1) elevated platform for sample and reference sample, 2) chromel area thermocouple, 3) constantan body, 4) chromel-constantan thermocouple, 5) silver furnace, S) sample substance, R) reference sample substance, ΔT) platform temperature difference, T_0) body (furnace) temperature [33].

4.7.3 Combustion Analysis

Through combustion analysis, the oxygen, nitrogen and hydrogen content (and by subsequent data analysis – the oxygen non-stoichiometry) of a variety of materials can be determined, using the inert gas fusion principle. The weighed sample is placed in a crucible of high-purity graphite under a flowing stream of helium gas stream at temperatures sufficient to release oxygen, nitrogen, and hydrogen. The oxygen in the sample, in whatever form present, combines with the carbon from the crucible to form carbon monoxide. The nitrogen present in the sample is released in the form of molecular nitrogen, and any hydrogen as hydrogen gas. The amounts of oxygen and hydrogen are then measured by infrared (IR) absorption. First, the sample gases enter the IR module and pass through CO and CO₂ detectors, whereby the total quantity of oxygen, which is present in either one of those states, is detected. Following this, the sample gas is passed over heated copper oxide to convert CO to CO₂, and any hydrogen to water. Gases then re-enter the IR module and pass through a separate CO₂ detector for total oxygen measurement and an H₂O detector for quantification of hydrogen [34].

Immediately before the analysis of an oxide sample, it is necessary to calcine the powder by heating it to 800°C, to keep the water content to a minimum, which may otherwise affect the reproducibility of the measurement. In order to account for the measured hydrogen, we assumed that it is completely bound in (residual) H₂O. This means that for every mole of hydrogen, half a mole of oxygen is bound in the form of water and should therefore not be included in the oxygen stoichiometry of the perovskite.

4.8. Electrical Properties

4.8.1 Electronic Conductivity

Many ceramic materials are electrical insulators. However, ceramics are much more versatile in terms of electrical conductivity than metals or polymers. Especially at high temperatures, ceramic materials can be used advantageously both electrically and structurally, despite their inherent brittleness and susceptibility to fracture [35]. The oxygen partial pressure during preparation can affect the properties of many oxides (e.g. perovskites), which can be either oxidized or reduced, depending on the respective conditions. These effects are dependent on the possibility of valence changes of the cations and/or the formation of cation- and oxygen defects. If, e.g. in a perovskite, the cation valence cannot be subject to change, oxygen-poor compositions are accommodated by the formation of oxygen vacancies. Additional oxygen can be incorporated in the form of interstitials, if the structure is open enough to allow for this possibility. These possibilities are often associated with changes in the ionic and electronic conductivity (EC) of the compounds, which can be of considerable importance for applications [17].

By using the Kröger-Vink notation, the loss of oxygen in the materials $(\text{La,Ca,Sr})(\text{Fe,Co})\text{O}_{3-\delta}$ studied in this work, can be formulated as



whereby the equilibrium constant K for this reaction is

$$K = [\text{V}_\text{O}^{\bullet\bullet}] [e']^2 p_{\text{O}_2}^{1/2} [\text{O}_\text{O}^\times] \quad \text{Equation 4-4}$$

Therefore, it can be stated that the number of oxygen vacancies is proportional to the oxygen partial pressure as

$$[\text{V}_\text{O}^{\bullet\bullet}] \propto p_{\text{O}_2}^{1/2} \quad \text{Equation 4-5}$$

when valence changes of the cations can be neglected. As it can be seen in Equation 4-3, the presence of oxygen vacancies directly results in the appearance of a balancing electron population to ensure charge neutrality. In an acceptor-substituted mixed ionic-electronic conducting transition metal perovskite such as $(\text{La,Ca,Sr})(\text{Fe,Co})\text{O}_{3-\delta}$, this results in the partial reduction of M^{4+} to M^{3+} ($\text{M}=\text{Co, Fe}$) and therefore to a decrease in the concentration of p-type electronic charge carriers $[\text{M}_\text{M}^\bullet]$. Thus, the EC increases with increasing oxygen partial pressure as well as increasing number of p-type charge carriers, and with decreasing number of oxygen vacancies according to

$$\sigma_e \propto [\text{M}_\text{M}^\bullet]^m \propto p_{\text{O}_2}^n \propto [\text{V}_\text{O}^{\bullet\bullet}]^{-p} \quad \text{Equation 4-6}$$

Where m, n, and p are exponents, which are determined by the materials' defect chemistry. For example, the lanthanum iron oxides have the nominal formula $\text{La}^{3+}\text{Fe}^{3+}\text{O}_3$. A-site substitution with an alkaline earth cation, such as Ca^{2+} or Sr^{2+} necessitates the formation of one Fe^{4+} cation for every substituent ion. Assuming that no change in oxygen stoichiometry occurs, the now Ca-substituted phase can be written as $\text{La}_{1-x}\text{Ca}_x\text{Fe}_{1-x}^{3+}\text{Fe}_x^{4+}\text{O}_3$. Alternatively, the negative effective charge of the substituent may be compensated by the formation of $\frac{1}{2}$ oxygen vacancy

for every substituent ion $\text{La}_{1-x}\text{Ca}_x\text{Fe}^{3+}\text{O}_{3-x/2}$. The extent of electronic and ionic charge compensation depends on the composition of the material, as well as external parameters such as temperature and $p\text{O}_2$.

In order to determine the EC of our specimen, the van der Pauw (vdP) method is used. By further evaluation of the EC as a function of temperature and $p\text{O}_2$ and under consideration of the defect chemistry, further insights may be gained into charge density and mobility of the majority carriers. The vdP method uses a four-point measurement geometry, with the advantage of using arbitrarily shaped samples, as long as the sample is approximately two-dimensional, which means it needs to be much thinner than it is wide. The contacted sample is shown schematically in Figure 16, where A implies an ampere meter to measure current and V a voltmeter to measure voltage.

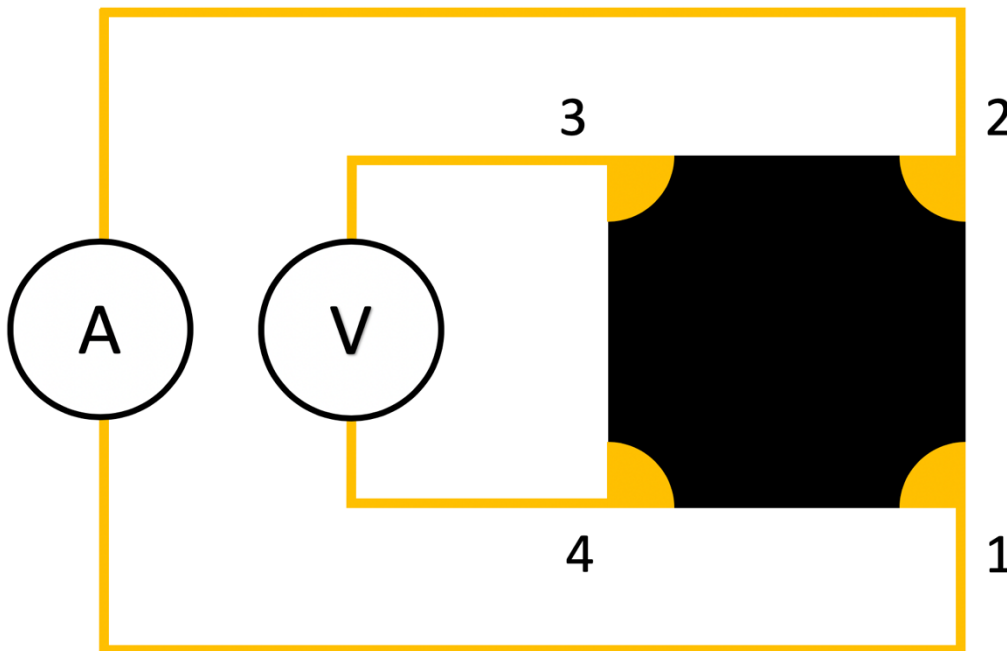


Figure 16: Contacted vdP sample.

With this method, the specific resistivity is given by

$$\rho = R_S \cdot t \quad \text{Equation 4-7}$$

in which R_S is the sheet resistance and t the thickness. To perform a measurement, a current (i.e. I_{12}) input along one side is introduced and the voltage (in this case U_{34}) response on the opposite edge is measured. From these two values a resistance can be calculated using Ohm's law as

$$R_{12,34} = \frac{U_{34}}{I_{12}} \quad \text{Equation 4-8}$$

By determining two of those resistances, i.e. one along a vertical edge such as $R_{12,34}$ and one along a horizontal edge $R_{23,41}$, van der Pauw showed that the sheet resistance of samples which fulfill the terms stated above is related to these resistances by the van der Pauw formula

$$e^{-\pi R_{12,34} / R_s} + e^{-\pi R_{23,41} / R_s} = 1$$

Equation 4-9

with which R_s can be calculated by using an iterative method and therefore also the specific resistivity as well as its reciprocal value (the specific electrical conductivity $\sigma = 1/\rho$) [29]. When the specific ionic conductivity is several orders of magnitude smaller than the specific electronic conductivity, the specific electrical conductivity corresponds to the EC ($\sigma = \sigma_e + \sigma_i \approx \sigma_e$).

In order to determine the EC at different temperatures, these measurements are carried out in a furnace, which is also equipped for measurements in test gases with different pO_2 . Electrical conductivity relaxation (CR, see chapter 4.9.) measurements can also be performed in this measurement setup. During the time segments in which the pO_2 is kept constant, EC measurements are performed. When a step-wise change in the pO_2 is introduced, CR can be measured. Figure 17 illustrates this measurement scheme, whereby the pO_2 is changed between 10% and 15% O_2 in Ar.

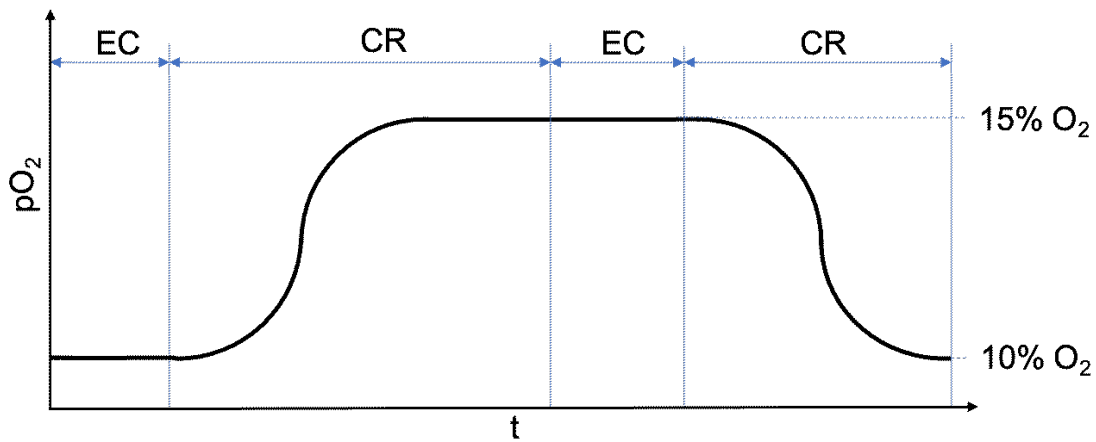


Figure 17: EC/CR measurement profile.

These measurements were conducted between 800°C and 600°C in steps of 50°C upon cooling (and steps of 100°C upon heating, to check reproducibility). The considered pO_2 changes are realized by switching between test gases with 10%/15%, 1%/1.5% and 0.1%/0.15% O_2 (rest Ar).

4.9. Oxygen Exchange Kinetics

The most vital part in every SOFC cathode material is the ability to reduce molecular oxygen to oxygen ions at its surface and subsequently conduct them throughout the bulk material. *De Souza* [36] and *Adler et al.* [37] suggest the following reaction path for oxygen at the surface of mixed ionic-electronic conductors (MIEC): (1) dissociative oxygen adsorption, (2) ionization of the oxygen atom, (3) incorporation of the adsorbed oxygen ion in the cathode bulk, (4) bulk diffusion, and (5) oxygen ion charge transfer from the cathode bulk into the electrolyte, as illustrated in Figure 18. The chemical oxygen surface exchange coefficient k_{chem} is linked to steps (1), (2) and (3), whereas the chemical diffusion coefficient of oxygen D_{chem} is linked to (4) [38].

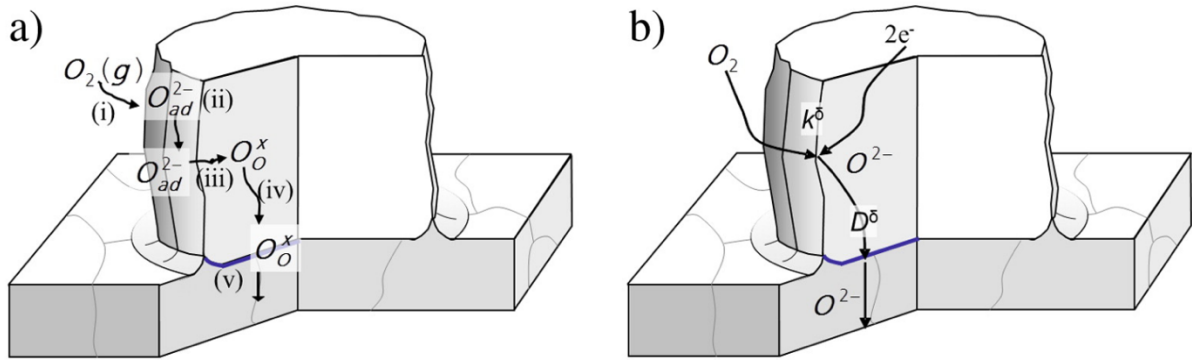


Figure 18: Oxygen reduction at a mixed ionic–electronic conducting cathode grain, which is in contact with an ionic conducting electrolyte. a) Reaction path suggested by De Souza [36] and Adler [37] b) The surface exchange coefficient $k_{\text{chem}} (= k^{\delta})$ is linked to (1), (2) and (3), and the bulk diffusion coefficient $D_{\text{chem}} (= D^{\delta})$ to (4). Illustration from [38].

4.9.1 Chemical Surface Exchange Coefficient and Chemical Diffusion Coefficient of oxygen

Both k_{chem} and D_{chem} are measured in a single experiment, which is described in chapter 4.8.1, by analyzing the transient conductivity with the suitable solution of Fick's second law for given boundary conditions (determined by the sample dimensions and the setup properties). In principle, this method is susceptible to two potential sources of error: One is the conditions of the sample itself and the other is introduced by the method of changing the atmosphere around the sample [38]. The result of the measurement is a relaxation curve, which now has to be analyzed using a nonlinear fitting procedure.

Depending on the rate-limiting step of the overall oxygen exchange kinetics, three different cases can be distinguished. In the first case it is assumed that the oxygen exchange kinetics is strictly limited by the incorporation of oxygen on the surface of the material, which means the kinetics would be k_{chem} -controlled [39]. This can be expressed with the equation

$$\ln(1 - \sigma_{\text{norm}}) = -\frac{2 \cdot k_{\text{chem}}}{L} \cdot t \quad \text{Equation 4-10}$$

where σ_{norm} is the normalized specific electrical conductivity, L the thickness of the sample and t the time.

A bulk diffusion-limited kinetics, here described as D_{chem} -controlled, follows if the ordinate intercept of the $\ln(1-\sigma)$ vs. t plot is around -0.21 as expressed in

$$\ln(1 - \sigma_{\text{norm}}) = \ln\left(\frac{8}{\pi^2}\right) - \frac{D_{\text{chem}} \cdot \pi^2}{L^2} \cdot t \quad \text{Equation 4-11}$$

In the third case, the kinetics may be limited by both k_{chem} and D_{chem} , which can be described as mixed-controlled kinetics, according to

$$\ln(1 - \sigma_{\text{norm}}) = \ln \left\{ \frac{2 \cdot k_{\text{chem}}^2}{\frac{k_{\text{chem}}^2 \cdot \gamma^2 \cdot \left[\frac{k_{\text{chem}} \cdot L}{D_{\text{chem}}} \right]^2}{4} + \frac{\gamma^2 \cdot L^2}{4} + \frac{k_{\text{chem}} \cdot L}{2 \cdot D_{\text{chem}}}} \right\} - D_{\text{chem}} \cdot \gamma^2 \cdot t$$

Equation 4-12

in which γ is an eigenvalue defined as $\gamma = \tan\left(\frac{\gamma \cdot L}{2}\right) = \frac{k_{\text{chem}}}{D_{\text{chem}}}$. Further details on the method are described in [40] [41] [42].

In Figure 19, a representative fitting process is displayed, in which the normalized specific conductivity can be best fitted using the expression for mixed-controlled kinetics. Further determination of the fitting procedure was performed in this manner.

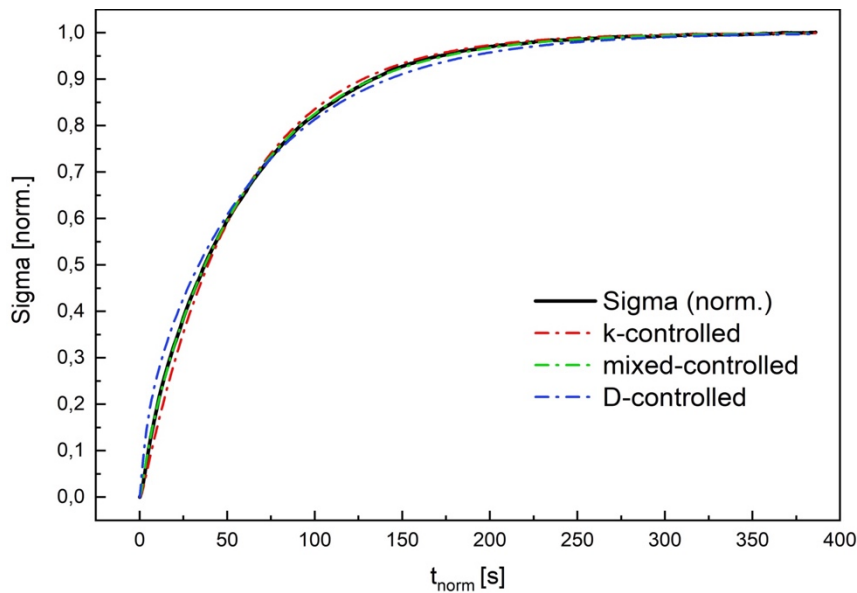


Figure 19: Data and fits for CR of LCF82 (oxidation at 700°C).

4.10. Electrochemical Properties

4.10.1 Electrochemical Impedance Spectroscopy

Electrochemical Impedance Spectroscopy (EIS) can be described as a measurement in the frequency domain of a complex system that cannot be easily visualized. The measured quantities, i.e. current and potential in electrochemical or electronic systems, are macroscopic values that are representations of the spatial average of individual events. These quantities are affected by the physical properties of the sample, such as charge transport in electrodes and in the electrolyte, ion diffusion, transport processes in grain boundaries and bulk and charge transfer at phase boundaries, which can however not be directly measured.

EIS experiments involve the conversion of input and output signals in the time domain into complex quantities that are functions of frequency. A signal generator is used to control a potentiostat and to induce a perturbation function. The input signal and the resulting output signal are processed by instrumentation in order to obtain a frequency-dependent transfer

function, whereby the basic condition for a reasonable interpretation of the response is a strict mathematical relationship between the excitation and response signal. The advantage of this method is that simultaneous processes can be separated – if they occur in different frequency ranges (more precisely: if the difference in the relaxation times is large enough). As an example, diffusion processes are usually observed in the low-frequency range, whereas rapid processes (e.g. charge transfer or charging of the double layer capacity) occur in the high-frequency range. The separation of bulk and grain boundary conductivity of bulk materials is also possible under this condition.

Impedance spectra are usually evaluated by equivalent circuit models, consisting of appropriate impedance elements. The total impedance can then be determined, and the correlation found is used to fit the measured data. Besides the classical impedance elements like capacitors or resistances, other characteristic elements like a Constant Phase Element (CPE) or a Warburg impedance are used [43] [44].

For the measurement, a “Probostat” setup in combination with a Novocontrol Alpha-A High Precision Frequency Analyzer under ambient conditions was used. All experiments performed with ESCs included measurements with both 100 mV and 200 mV at every considered temperature in a frequency range from 1 MHz to 100 mHz by using equidistant frequency steps in the logarithmic representation, which are calculated by the WinDETA measuring software. The contacting of the cathode surfaces is realized by Pt-meshes on both electrodes. The program consists of a heating ramp from RT to 850°C using 10 K/min and then, while cooling down with 5 K/min to 600°C, measuring with the designated voltages in 25°C steps. Finishing the 600°C measuring points, a cooling period with 10 K/min starts until reaching RT again.

The data was analyzed using the software ZView (Scribner Associates), whereby the equivalent electrical circuit seen in Figure 20 was used.

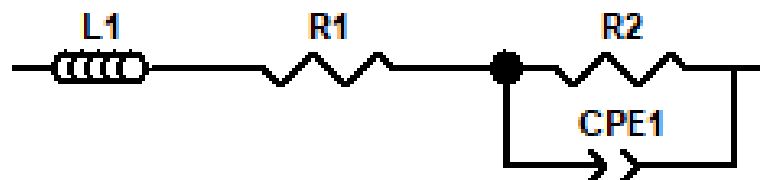


Figure 20: Equivalent electrical circuit.

In Figure 21, a representative evaluation is shown. Using this method, the first intersection point with the abscissa, which represents Z' , can be considered as the ohmic resistance R_0 of the cell (here named R_1), whereas the diameter of the circle, when normalized to the cathode area of 78.5 mm², which results from the printed cathode diameter, represents the polarization resistance R_{pol} (here named R_2). Both R_0 and R_{pol} can now be displayed in various kinds of plots – for comparison within a test series, but also to benchmark them with state-of-the art LSCF6428 [45]. In addition, R_{tot} was calculated, which is the normalized sum of R_0 and R_{pol} .

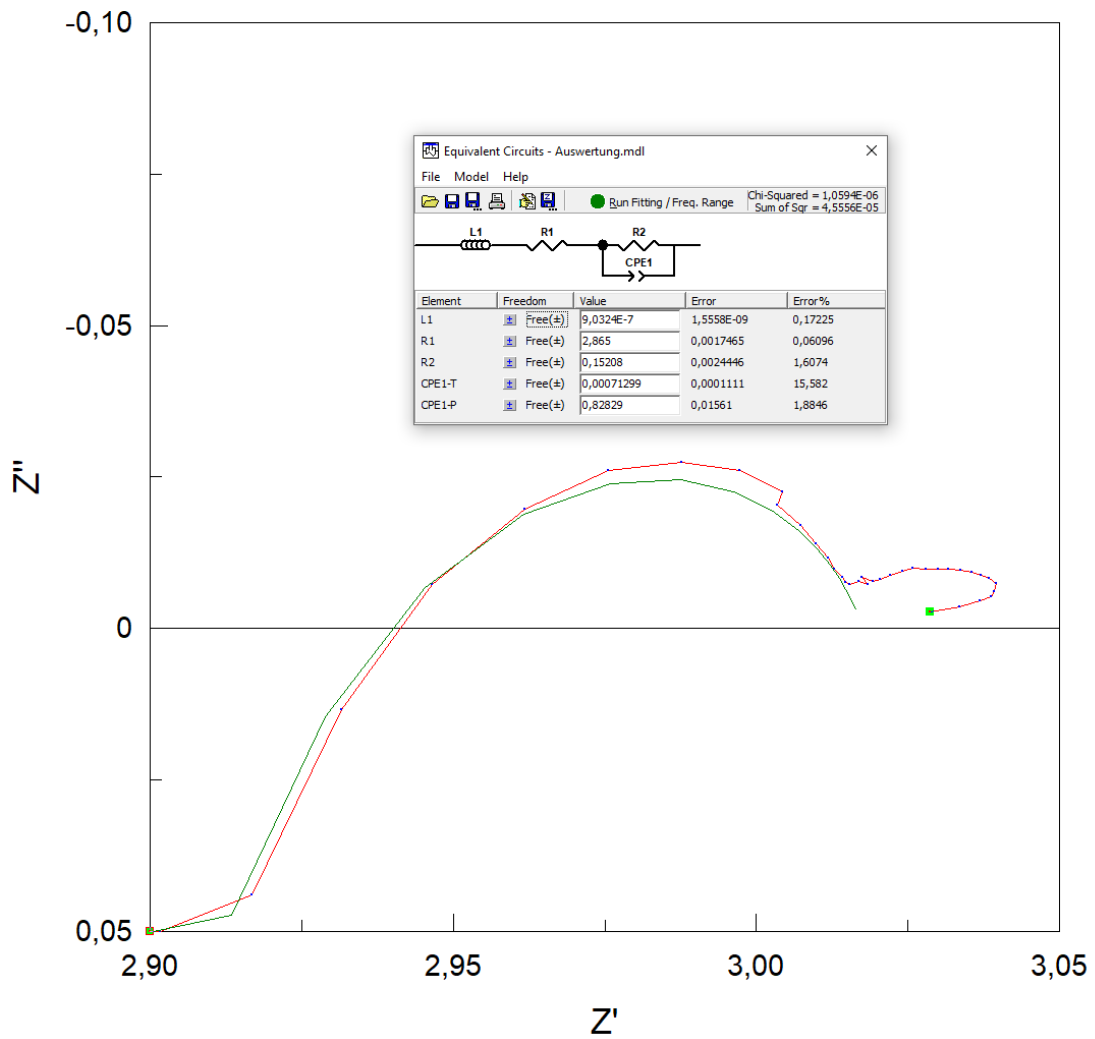


Figure 21: Exemplary representation of EIS data evaluation.

5. Results and Discussion

5.1. Crystal Structure

At room temperature (RT), the perovskites investigated in the present work belong to the *orthorhombic* crystal system, whereby the unit cell parameters are determined by $\alpha = \beta = \gamma = 90^\circ$ und $a \neq b \neq c$ [46]. Therefore, all structures can be classified into the space group No. 62, which corresponds to the Hermann-Mauguin notation $P \frac{2_1}{n} \frac{2_1}{m} \frac{2_1}{a}$, abbreviated *Pnma* and can be described as tilted *orthorhombic* [47]. Above 700°C , a phase transformation from the *orthorhombic* to the *trigonal* structure occurs with LCF82, which can be classified into the space group No. 167, corresponding to *R-3c*. LCF8282 also shows a structural transformation above 500°C , being classified into the space group No. 167, corresponding to *R-3c*. In contrast, LCSF622 shows no change in the crystal structure at elevated temperatures. All changes at elevated temperatures are fully reversible upon cooling. The diffraction patterns measured under ambient conditions at RT for the calcined samples are displayed in Figure 22.

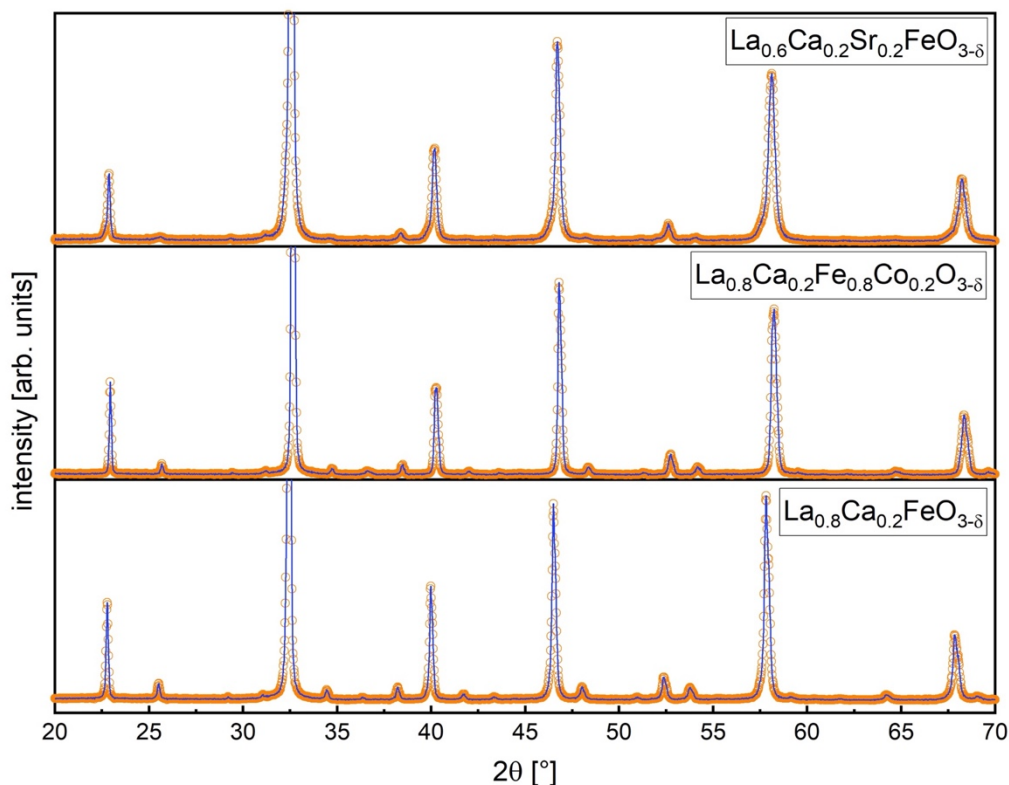


Figure 22: Diffraction patterns at room temperature and Rietveld refinement.

The HT-XRD measurements took place in ambient air using a temperature ramp of 5 K/min . Between 100 and 1100°C , diffractograms were recorded in steps of 100°C . At 950°C , an additional measurement was performed, since this temperature was used for sintering the cathodes printed on the electrochemical cells. Each XRD measurement was conducted after a two-minute temperature dwell. The resulting diffraction patterns are shown in Figure 23 to Figure 28, whereby the patterns measured during heating and cooling, respectively, are displayed.

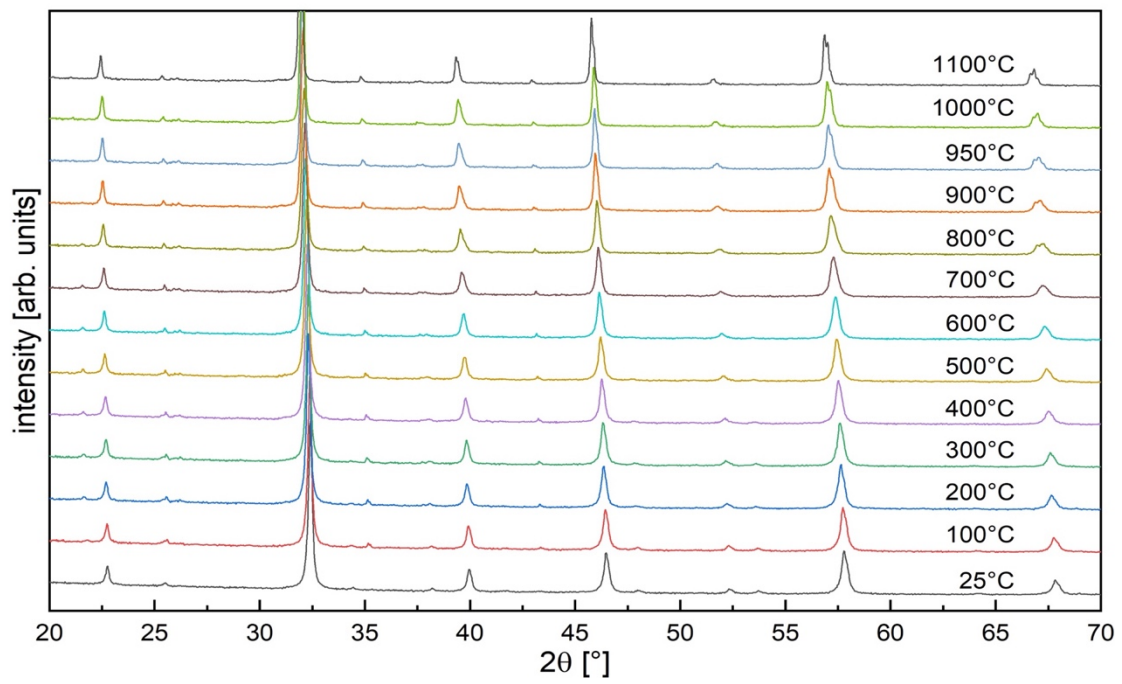


Figure 23: HT-XRD diffraction patterns of LCF82 during heating.

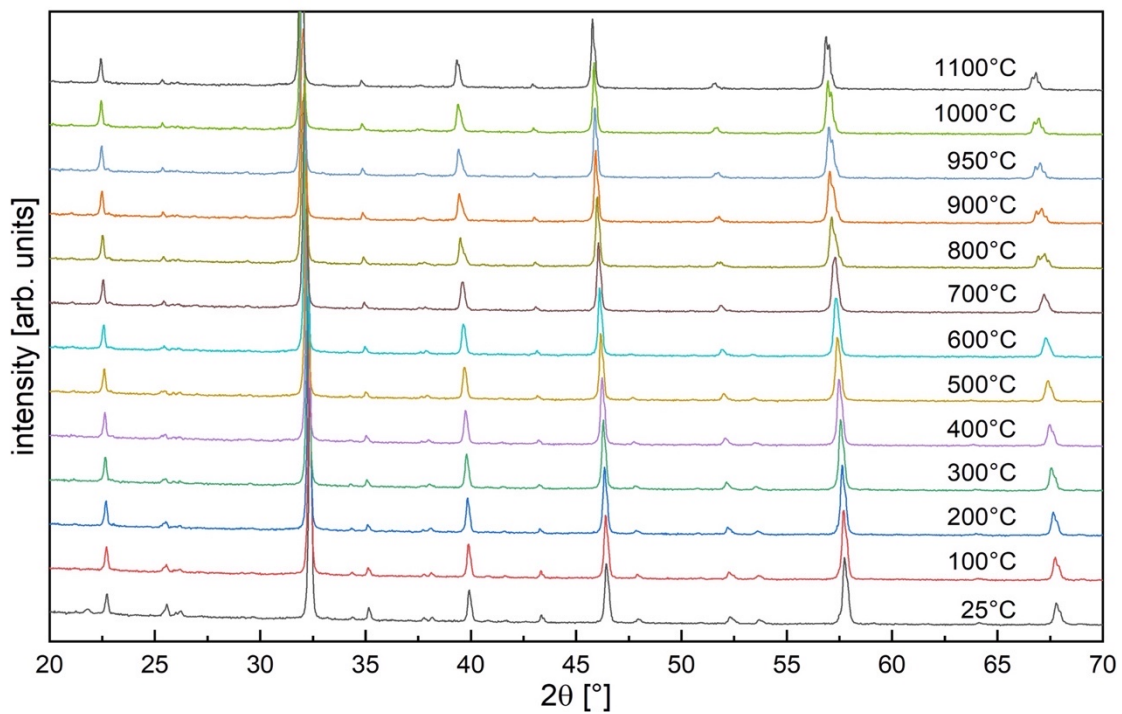


Figure 24: HT-XRD diffraction patterns of LCF82 during cooling.

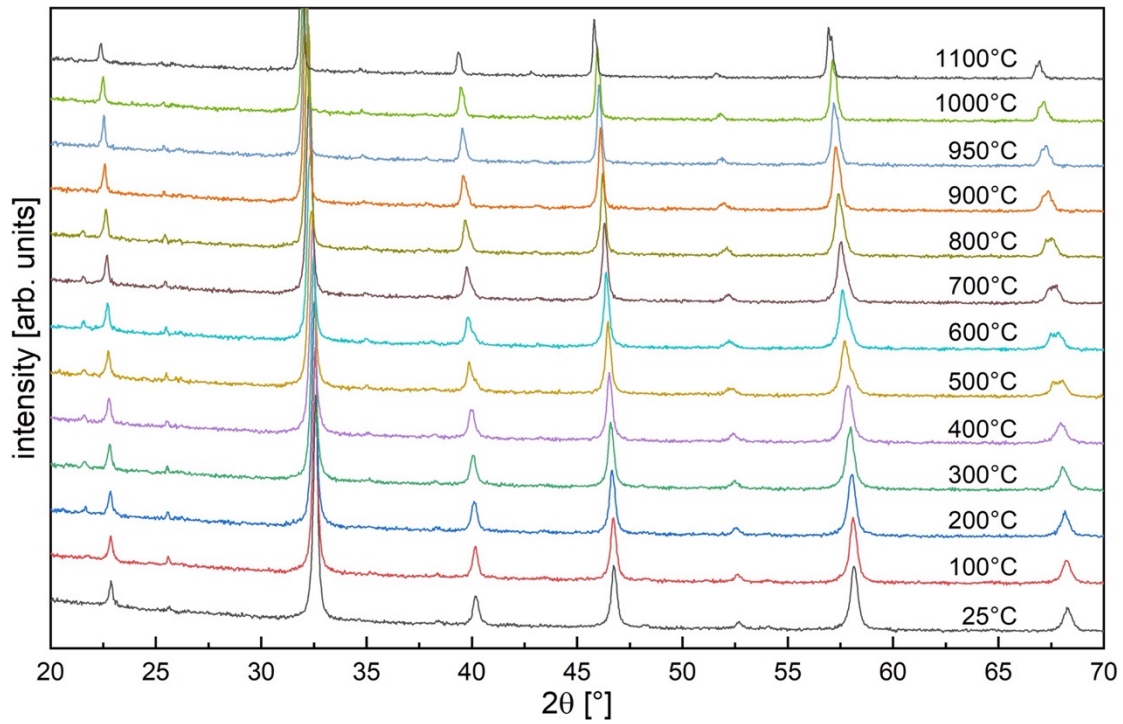


Figure 25: HT-XRD diffraction patterns of LCFC8282 during heating.

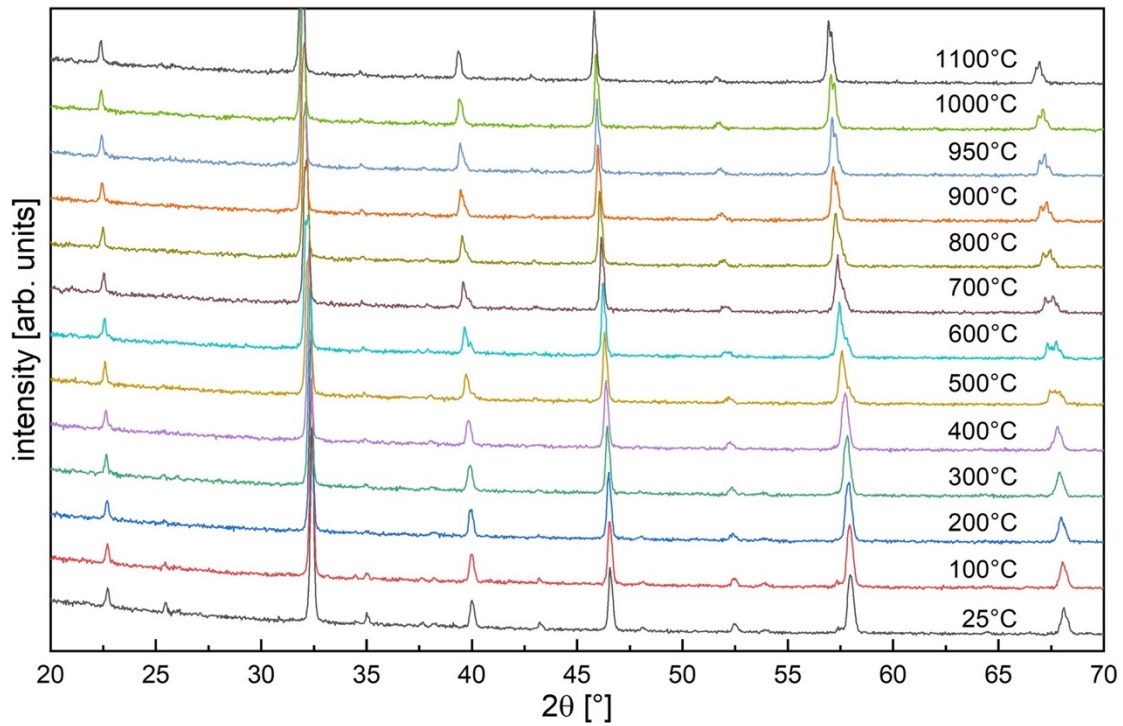


Figure 26: HT-XRD diffraction patterns of LCFC8282 during cooling.

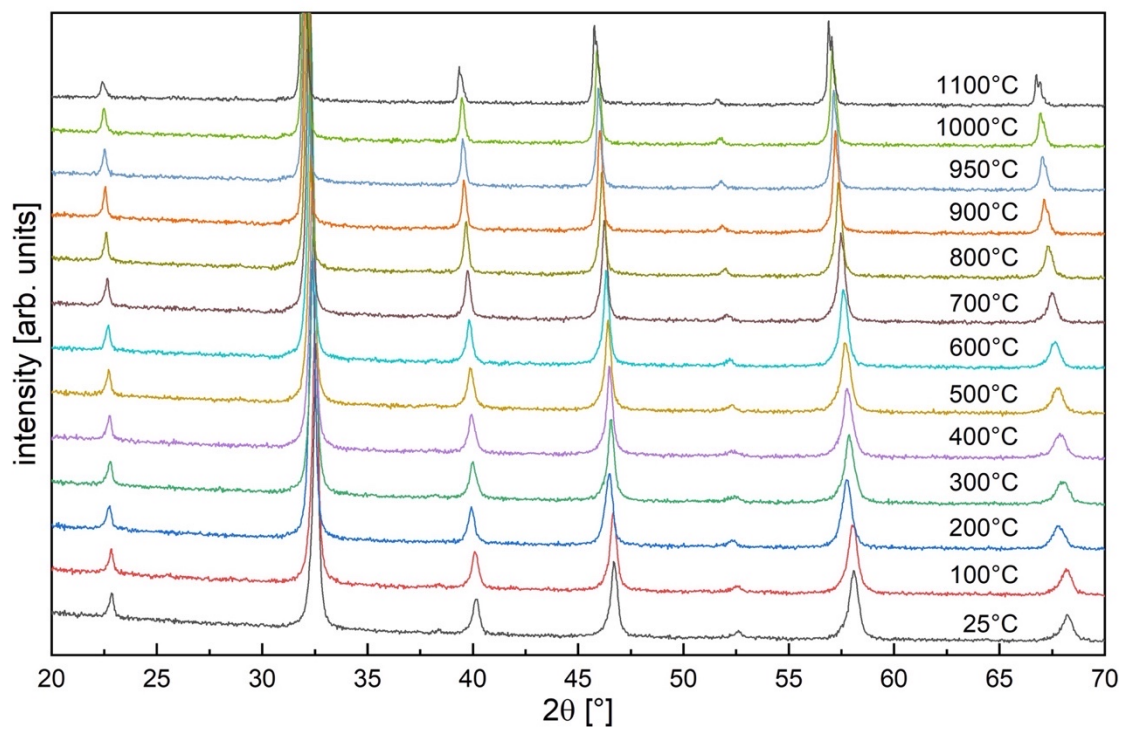


Figure 27: HT-XRD diffraction patterns of LCSF622 during heating.

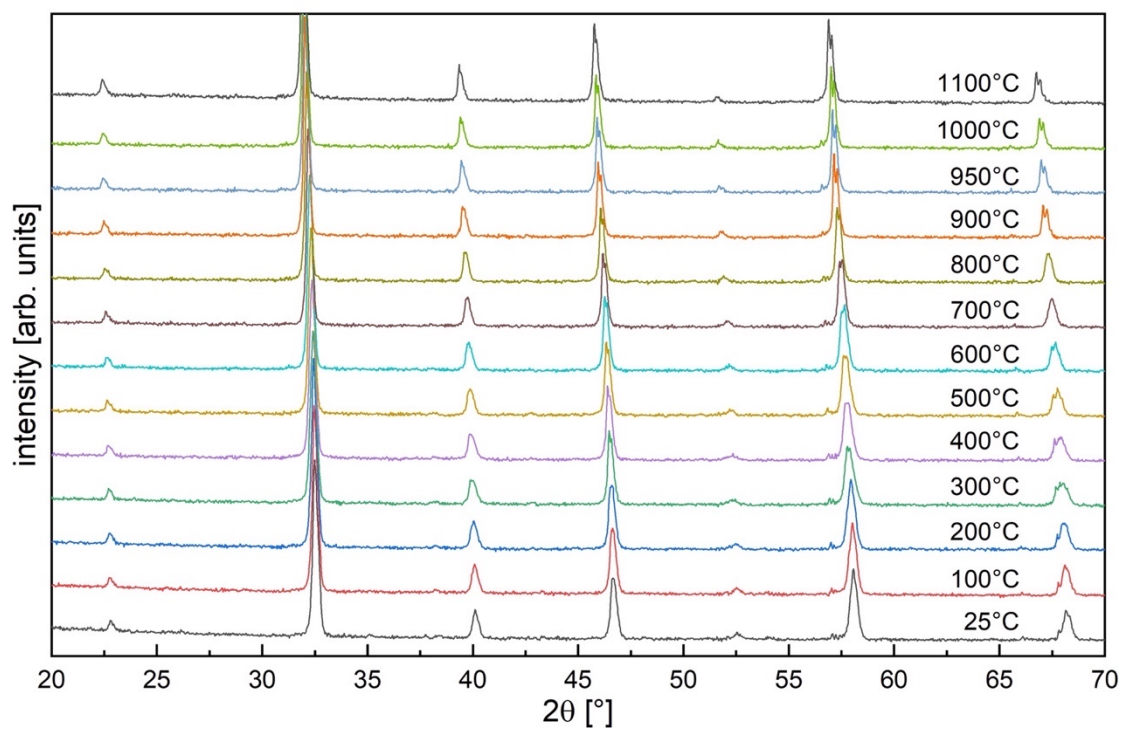


Figure 28: HT-XRD diffraction patterns of LCSF622 during cooling.

The actual cation compositions of the synthesized compounds were determined by ICP-AES. For this purpose, two samples of 50 mg each were dissolved in 3 ml HCl, respectively 3 ml H₂O₂, and filled up to 50 ml volume using the same solvent. Two aliquots each of the sample solutions obtained were diluted 1:100 and analyzed. As a supplement and for comparison, LSCF6482 was also analyzed. All measurements were carried out at FZJ using an iCAP 7600. The data obtained from the measurements are shown in Table 6, whereby the mean value (MV) and the standard deviation (SD) are given in weight percent. The theoretical values (expected from the targeted compound stoichiometry) are given in parentheses, and “Δ” denotes the differences between the experimentally determined mean values and the theoretically expected values. Translated into stoichiometric values, the adjusted chemical formulas are shown in Table 7, whereas the measured percentage of the cations are summed up to 100%, which corresponds to two cation sites, and the measured values of oxygen are neglected here. These values are taken into account in Table 13 with an adjustment in the course of a combustion analysis.

Table 6: Fraction of cations in weight percent

Element [wt.%]	LCF82			LCFC8282			LCSF622			LSCF6428		
	MV	SD	Δ	MV	SD	Δ	MV	SD	Δ	MV	SD	Δ
La	48.4 (49.8)	0.9	2.9	46.7 (49.7)	0.9	6.0	37.3 (39.2)	0.3	4.8	36.5 (36.6)	0.3	0.3
Sr							9.06 (8.2)	0.08	10.0	15.54 (15.9)	0.19	2.4
Ca	3.44 (3.6)	0.07	4.3	3.44 (3.6)	0.06	4.0	3.65 (3.8)	0.07	3.1			
Co				6.02 (5.3)	0.08	14.2				5.37 (5.4)	0.04	0.3
Fe	23.40 (25.0)	0.4	6.6	18.7 (20.0)	0.4	6.4	24.5 (26.3)	0.2	6.7	19.67 (20.3)	0.13	3.1

Table 7: Adjusted stoichiometries derived from ICP-AES

Theoretical formula	Adjusted formula
$\text{La}_{0.8}\text{Ca}_{0.2}\text{FeO}_{3-\delta}$	$\text{La}_{0.82\pm 0.01}\text{Ca}_{0.20}\text{Fe}_{0.98\pm 0.02}\text{O}_{3-\delta}$
$\text{La}_{0.8}\text{Ca}_{0.2}\text{Fe}_{0.8}\text{Co}_{0.2}\text{O}_{3-\delta}$	$\text{La}_{0.78\pm 0.02}\text{Ca}_{0.20}\text{Fe}_{0.78\pm 0.02}\text{Co}_{0.24}\text{O}_{3-\delta}$
$\text{La}_{0.6}\text{Ca}_{0.2}\text{Sr}_{0.2}\text{FeO}_{3-\delta}$	$\text{La}_{0.60}\text{Ca}_{0.20}\text{Sr}_{0.23}\text{Fe}_{0.97\pm 0.01}\text{O}_{3-\delta}$
$\text{La}_{0.6}\text{Sr}_{0.4}\text{Co}_{0.2}\text{Fe}_{0.8}\text{O}_{3-\delta}$	$\text{La}_{0.59}\text{Sr}_{0.40}\text{Co}_{0.21}\text{Fe}_{0.80\pm 0.01}\text{O}_{3-\delta}$

In comparison to LSCF6428, the deviations between theoretically expected and experimentally determined cation compositions are slightly larger for LCF82, LCFC8282, and LCSF622. Since

LSCF6428 is synthesised in the same way as the other materials, it is not expected to differ so strongly. As stated in section 4.8, the formation of oxygen vacancies is essential in order to achieve ionic conductivity as well as oxygen diffusivity. However, regarding the results in Table 7, it is to remark, that furthermore a combustion analysis was carried out. Given this, the above values are not ultimate since the presence of water and oxygen may falsify the oxygen content. The adjusted values are presented in chapter 5.5, which is especially important for LCSF622, since a stoichiometric value for oxygen above 3 is not expected in an acceptor-doped compound with this chemical composition.

5.2. Thermal Properties

As stated, the first step to determine the TEC was to prepare dense pellets. In Table 8, the relative density of the pellets used for the experiment is listed, as well as the sinter temperature determined by the sinter study. This temperature can also be seen as the first guess in order to find good sintering conditions for cathode layer manufacturing.

Table 8: Pellet density (after sintering) and sinter temperature. Values for LCF82 from *Berger et al.* [12]

	LCF82	LCFC8282	LCSF622
Theoretical density [g/cm ³]	6.3195	6.338	6.014
Relative density [%]	97	99	95
T _{sint} [°C]	1100	1100	1100

Given these high density values, it can be assumed that no post-sintering during the TEC measurement occurred and the measured expansions can be considered to originate exclusively from thermal- and chemical expansion, respectively, of the material. The evaluation of the measured data from the TEC experiments is shown in Figure 29 to Figure 31.

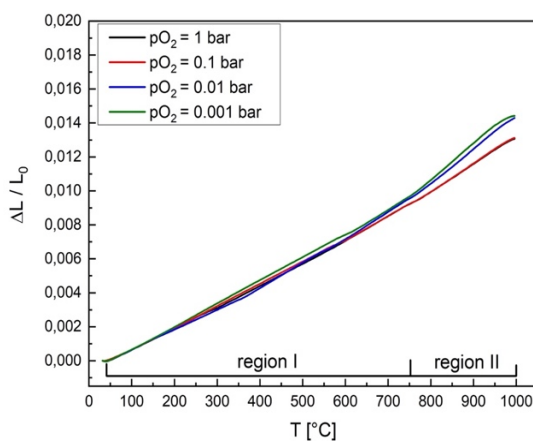


Figure 29: Expansion curve LCF82.

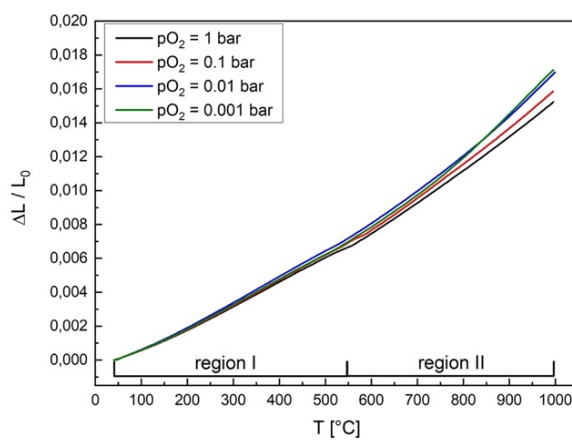


Figure 30: Expansion curve LCFC8282.

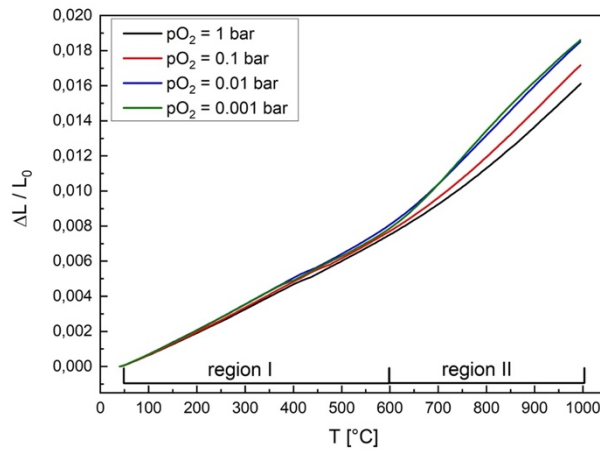


Figure 31: Expansion curve LCSF622.

Two regions can be identified in the expansion curves of all materials. The first one is independent from the pO_2 , indicating purely thermal expansion. In the second, the slope inclines according to the changing oxygen conditions. In this range, chemical expansion contributes to the total expansion caused by the formation of oxygen vacancies under reducing atmospheres at elevated temperatures, due to the removal of oxygen ions from the perovskite crystal. This causes Coulomb repulsion between B-site cations, which are positively charged. Furthermore, the reduction of Fe^{4+} to Fe^{3+} induces strain in the crystal lattice [48]. In Table 9, the TEC values determined for our materials are compared to those of LSCF6428, whereby region I – for LSCF6428 – is between 200-700°C and region II between 800-980°C in air [49]. In comparison with the most common electrolyte material 8YSZ, with a TEC in the range of $10.8 \times 10^{-6} \text{ 1/K}$ [50], and the diffusion barrier material GDC20, with $12.5 \times 10^{-6} \text{ 1/K}$ [51], the materials show slightly larger TECs in region I. In region II, deviations become more pronounced as the TECs increase.

Table 9: TEC values in comparison with other SOFC materials

pO ₂ [bar]	region I, TEC [10 ⁻⁶ /K]				region II, TEC [10 ⁻⁶ /K]			
	LCF82	LCFC8282	LCSF622	LSCF6428	LCF82	LCFC8282	LCSF622	LSCF6428
1	12.8	12.8	13.5		15.8	19.2	21.8	
0.1	12.8	13.6	13.9	16.2	16.0	20.0	23.9	28.0
0.01	13.3	14.1	14.5	@	19.4	21.7	26.4	@
0.001	13.5	13.7	14.1	0.2 bar	19.2	22.7	27.1	0.2 bar

The highest TECs are found for LCSF622. It may be assumed that due to its high TEC values in comparison to GDC20 and 8YSZ, thermal cracks after sintering occur, which can be seen in Figure 34. Those cracks are also present in LCF82 as it is visible in Figure 32, whereby length and depth of the cracks vary and are more significant in LCSF622. In contrast, LCFC8282 shows very smooth and homogeneous cathode layers, as displayed in Figure 33, which might be due the sinter active cobalt. Regardless of crack formation, all cathode layers were firmly attached to the substrate and showed no sign of delamination. In Figure 32 to Figure 34, 50x50 mm² cells are displayed after sintering, for fabrication parameters see Table 29.

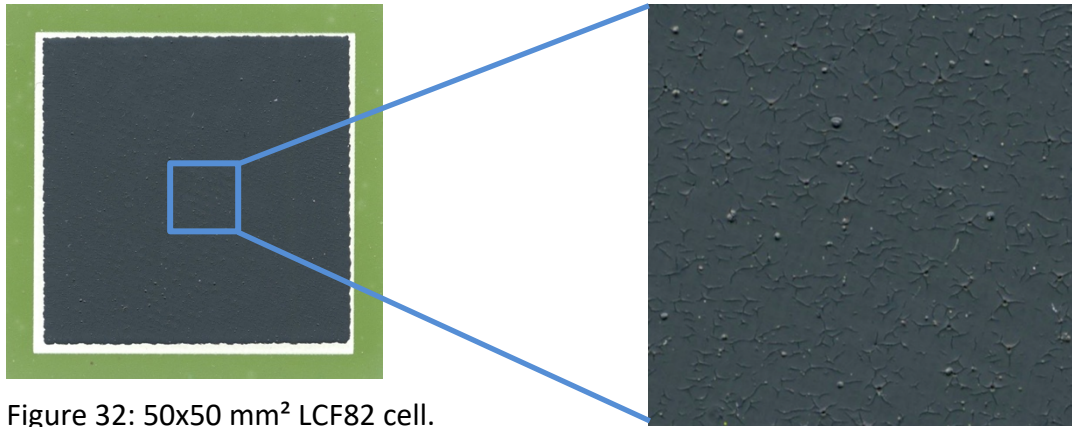


Figure 32: 50x50 mm² LCF82 cell.

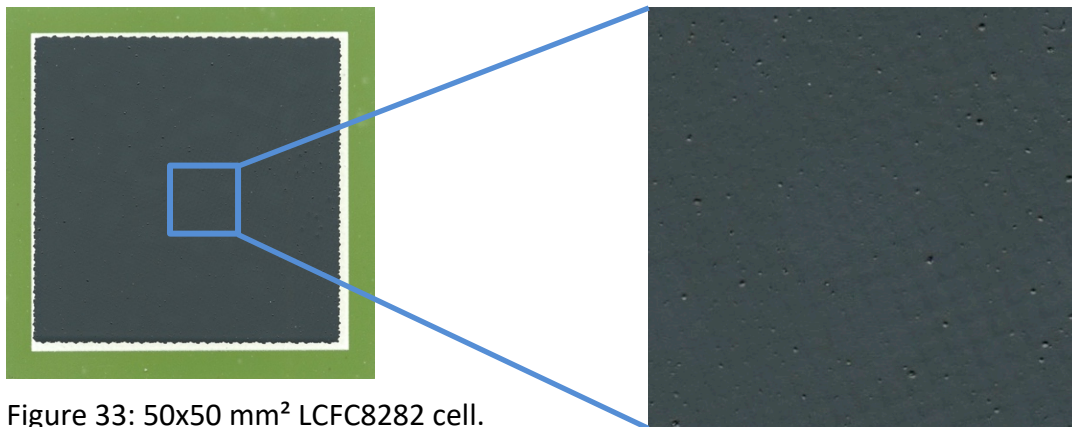


Figure 33: 50x50 mm² LCFC8282 cell.

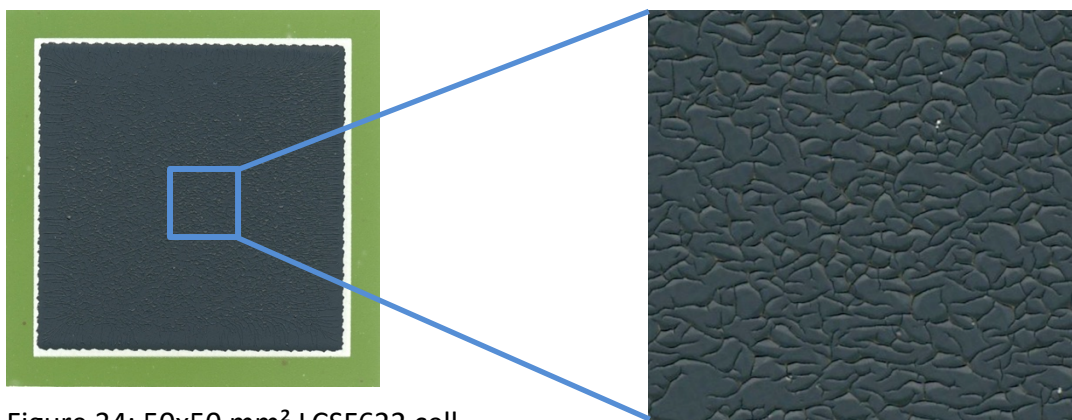


Figure 34: 50x50 mm² LCSF622 cell.

For DSC measurements, we used powders obtained by crushing and mortaring the respective pellets from the TEC experiments. The investigations were carried out with a high-temperature-DSC Netzsch DSC 404 C Pegasus[®] with TASC 414/3A controller and PU1 power unit. The sample was heated from room temperature to 1000°C using 10 K/min as heating (and cooling) rate, whereby the reference sample was an empty platinum crucible. The data were analyzed with the Netzsch Proteus software, and subsequently exported and normalized using the software Origin (OriginLab). The obtained DSC curves of all three materials are compared in Figure 35.

In the case of LCF82 and LCFC8282, a peak occurred in the DSC curve (compare Figure 35), which indicates either a structural or phase transformation. In the first case, the basic Bravais lattice remains the same and a realignment of the structure occurs, e.g. the angle of the oxygen octahedra changes, whereas in the latter the crystal lattice type changes, e.g. from

orthorhombic to trigonal [52]. Since all transformations from the investigated materials are considered to be structural transformations, this is in accordance with the HT-XRD results in chapter 4.6.1, whereby the transition temperature is slightly higher under DSC measurement conditions, due to the high heating rate. Both materials revealed that the transformation is fully reversible.

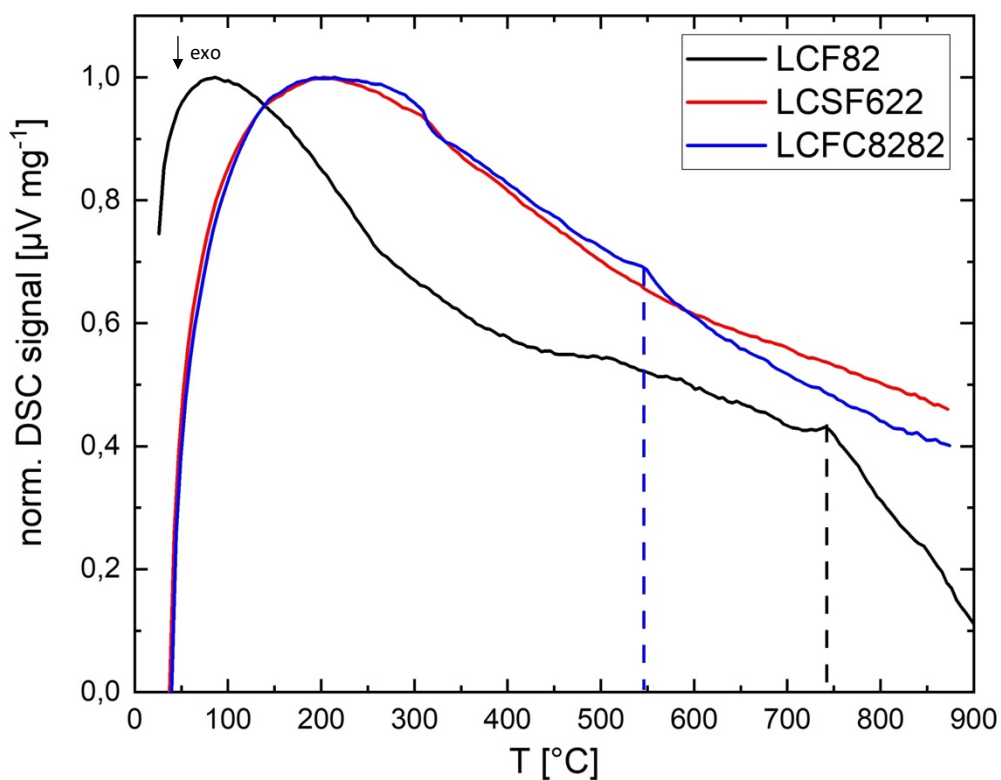


Figure 35: DSC at $p\text{O}_2 = 0.2$ bar.

5.3. Electronic Conductivity

The electronic conductivities and the corresponding activation energies of the investigated materials are displayed in Figure 36 to Figure 40. In addition, Table 10 shows the values determined in the temperature range between 600–800°C in comparison to those of LSCF6428, which values are valid for pO_2 0.01-1 bar and between 400–800°C [49].

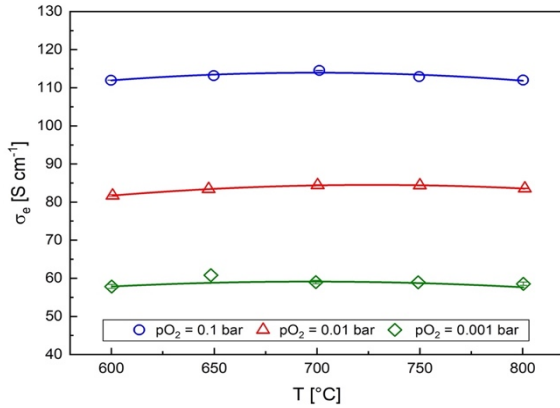


Figure 36: σ_e of LCF82.

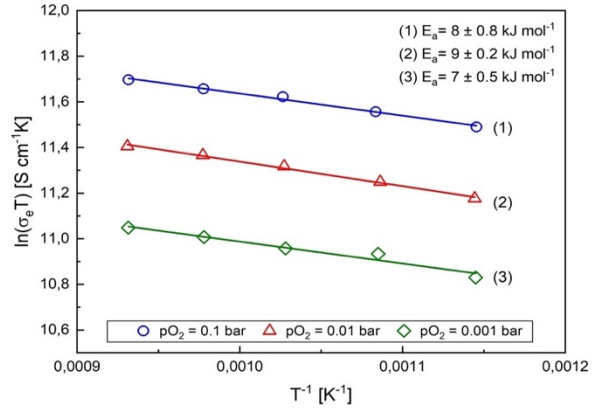


Figure 37: Arrhenius plot σ_e of LCF82.

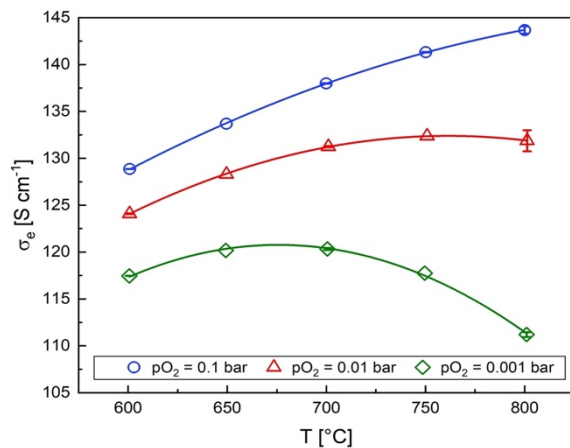


Figure 38: σ_e of LCFC8282.

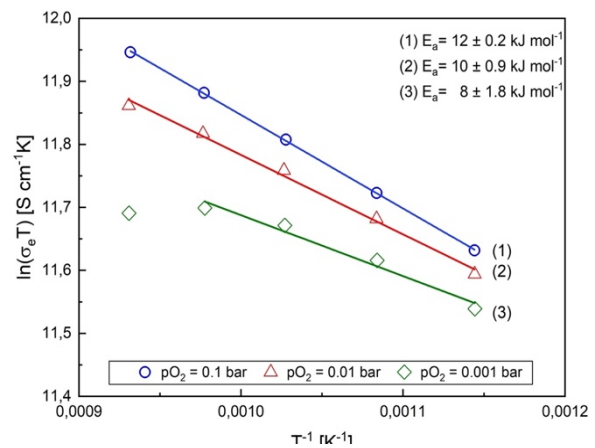


Figure 39: Arrhenius plot σ_e of LCFC8282.

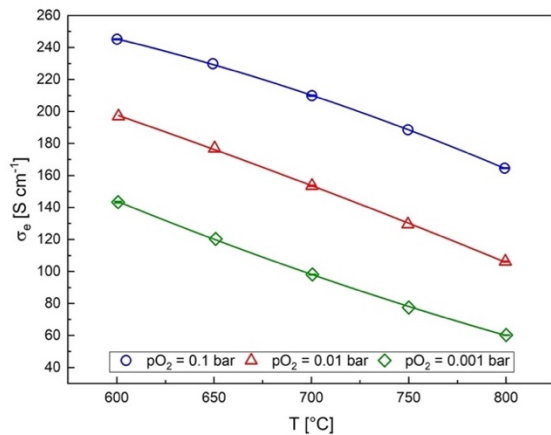


Figure 40: σ_e of LCSF622.

Table 10: Activation energies of electronic conductivity of various materials for different oxygen partial pressures in [kJ mol⁻¹]

pO ₂ [bar]	LCF82		LCFC8282		LCSF622		LSCF6428	
	E _a	SD	E _a	SD	E _a	SD	E _a	SD
0.1	8	± 0.8	12	± 0.2			7	± 0.1
0.01	9	± 0.2	10	± 0.9	-	-		
0.001	7	± 0.5	8	± 1.8			-	-

As stated in the introduction, electronic conductivity values in the order of magnitude of 100 Scm⁻¹ are sufficient for mixed ionic-electronic conductors in order to maintain the electrochemical reactions within a fuel cell. With the exception of LCF82 (at low pO₂), all of our materials fulfill this requirement. Therefore, lateral and bulk electronic conductivity are not expected to show a bottleneck in cell performance. With about 300 Scm⁻¹ at operating temperature (600-800°C), LSCF6482 exhibits higher electronic conductivity than the new materials.

LCF82 shows a direct correlation between pO₂, electronic conductivity and temperature, with the activation energies being in the range expected for p-type small polaron hopping conductors, which was already described by *Benali et al.* [53]. In comparison, LCFC8282 shows higher activation energies and, after reaching a maximum at 700°C, a decrease in electronic conductivity with increasing temperature at lower pO₂. Since cobalt was expected to increase the electronic conductivity, which it clearly does (in comparison with values for the Co-free compound LCF82), this may not be intuitive. However, the decrease in the electronic conductivity at higher temperatures and lower pO₂ can be explained by the formation of oxygen vacancies (and the corresponding consumption of p-type charge carriers [M_M[•]] (M=Fe, Co). This explanation is also applicable to the electronic conductivity of LCSF622, which should form even higher concentrations of oxygen vacancies due to the higher amount of acceptor substitution [54].

5.4. Oxygen Exchange Kinetics

The chemical surface exchange coefficients k_{chem} and the chemical diffusion coefficients D_{chem} of oxygen of all investigated materials are shown in Figure 41 to Figure 45. The majority of the evaluated data revealed that the oxygen exchange kinetics are primarily limited by the surface exchange. The thicknesses of the samples, which were used for conductivity relaxation experiments in van der Pauw geometry are displayed in Table 11.

With LCSF622, only surface exchange coefficients could be determined, since the kinetics was rate-limited by the surface exchange process. In order to determine diffusion coefficients, an even thicker LCSF622 sample would have been needed (presumably > 1mm). LCF82 as well as LCFC8282 showed mixed-controlled kinetics at an oxygen partial pressure of 0.1 bar. Thus, both surface exchange- and diffusion coefficients could be measured. Data for LCF82 was previously published by *Berger et al.* [12].

Table 11: vdP sample thickness

Material	d [μm]
LCF82	503
LCFC8282	450
LCSF622	576

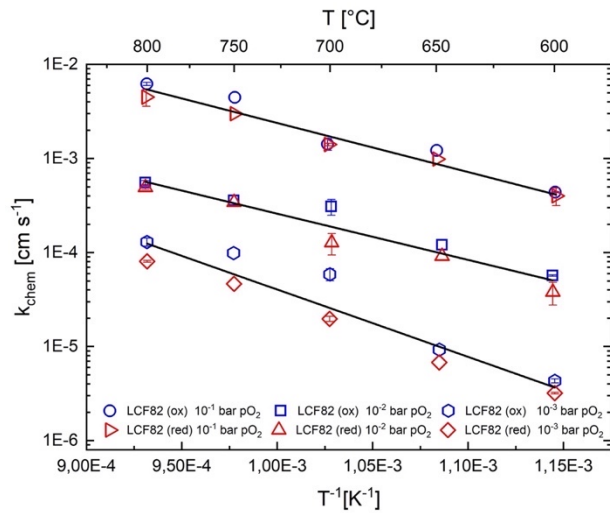


Figure 41: k_{chem} of LCF82.

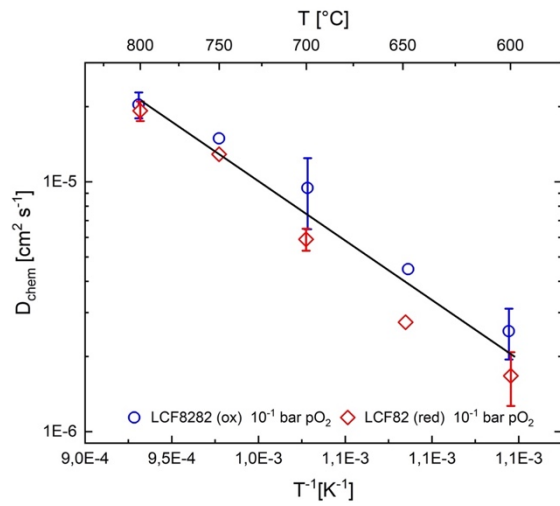


Figure 42: D_{chem} of LCF82.

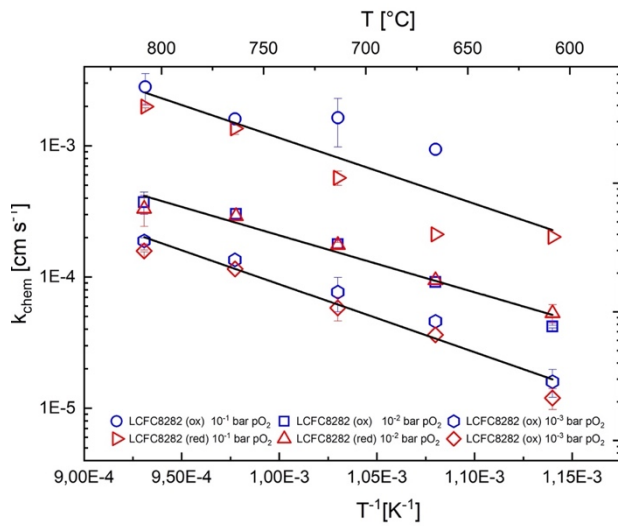


Figure 43: k_{chem} of LCFC8282.

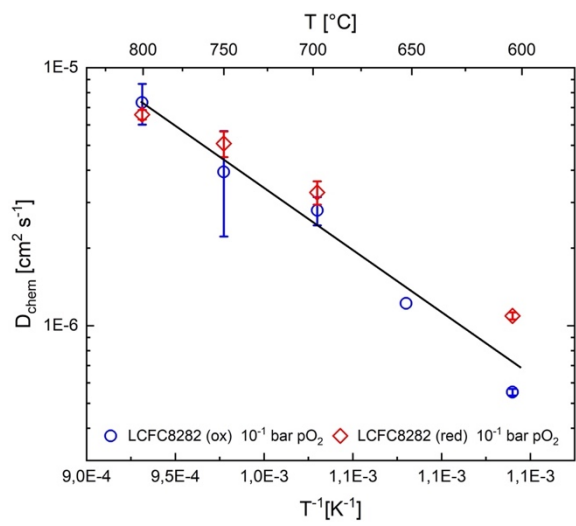


Figure 44: D_{chem} of LCFC8282.

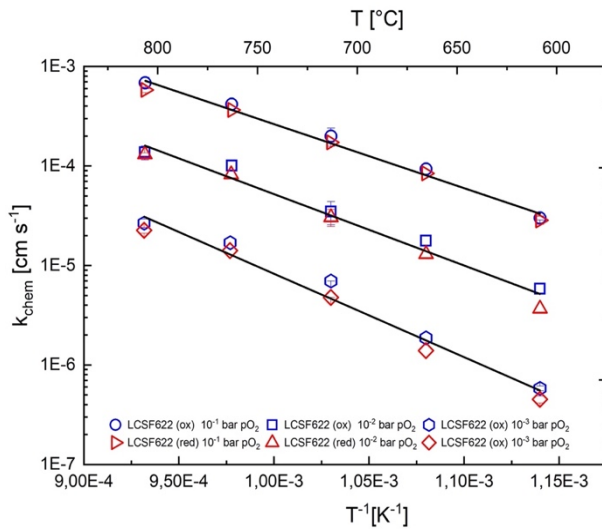


Figure 45: k_{chem} of LCSF622.

5.5. Oxygen Non-Stoichiometry

The measurement was carried out at FZJ using a Leco TCH600 and the results are shown in Table 12, whereby the oxygen and hydrogen contents from three measurements each and the standard deviation (SD) in weight percent are given. The theoretical values are given in parentheses. Further data processing and the interpretation is given in section 5.1.; for comparison, LSCF6482 was also analyzed.

Table 12: Results of the non-metal analysis

Sample [wt.%]	Oxygen		Hydrogen	
	content	SD	content	SD
LCF82	21.19 (21.5)	0.05	0.0248 (0)	0.0018
LCFC8282	21.15 (21.5)	0.03	0.0284 (0)	0.0018
LCSF622	22.63 (22.6)	0.1	0.0308 (0)	0.0008
LSCF6428	21.2 (21.8)	0.13	0.021 (0)	0.005

As mentioned in section 5., values listed there were not adjusted for the oxygen content. The adjusted stoichiometric ratios are listed in Table 13.

Table 13: Adjusted stoichiometry

Non-Adjusted formula	Adjusted formula
$\text{La}_{0.82\pm0.01}\text{Ca}_{0.20}\text{Fe}_{0.98\pm0.02}\text{O}_{3-\delta}$	$\text{La}_{0.77\pm0.01}\text{Ca}_{0.19}\text{Fe}_{0.93\pm0.02}\text{O}_{2.93\pm0.01}$
$\text{La}_{0.78\pm0.02}\text{Ca}_{0.20}\text{Fe}_{0.78\pm0.02}\text{Co}_{0.24}\text{O}_{3-\delta}$	$\text{La}_{0.75\pm0.01}\text{Ca}_{0.19}\text{Fe}_{0.75\pm0.02}\text{Co}_{0.23}\text{O}_{2.92}$
$\text{La}_{0.60}\text{Ca}_{0.20}\text{Sr}_{0.23}\text{Fe}_{0.97\pm0.01}\text{O}_{3-\delta}$	$\text{La}_{0.57}\text{Ca}_{0.19}\text{Sr}_{0.22}\text{Fe}_{0.93\pm0.01}\text{O}_{2.98\pm0.01}$
$\text{La}_{0.59}\text{Sr}_{0.40}\text{Co}_{0.21}\text{Fe}_{0.80\pm0.01}\text{O}_{3-\delta}$	$\text{La}_{0.58}\text{Sr}_{0.39}\text{Co}_{0.20}\text{Fe}_{0.78\pm0.01}\text{O}_{2.99\pm0.02}$

As anticipated, the oxygen content decreased due to adjustment in comparison to the non-adjusted formula. The adjusted compositions can be interpreted to reflect the real oxygen content in the crystal unit cell. Furthermore, the values are also adjusted due to the hydrogen content, since the premise is that hydrogen exists under ambient conditions in the materials as H_2O . Therefore, it can be stated, that for every two parts of hydrogen, also one part of oxygen can further be removed.

5.6. Electrochemical Properties

5.6.1 $\text{La}_{0.8}\text{Ca}_{0.2}\text{FeO}_{3-6}$

In the beginning, a series of 16 symmetric cells were printed (cells #1-16 in Table 26), with the aim to determine the optimum sintering conditions. For this purpose, the sintering temperatures were varied from 1040°C to 1100°C, with a stepwise temperature increase of 20°C and a sintering time of 3 h. Measurements were performed on four samples obtained by sintering at the respective temperature. The results are given in Figure 46. Further, after surveying the cells, a current collecting LSM20 layer (\varnothing 8 mm) was printed on top of the LCF82 cathodes of cells 1-4, and sintered with 950°C for 2 h, since the in-plane resistance of LCF82 was higher than expected. It was assumed that this was due to the insufficient lateral electronic conductivity, and LSM as a good electronic conductor was expected to help overcome this issue. The results are shown in Figure 47. The orange and the blue boxes represent the mean value and standard derivation of all LCF82, respectively LCF82/LSM, cells sintered at 1040°C, respectively 1040°C/950°C. SEM images of a cell with promising performance (cell #2) and an insufficiently performing cell (cell #3) revealed no major differences in the microstructure. The porosity was determined to be around 54%, which is above literature values of 40% for LSCF6428 cathodes [45]. The evaluation of cells sintered at 1100°C (cell #14 and cell #16) revealed that a porosity of 43% was achieved, which is closer to the targeted values. Therefore, a given correlation between sinter temperature and porosity can be assumed. The GDC20 interlayer of all investigated cells showed a porosity of 47%, which is as well above literature values with 35% [45]. Nevertheless, since the substrate and GDC20 interlayer was manufactured in accordance with in-house standards of FZJ, this deviation is considered to be negligible, especially when considering a mean layer thickness of 7 μm .

As shown in Figure 46, the differences in R_{pol} and R_{tot} between the samples subjected to different sintering temperatures are small. The assumption that the resistances may decrease with decreasing sintering temperature is inconclusive, since the data points (partly) overlap within the limits of error. The application of an additional LSM current collector on top of the cathode does not result in the expected improvement. Whereas R_{pol} tends to be even higher than on a pure LCF82 cathode, the relatively large standard deviation in R_{pol} does not allow for a clear conclusion. The averaged activation energy as well as the standard deviation for the given sintering temperatures are shown in Table 14, whereby a low-temperature (< 700°C) and a high temperature activation energy (> 700°C) can be determined. When considering cells 1.2-4.2, an increase in ASR_{Ω} as well as in the SD can be observed, which verifies that additional current collector layers on top of LCF82 cells do not deliver the expected results, as seen in Figure 47. In Figure 48 and Figure 49, a cross-section and its magnification of cell #2 is shown. Layer adhesion is clearly given and the microstructure of the LCF82 cathode as well as that of the LSM layer is as expected. Therefore, cell performance seems to be below the expectations due to the sintering conditions. To overcome this issue, LSCF6428 standard sintering conditions with a sintering temperature of 950°C and dwell time of 2 h was chosen for further attempts. All further LSCF6428 values for comparison seen in the figures are from Szász *et al.* [45].

Table 14: Activation energies for cells 1-16

Cell number	T [°C]	E _a of ASR _Ω (R _{tot}) [eV]				E _a of ASR _{cat} (R _{pol}) [eV]			
		> 700°C		< 700°C		> 700°C		< 700°C	
		MV	SD	MV	SD	MV	SD	MV	SD
1.1-4.1	1040	0.59	0.06	1.15	0.04	1.54	0.08	1.63	0.03
1.2-4.2	950	0.67	0.15	1.23	0.14	1.51	0.16	1.61	0.08
5-8	1060	0.54	0.06	1.04	0.05	1.36	0.02	1.58	0.03
9-12	1080	0.49	0.04	1.00	0.06	1.36	0.06	1.62	0.03
13-16	1100	0.55	0.06	1.07	0.08	1.46	0.14	1.63	0.10

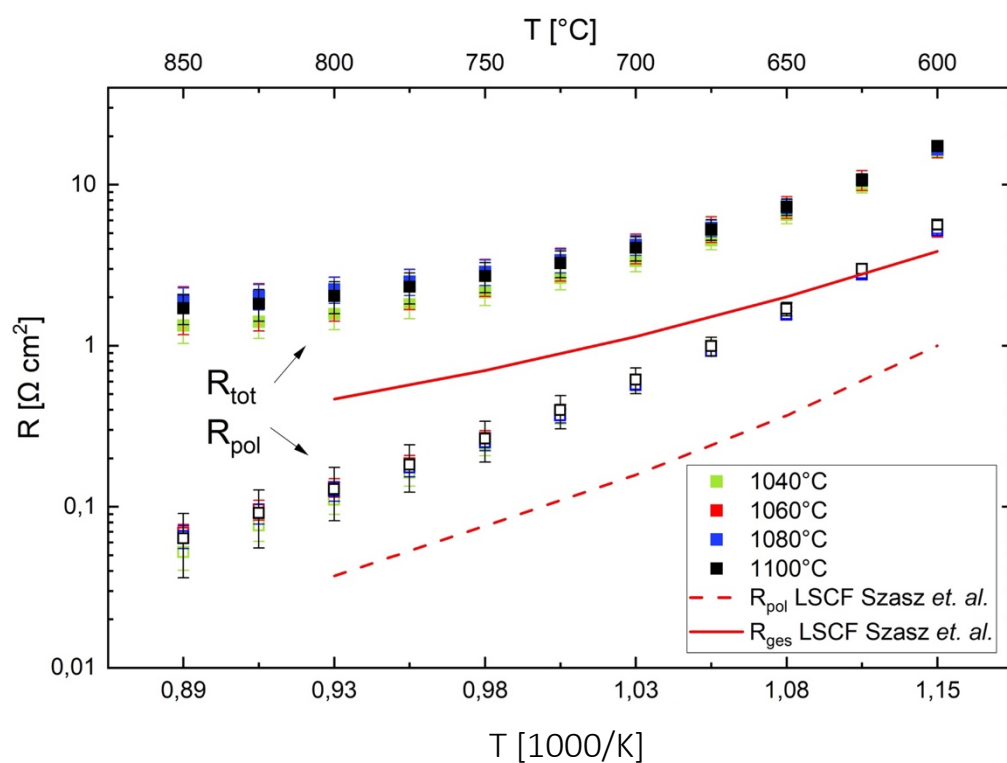


Figure 46: ASR of LCF82 cells from first sinter attempt.

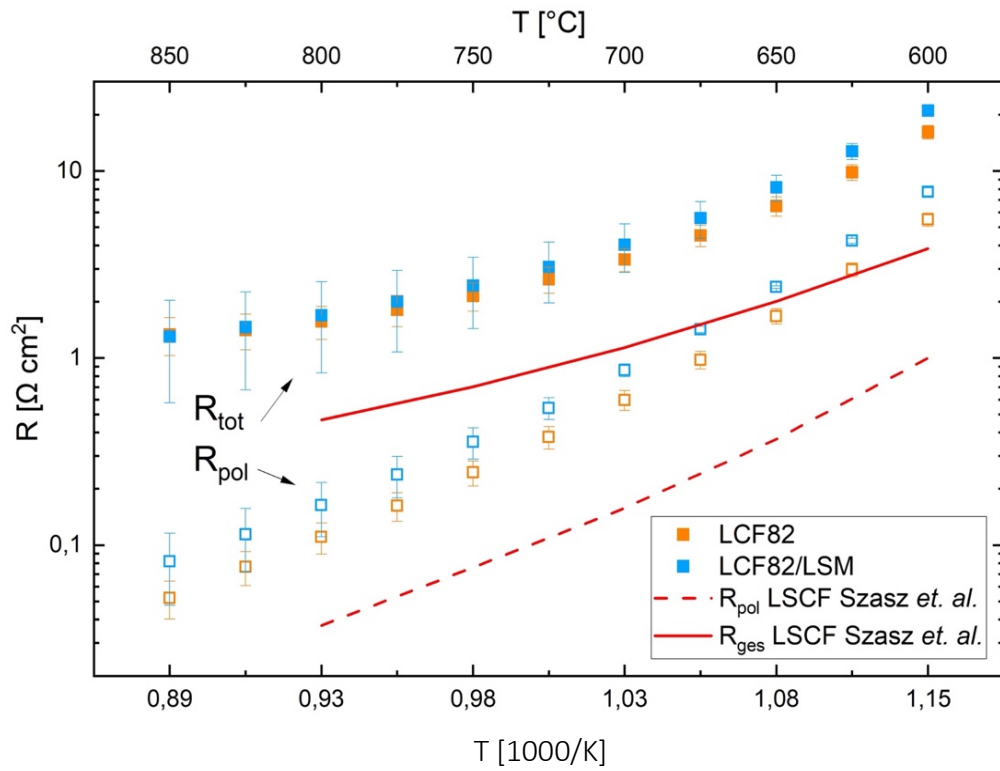


Figure 47: ASR of LCF82 cells with LSM current collector.

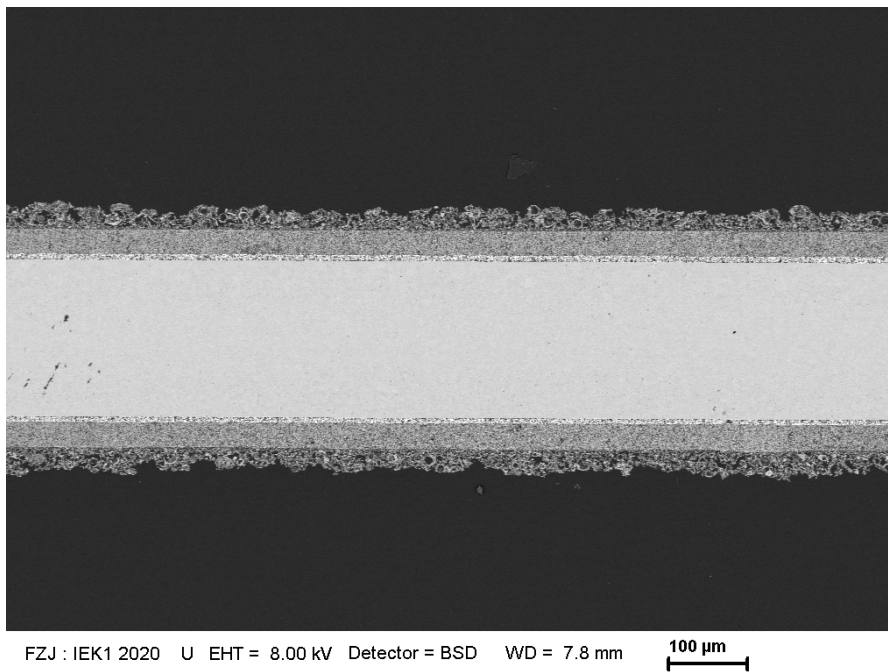


Figure 48: SEM cross-section of LCF82/LSM cell #2.

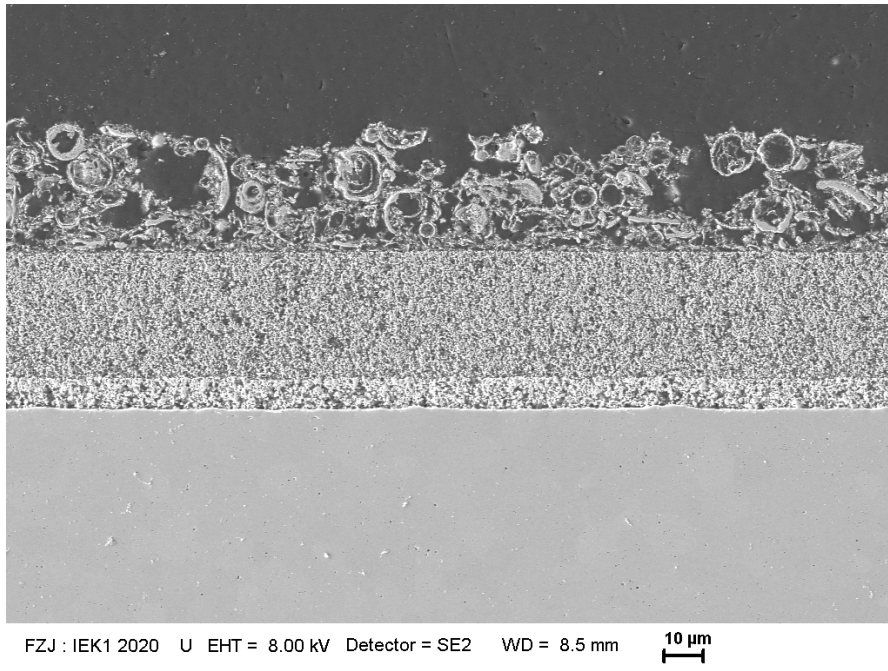


Figure 49: SEM cross-section magnification of LCF82/LSM cell #2.

Sintering at 950°C delivered better results and was therefore chosen as a starting temperature for all further cells. One more attempt to overprint LCF82 cathodes with an LSM layer was done, whereby co-sintering took place by using 950°C for 2 h (cells #19-20). The microstructure of the LSM layer was in this case adjusted to resemble that of the cathode rather than the coarser current collector. The finer microstructure was realized by using starting powder with much smaller PSD (see Table 2). The result is shown in Figure 50.

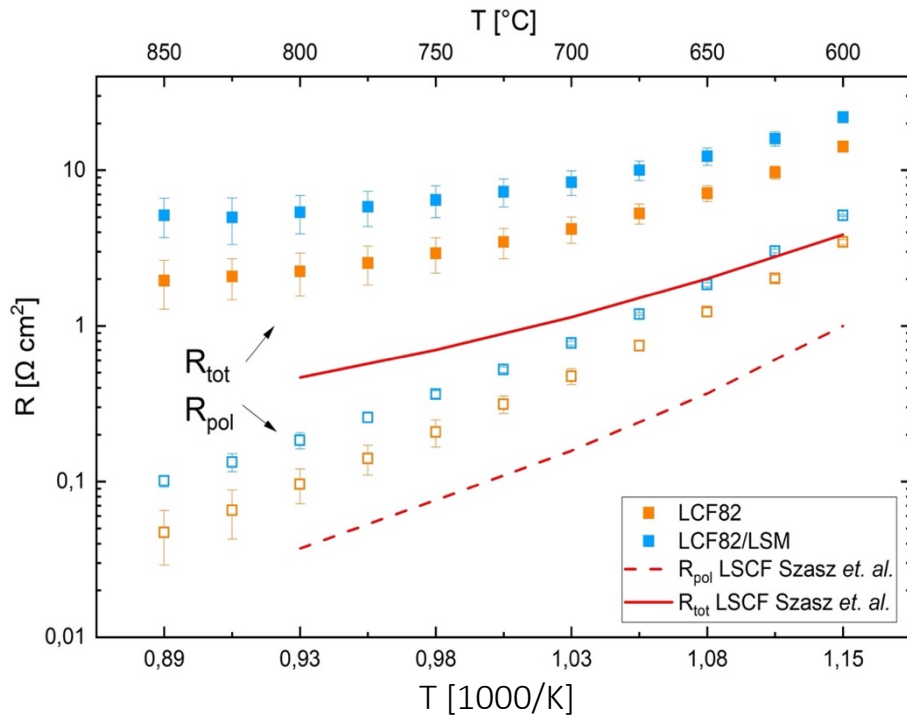


Figure 50: ASR of LCF82 cells with additional LSM cathode.

As before, R_{pol} and R_{tot} again increased drastically by adding the LSM layer, whereas the pure LCF82 cathode sintered with 950°C (cells #17-18) showed increased performance also in comparison to cells 1-16. The activation energies for cells #17-20 are displayed in Table 15. Although activation energy for cells #19-20 tends to be the lowest in the whole LCF82 test series, ASR_{Ω} and ASR_{cat} increased noticeable. Due to this result, no further attempts regarding a current collector layer were performed.

Table 15: Activation energies for cells 17-20

Cell number	T [°C]	E _a of ASR _Ω (R _{tot}) [eV]				E _a of ASR _{cat} (R _{pol}) [eV]			
		> 700°C		< 700°C		> 700°C		< 700°C	
		MV	SD	MV	SD	MV	SD	MV	SD
17-18	950	0.49	0.07	0.90	0.06	1.47	0.12	1.46	0.04
19-20	950	0.32	0.05	0.71	0.05	1.28	0.03	1.38	0.01

In order to determine the influence of the cathode microstructure on the performance of cells, cathodes were fabricated from powders of the same material but with different PSDs. Cells with cathodes prepared from LCF82_V1_3_2 powder (smaller particle size, orange symbols in Figure 51, cells #17-18) and LCF82_V3 (increased particle size, blue symbols in Figure 51, cells #33-35) and sintered at 950°C are presented in the same plot. Additional cathodes were sintered at 1000°C (cells #36-38) to check for a correlation between sintering temperature and R_{pol} as well as R_{tot} . Furthermore, a temperature program including heating up to 1100°C with dwell time of 30 min and then cooling down and dwelling 90 min at 950°C (cells #45-46) was

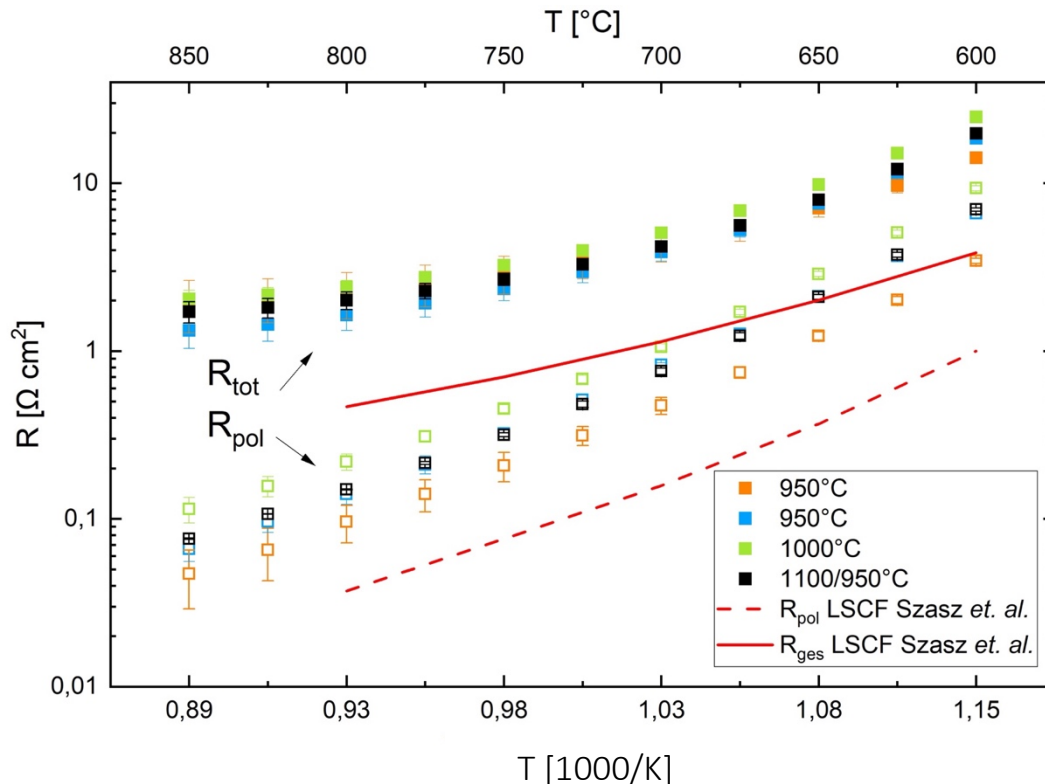


Figure 51: ASR of LCF82 cells prepared with different sintering temperatures and printing pastes.

tested. The aim was to achieve a more favorable porosity, as previously achieved for LCF82 cells sintered at 1100°C. All data are shown in Figure 51, activation energies are given in Table 16.

As it can be seen in the results of the ASR, no direct correlation between the sintering temperature and R_{pol} as well as R_{tot} can be observed for LCF82. When comparing the values obtained for cathodes sintered at 1000°C with those sintered at 1100°C in Figure 46, latter R_{pol} values are lower than the first ones. At the same time, the ASR of cathodes sintered at 950°C are lower than those of cathodes sintered at 1100°C, which would not be expected. In summary, it can be stated that cells sintered at 950°C show the best results in terms of lowest R_{tot} and R_{pol} achieved with LCF82.

Table 16: Activation energies for cells #33-35, #36-38 & #45-46

Cell number	T [°C]	E _a of ASR _Ω (R _{tot}) [eV]				E _a of ASR _{cat} (R _{pol}) [eV]			
		> 700°C		< 700°C		> 700°C		< 700°C	
		MV	SD	MV	SD	MV	SD	MV	SD
33-35	950	0.68	0.06	1.15	0.06	1.61	0.05	1.55	0.05
36-38	1000	0.59	0.04	1.18	0.03	1.40	0.06	1.60	0.02
45-46	1100/ 950	0.57	0.05	1.14	0.02	1.44	0.02	1.63	0.01

The use of composite cathodes is a further way to improve electrochemical properties. Also in this study, mixtures of the cathode material with GDC20 were tested, which represent cells #21-24 in Table 26. Weight ratios of 50:50 and 70:30 were used, since *Yamaguchi et al.* [55] showed good cell performance with given composite cathodes. These results, however, were not reproducible. Since *Yamaguchi et al.* [55] seemed to have used a sinter temperature of 950°C for their composite materials, the analysis of R_{pol} and R_{tot} revealed that other parameters – beside the sinter temperature – must have influenced their results. Since GDC20 layers are sintered at around 1300°C, it can be assumed that by using only 950°C, no percolation and mutual sintering can take place. Since the EIS results did not yield in meaningful data, no results are shown here.

50x50 mm² cell measurements revealed performance below average, whereby only two of three cells were suitable for measurement. The comprehensive data obtained can be found in the appendix, whereby cells 15770-6 (9M0981) and 15770-7 (9M0985) were measured. The ASR obtained at a current density of 0.5 A/cm² at 700°C and 800°C is given in Figure 56. At 800°C and a fuel gas composition consisting of 20% H₂O and 80% H₂, cell 15770-6 showed an OCV of 1 V and cell 15770-7 of 1.028 V, respectively. In order to obtain further insights into the factors limiting the performance, post-mortem analyses were conducted. The SEM images revealed no secondary phases at the cathode-electrolyte interface. Therefore, poor adhesion and thermal cracks are a possible reason for the limited performance. Selected images are shown in Figure 52 to Figure 55. The images indicate a subsurface crack in the outer layer of the cathode, which might be due to sinter conditions. No further sub-surface crack network was observed, which leads to the assumption that thermal mismatch plays a minor role in the

low performance. Since also no abnormal sinter cracks are found in Figure 32, the main reason for the limited performance may be the poor adhesion of the cathode on the electrolyte.

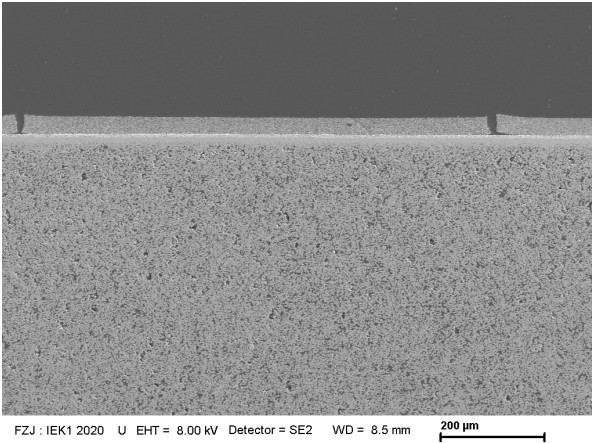


Figure 52: SEM cross-section of LCF82-electrolyte interface.

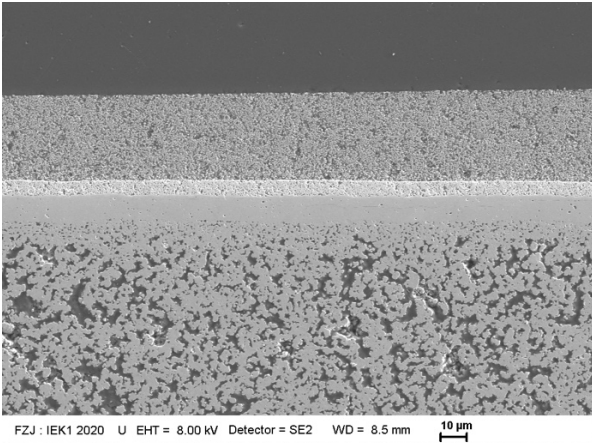


Figure 53: SEM cross-section of LCF82-electrolyte interface.

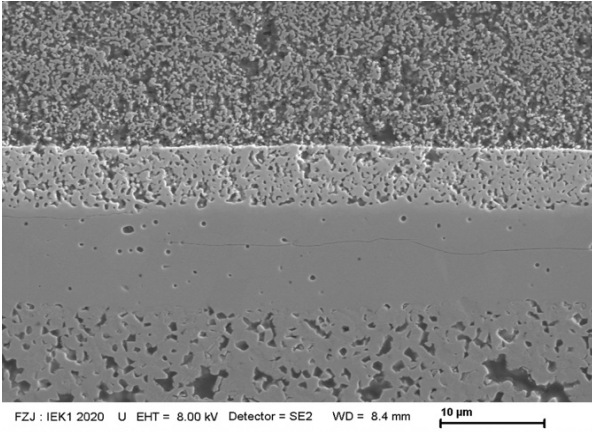


Figure 54: SEM cross-section of LCF82-electrolyte interface with crack.

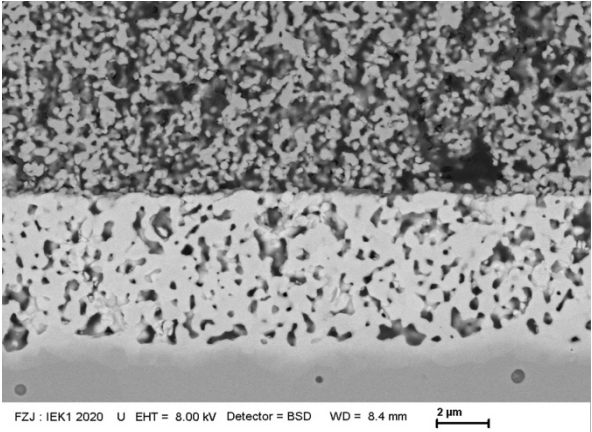


Figure 55: SEM cross-section of LCF82-electrolyte interface.

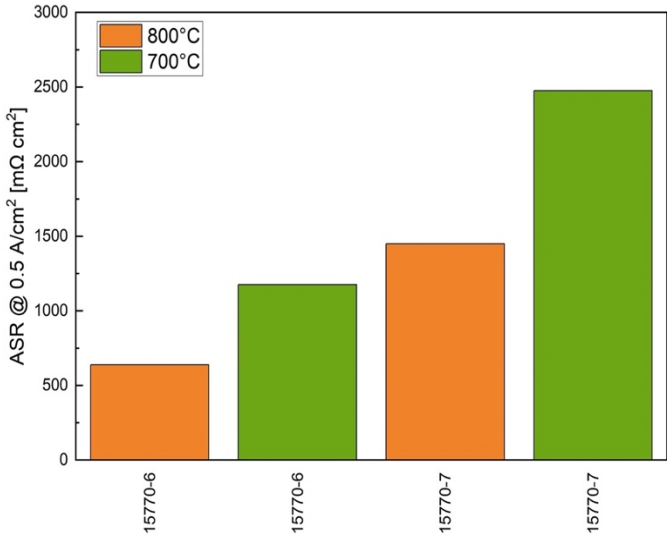


Figure 56: ASR_{tot} of cells with LCF82 cathodes at 0.5 A/cm².

5.6.2 $\text{La}_{0.8}\text{Ca}_{0.2}\text{Fe}_{0.8}\text{Co}_{0.2}\text{O}_{3-\delta}$

As stated in section 5.6.1, 950°C was chosen as a starting temperature for sintering the cathodes (cells # 25-26). As shown in Figure 33, only minor (or no) sinter cracks occurred, which can presumably be ascribed to the cobalt substitution. Since the EIS measurements revealed better performance in comparison to LCF82 but also to LSCF symmetrical cells, the attempt to rise as well as lower sintering conditions by 50°C was carried out (900°C: cells #27-29; 1000°C: #30-32) in order to verify if a direct connection can be identified. The results are shown in Figure 57, whereby activation energies can be found in Table 17.

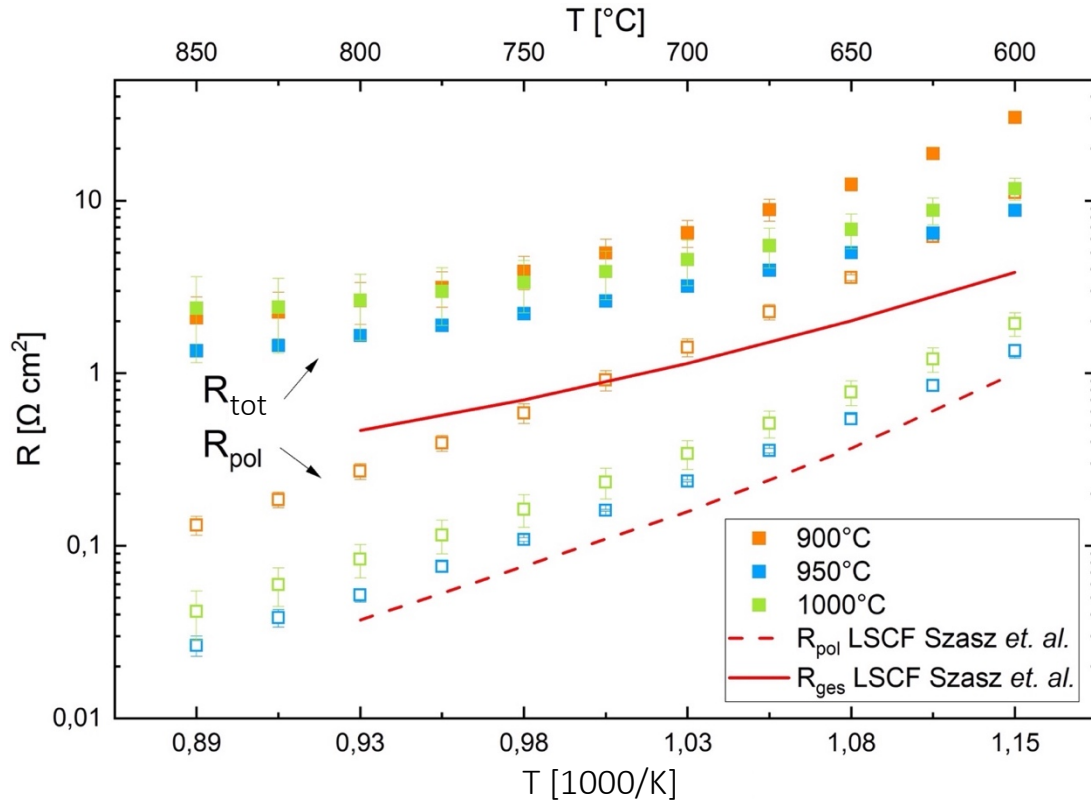


Figure 57: ASR of LCFC8282 symmetrical cells.

Table 17: Activation energies for cells #25-32

Cell number	T [°C]	E_a of ASR_Ω (R_{tot}) [eV]				E_a of ASR_{cat} (R_{pol}) [eV]			
		> 700°C		< 700°C		> 700°C		< 700°C	
		MV	SD	MV	SD	MV	SD	MV	SD
25-26	950	0.54	0.02	0.74	0.03	1.38	0.07	1.27	0.04
27-29	900	0.73	0.07	1.14	0.08	1.49	0.04	1.52	0.07
30-32	1000	0.44	0.11	0.71	0.09	1.34	0.10	1.27	0.03

ASR_Ω and ASR_{cat} of cells sintered at 950°C are very close to state-of-the art LSCF cells. Cobalt substitution seems to help overcome the issue of insufficient lateral electronic conductivity.

Cells sintered at 900°C seem to show lack of percolation, since ohmic losses tend to increase more significantly compared to cells sintered at 1000°C. When compared directly to its unsubstituted counterpart LCF82, LCFC8282 shows the same activation energy in the temperature range below 700°C, whereas at higher temperatures the activation energy is by almost one third higher. Therefore, when regarding only the activation energies, LCF82 shows superior properties. Nevertheless, when considering the ohmic losses, it can be stated that LCFC8282 is outperforming its LCF82 counterpart, as it was expected due to the introduced cobalt.

Again, when it comes to 50x50 mm² cells, LCF82 is outperformed by LCFC8282. This is as expected, since EIS measurements on symmetrical cells were promising. The data obtained can be found in the appendix, whereby cells 15775-4 (9M0992), 15775-7 (9M0993) and 15775-8 (9M1001) were measured. The ASR measured at a current density of 0.5 A/cm² at 700°C and 800°C is shown in Figure 62. At 800°C, cell 15775-4 showed an OCV of 1.002 V, 15775-7 of 1 V and 15775-8 of 1,002 V. Again, post-mortem analyses were conducted, whereby the SEM images revealed no other secondary phases at the cathode-electrolyte interface. Nevertheless, rather voluminous agglomerates are observed, whereas no cracks were found. In addition, the cathode-electrolyte interface looked as expected. Therefore, poor adhesion of the cathode to the electrolyte is a possible cause for the still limited performance. Selected SEM images are shown in Figure 58 to Figure 61.

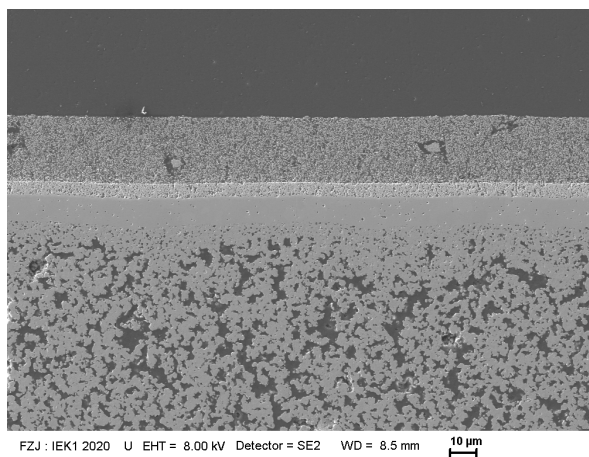


Figure 58: SEM cross-section of LCFC8282-electrolyte interface.

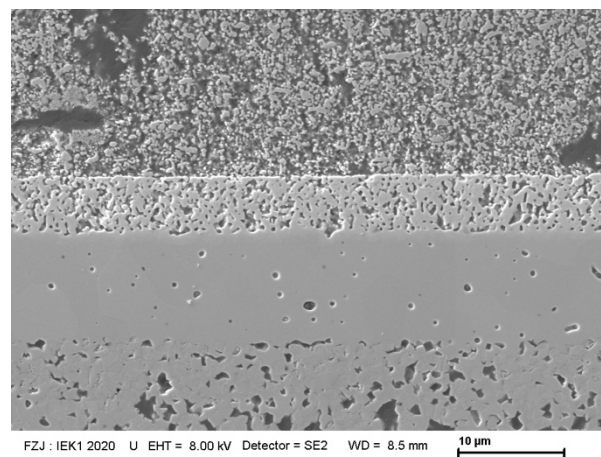


Figure 59: SEM cross-section of LCFC8282-electrolyte interface.

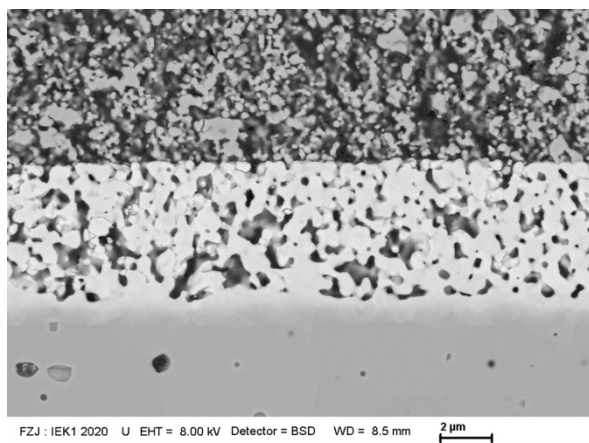


Figure 60: SEM cross-section of LCFC8282-electrolyte interface with GDC layer.

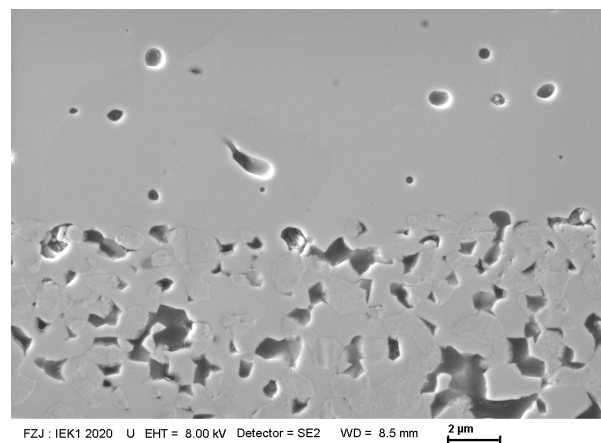


Figure 61: SEM cross-section of LCFC8282-electrolyte/anode interface.

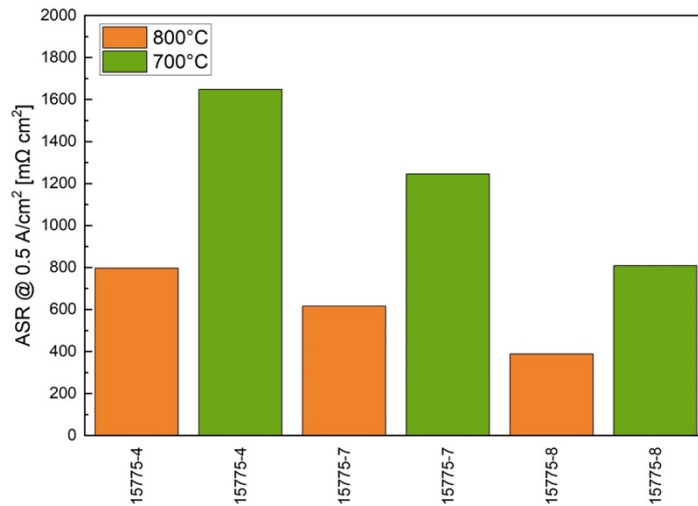


Figure 62: ASR_{tot} of cells with LCFC8282 cathodes at 0.5 A/cm².

5.6.3 La_{0.6}Ca_{0.2}Sr_{0.2}FeO_{3-δ}

For LCSF622, 950°C (cells #39-41) was chosen as a starting temperature for cathode sintering due to the good previous results. For comparability with LCFC8282, additional LCSF622 cathodes were sintered at 1000°C (cells #42-44), whereas 900°C was left out due to the previous experience. In addition, a further attempt with a combination of sintering conditions was carried out. A combination of sintering at 1100°C for 30 min and cooling down with dwell time at 950°C for 90 min, as described in chapter 5.6, was also performed (cells #47-48). The results are shown in Figure 63.

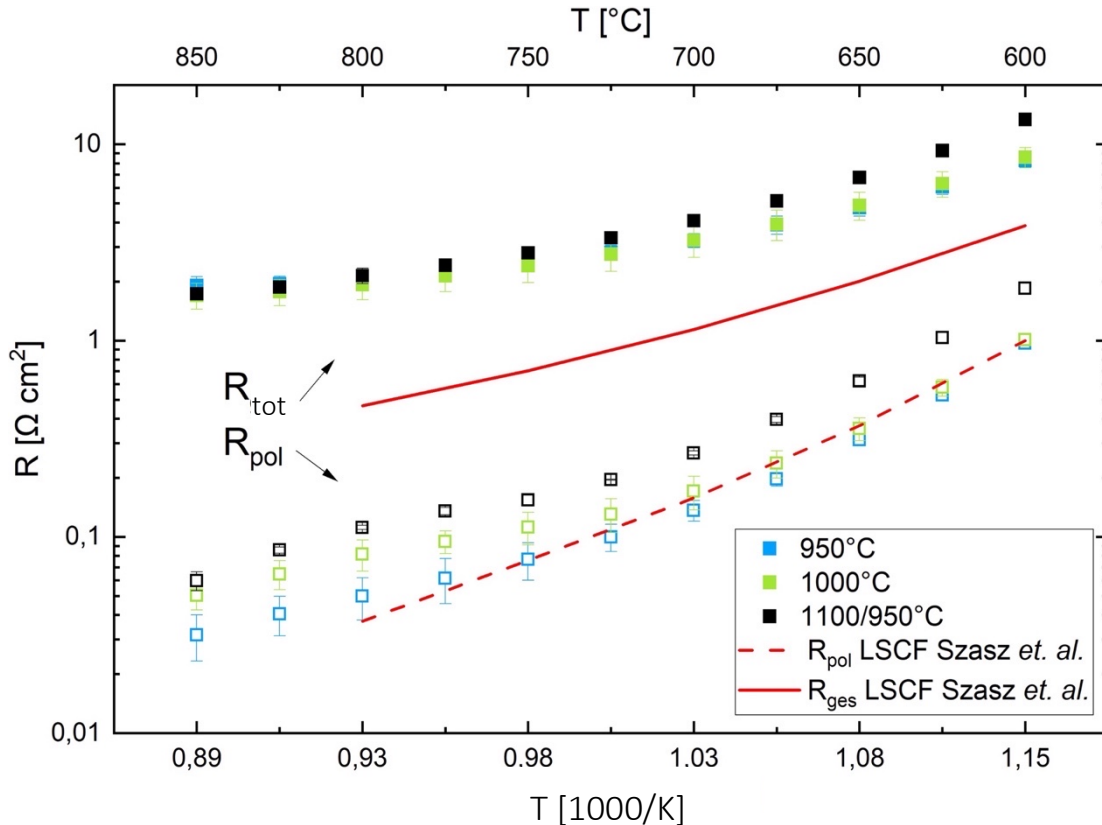


Figure 63: ASR of symmetrical cells with LCSF622 cathodes.

Since the obtained results for cathodes sintered at 950°C were exceptionally good, and in order to even further improve the ASR, the same sintering conditions were tested using a CeSZ electrolyte (cells #49-50), whereby the diffusion barrier remained the same. The measurement results are shown in Figure 64, in comparison with the cells fabricated with 8YSZ electrolyte. All activation energies are shown in Table 18.

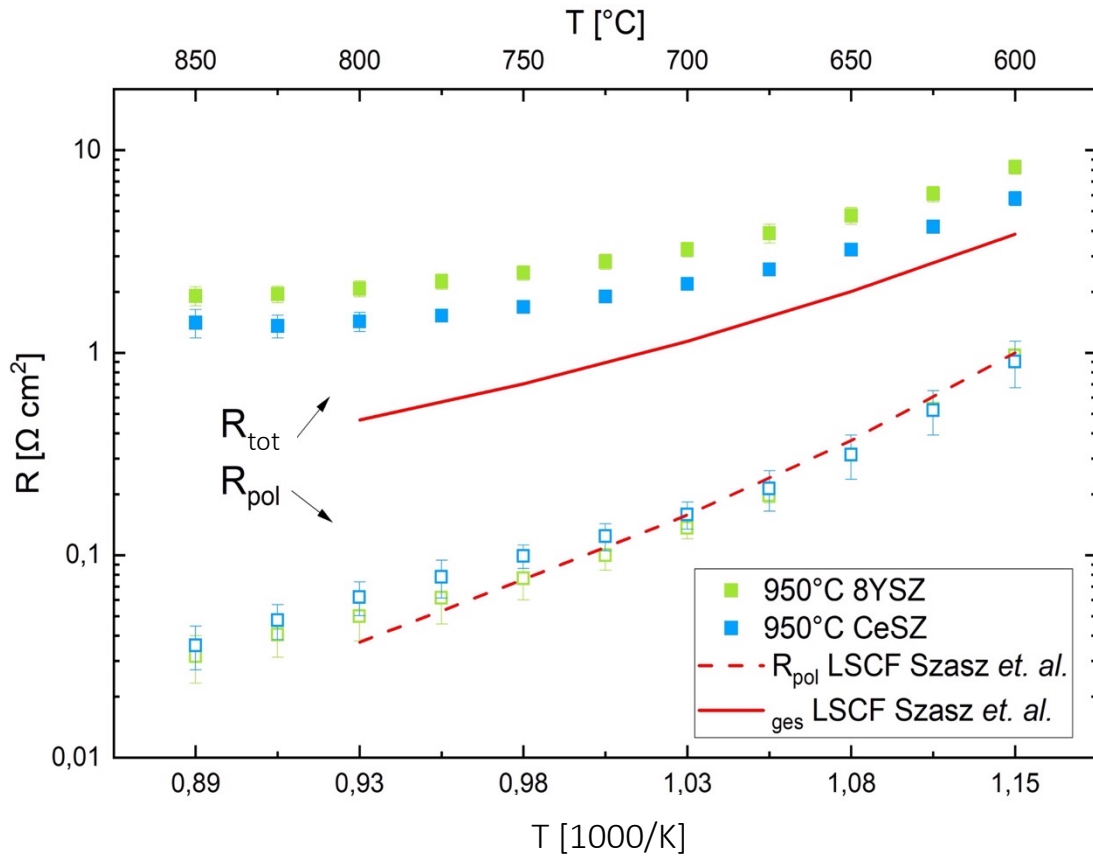


Figure 64: ASR of cells with LSCF622 cathodes using different electrolytes.

Table 18: Activation energies for cells #39-44 & #47-50

Cell number	T [°C]	E _a of ASR _Ω (R _{tot}) [eV]				E _a of ASR _{cat} (R _{pol}) [eV]			
		> 700°C		< 700°C		> 700°C		< 700°C	
		MV	SD	MV	SD	MV	SD	MV	SD
39-41	950	0.33	0.02	0.69	0.01	0.93	0.08	1.44	0.07
42-44	1000	0.40	0.02	0.72	0.05	0.76	0.02	1.31	0.08
47-48	1100/ 950	0.54	0.02	0.87	0.05	0.94	0.06	1.41	0.02
49-50	950	0.28	0.07	0.71	0.05	0.94	0.04	1.27	0.06

SEM images of LCSF622 cathodes reveal a porosity of about 53%, which is (similar to those found for LCF82) above the values commonly found in literature for LSCF6428 cathodes [45]. The surface of the cathodes appeared far more brittle than that of LCFC8282. In addition, sintering cracks occurred in large numbers, as it shown in Figure 34 as well as in Figure 65. In Figure 67, the cathode-electrolyte interface is displayed, whereby layer adhesion is clearly given as well as an expected percolation. Therefore, the relatively high ASR_{Ω} values may be related to insufficiently optimized process parameters. Since similar sinter cracks also occur in state-of-the-art materials, and because the symmetrical cell performance in terms of ASR_{cat} is in the range of LSCF6428, this phenomenon is not further discussed.

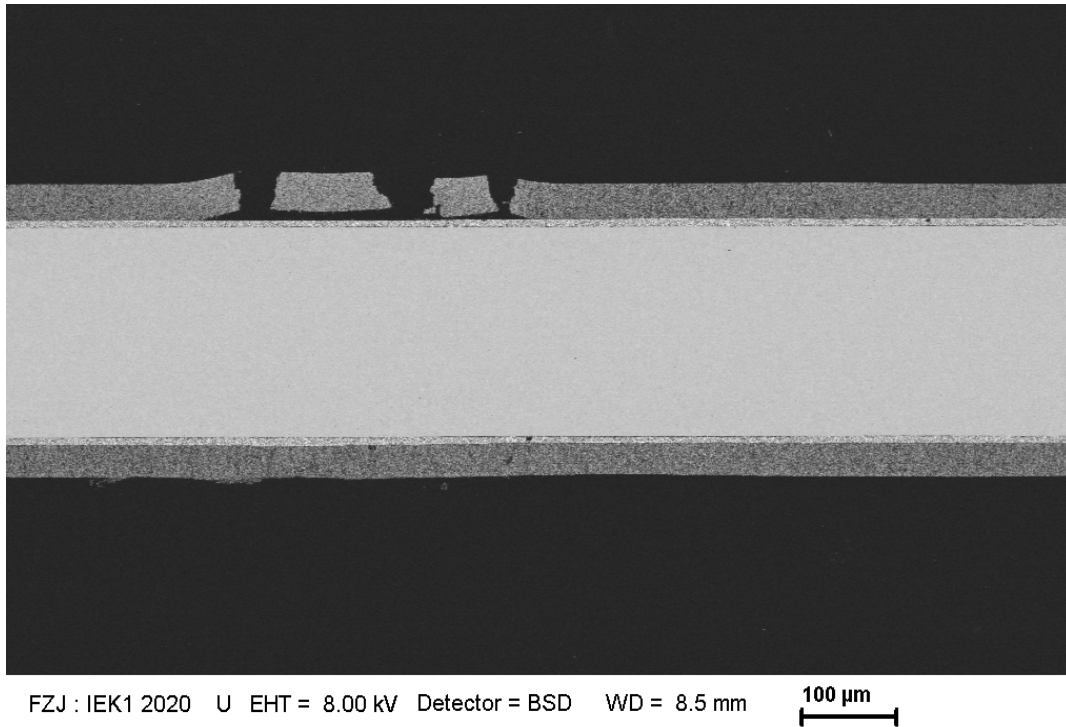


Figure 65: SEM cross-section of cell #42.

In terms of ohmic resistance, changing the electrolyte helped to further improve symmetric cell performance. When considering activation energies, however, results remain relatively unchanged between the two electrolytes. When comparing LCSF622 with 8YSZ substrate to its LCF82 and LCFC8282 counterparts, activation energies for $T > 700^{\circ}\text{C}$ show a decrease of around 100% respectively 60%, whereas in the range $T < 700^{\circ}\text{C}$, results are comparable.

In comparison with the other two materials, LCSF622 performed best in $50 \times 50 \text{ mm}^2$ cell tests. All data obtained can be found in the appendix, whereby cells 15775-5 (9M0995) and 15775-6 (9M0997) were measured. The ASR measured at a current density of 0.5 A/cm^2 at 700°C and 800°C is shown in Figure 66. At 800°C , cell 15775-5 showed an OCV of 1.002 V and 15775-6 of 0.978 V. A post-mortem analysis was conducted, whereby the SEM images revealed no secondary phases at the cathode-electrolyte interface. Sinter cracks were also found in LCSF622, whereby these did not appear to be widely branched. Regarding LCSF622 in Figure 34, it can be seen that the surface is most riddled with cracks. In addition, the cathode seemed brittle while handling it. Selected SEM images are shown in Figure 68 to Figure 71. Therefore, again a poor adhesion in combination with discrepancies in thermal expansion properties of the cathode and the electrolyte can be assumed as a possible cause for not obtaining the expected cell performance. Nevertheless, in average, LCSF622 performed better than LCFC8282 and LCF82.

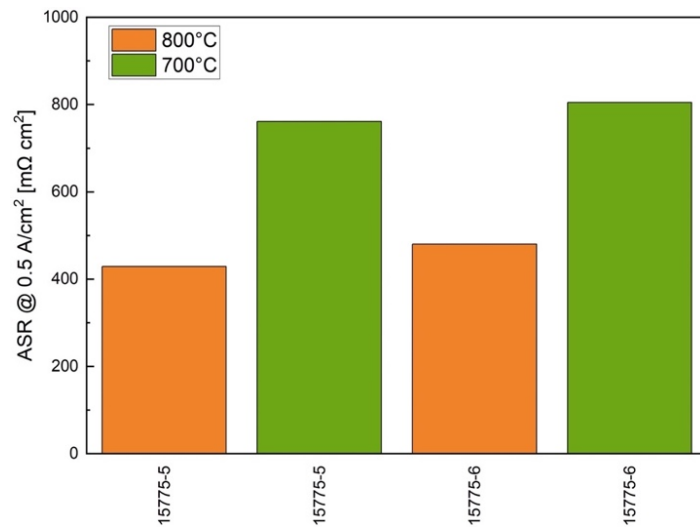


Figure 66: ASR_{tot} of cells with LCSF622 cathodes at 0.5 A/cm^2 .

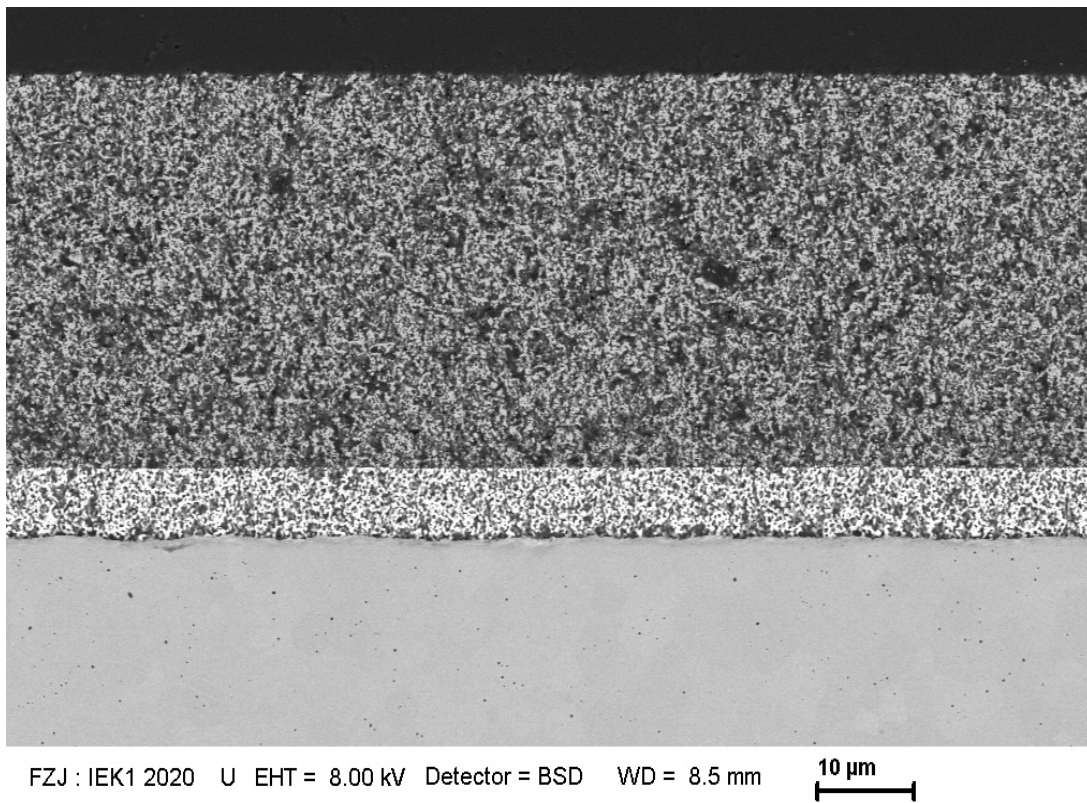


Figure 67: SEM cross-section of electrolyte interface from cell #42.

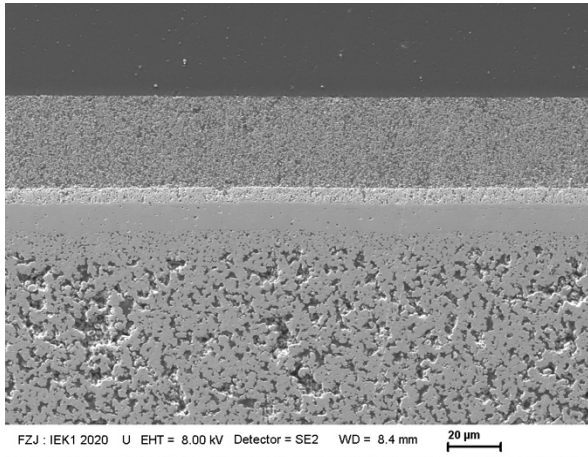


Figure 68: SEM cross-section of LCSF622-electrolyte interface.

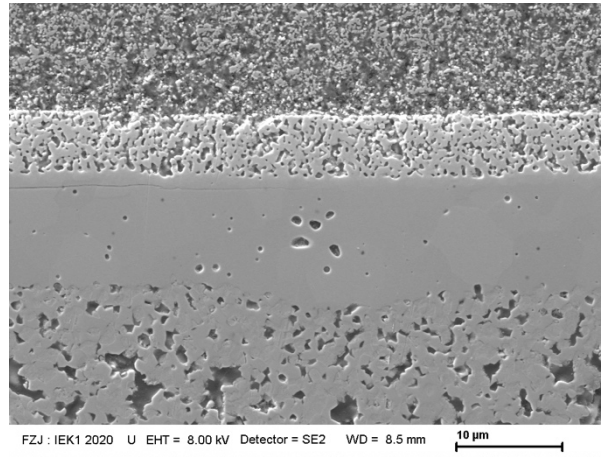


Figure 69: SEM cross-section of LCSF622-electrolyte interface.

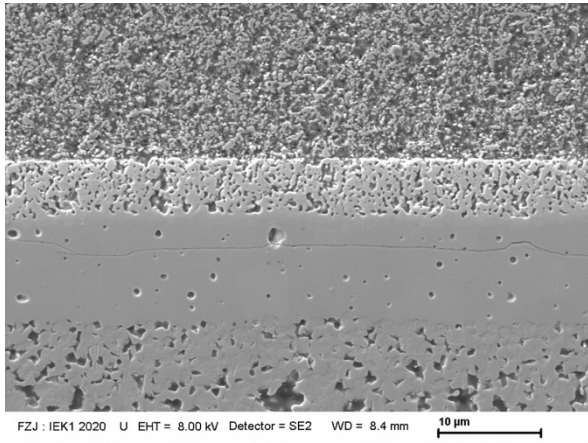


Figure 70: SEM cross-section of LCSF622-electrolyte interface.

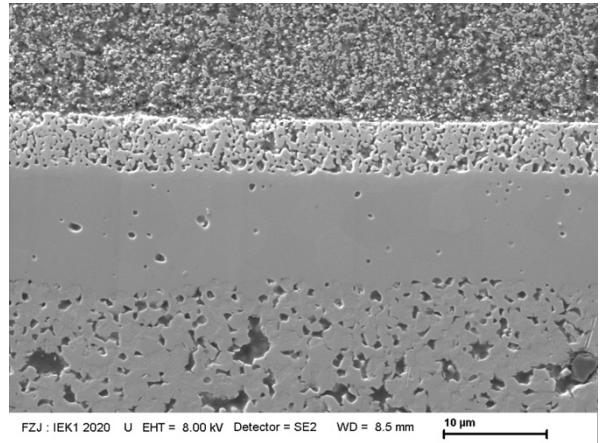


Figure 71: SEM cross-section of LCSF622-electrolyte interface.

5.6.4 Overview of cell performance

In summary, the best results from the EIS measurements as well as the activation energies from those best performing cells are shown in Figure 72 and Table 19. This serves as a concluding and comparative presentation of the results that could be achieved with the different materials.

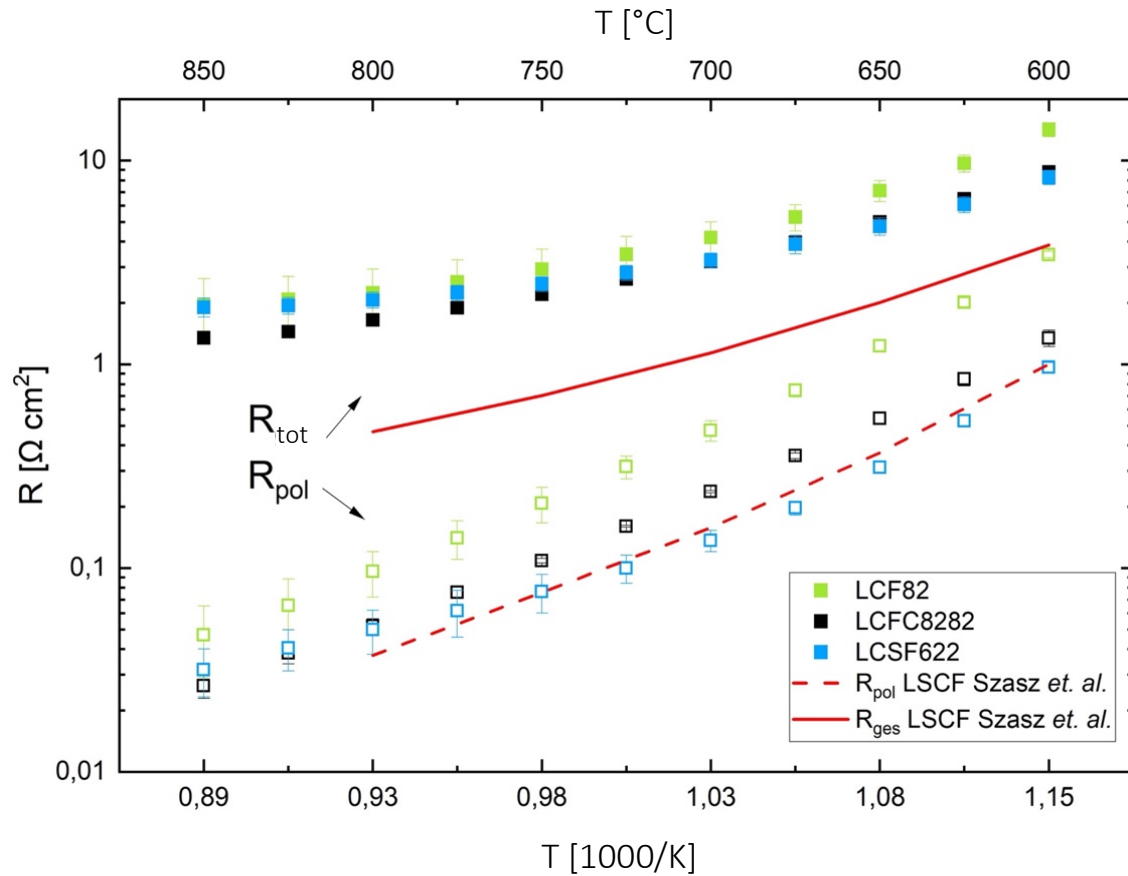


Figure 72: ASR of best performing symmetrical cells.

Table 19: Activation energies of best performing symmetrical cells

Cell number	T [°C]	Material	E _a of ASR _Ω (R _{tot}) [eV]				E _a of ASR _{cat} (R _{pol}) [eV]			
			> 700°C		< 700°C		> 700°C		< 700°C	
			MV	SD	MV	SD	MV	SD	MV	SD
17-18	950	LCF82	0.49	0.07	0.90	0.06	1.47	0.12	1.46	0.04
25-26	950	LCFC8282	0.54	0.02	0.74	0.03	1.38	0.07	1.27	0.04
49-50	950	LCSF622	0.28	0.07	0.71	0.05	0.94	0.04	1.27	0.06

6. Summary and Conclusion

In the present work, novel perovskite-based cathodes for solid oxide fuel cells are examined. The base material is LCF82, which is relatively well known and has been previously characterized [12]. In terms of the oxygen surface exchange coefficients, LCF82 can be compared to LSCF6428. Also presented in this work are two novel compounds derived from the base material, LCFC8282 and LCSF622. In the latter, the aim is to introduce more oxygen vacancies by substituting with higher concentrations of divalent ions (Sr and Ca) on trivalent lattice positions, and thus improve the oxygen surface exchange coefficients and the ionic conductivity. In case of LCFC8282, iron ions were substituted with cobalt. The underlying concept is on the one hand to improve electronic conductivity, and on the other hand, to improve the processing parameters since cobalt is known to be a very sinter-active metal [13].

After determining the optimum particle size distribution, screen-printing pastes were fabricated and sintering studies were carried out. By using EIS, sintering conditions were optimized, and symmetric button cells were prepared in order to determine microstructure-property relationships. Regarding fundamental material properties, LCFC8282 and LCSF622 seemed especially promising. However, test results of 50x50 mm² cells showed not the expected performance (refer to results given in comparison with state-of-the-art cells in the report in the appendix). While delamination and brittle surfaces, especially in LCSF622, were observed, this is usually not a direct reason for poor performance (considering for example similar LSM cathodes). In addition, no secondary phases were found at the cathode-electrolyte interface, which might otherwise have been responsible for below-average performance. Considering all these results, a likely remaining cause is poor adhesion of the cathodes to the electrolytes, which inhibits oxygen ion transport and therefore limits the overall performance.

7. Outlook

In order to improve performance of the novel materials on the cell level, further optimization of the cathode-electrolyte interface and the sintering conditions will be required. Therefore, further tests with adjusted sintering conditions and adapted rheology properties of the screen-printing pastes, in combination with state-of-the-art tape cast substrates might be able to further improve the performance.

8. Literature

- [1] INTERNATIONAL ENERGY AGENCY, "Key World Energy Statistics" IEA Publications, France, 2019.
- [2] F. Ekaradt, J. Wieding und A. Zorn, „Paris-Abkommen, Menschenrechte und Klimaklagen“ Forschungsstelle Nachhaltigkeit und Klimapolitik, Leipzig/Berlin, 2018.
- [3] Renewable Energy Certificate System, „RECS International“ 2020. [Online]. Available: <https://www.recs.org/glossary/european-20-20-20-targets>. [Zugriff am 21 March 2020].
- [4] Umweltbundesamt Deutschland, 25 July 2013. [Online]. Available: <https://www.umweltbundesamt.de/themen/klima-energie/internationale-eu-klimapolitik/kyoto-protokoll#entstehungsgeschichte-und-erste-verpflichtungsperiode>. [Zugriff am 21 March 2020].
- [5] Boston Consulting Group, „The Real Promise of Hydrogen“ 2019.
- [6] Forschungszentrum Jülich GmbH, „MENÜ+ Research + Institutes + Careers + Media + About us + High-Temperature Fuel Cell Achieves Lifetime of More Than 11 Years,“ 7 February 2019. [Online]. Available: <https://www.fz-juelich.de/SharedDocs/Pressemitteilungen/UK/EN/2019/2019-02-07-sofc-en.html?nn=2409938>. [Zugriff am 21 March 2020].
- [7] C. Berger, E. Bucher, C. Gspan, A. Menzel and W. Sitte, "Impact of SO₂ on the Oxygen Exchange Kinetics of the Promising SOFC/SOEC Air Electrode Material La_{0.8}Ca_{0.2}FeO_{3-δ}" *Journal of The Electrochemical Society*, no. 164, pp. F3008-F3018, 2017.
- [8] G. McLean, T. Niet, S. Prince-Richard and N. Djilali, "An assessment of alkaline fuel cell technology" *International Journal of Hydrogen Energy*, no. 27, pp. 507-526, 2002.
- [9] Z. Shao und M. Tade, *Intermediate-Temperature Solid Oxide Fuel Cells*, Berlin: Springer-Verlag Berlin Heidelberg, 2016.
- [10] S. Jiang, „Development of lanthanum strontium manganite perovskite cathode materials of solid oxide fuel cells: a review“ *Journal of Material Science*, Nr. 43, pp. 6799-6833, 2008.
- [11] B. Steele, „Survey of materials selection for ceramic fuel cells II. Cathodes and anodes“ *Solid State Ionics*, Nr. 86-88, pp. 1223-1234, 1996.
- [12] C. Berger, E. Bucher, A. Windischbacher, A. Boese und W. Sitte, „Strontium-free rare earth perovskite ferrites with fast oxygen exchange kinetics: Experiment and theory“ *Journal of Solid State Chemistry*, Nr. 259, pp. 57-66, 2018.
- [13] C. Grgicak, R. Green und J. Giorgi, „Control of microstructure, sinterability and performance in Co-precipitated NiYSZ, CuYSZ and CoYSZ SOFC anodes“ *Journal of Materials Chemistry*, Nr. 16, pp. 885-897, 2006.

- [14] X.-D. Zhou und S. Singhal, FUEL CELLS – SOLID OXIDE FUEL CELLS, Pacific Northwest National Laboratory, Richland, WA, USA: Elsevier B.V., 2009.
- [15] J. Larminie und A. Dicks, Fuel Cell Systems Explained, Second Edition, The Atrium, Southern Gate, Chichester, West Sussex PO19 8SQ, England: John Wiley & Sons Ltd, 2003.
- [16] J. Fleig, „Solid Oxide Fuel Cell Cathodes: Polarization Mechanisms and Modeling of the Electrochemical Performance“ *Annu. Rev. Mater. Res.*, Nr. 33, p. 361, 2003.
- [17] R. J. D. Tilley, Perovskites, Structure–Property Relationships, 2016: John Wiley & Sons Ltd, The atrium, Southern Gate, Chichester, West Sussex, PO19 8SQ, United Kingdom.
- [18] A. Huízar-Félix, T. Hernández, S. de la Parra, J. Ibarra and B. Kharisov, "Sol–gel based Pechini method synthesis and characterization of $\text{Sm}_{1-x}\text{Ca}_x\text{FeO}_3$ perovskite $0.1 \leq x \leq 0.5$ " *Powder Technology*, vol. 229, pp. 290-293, 2012.
- [19] „Chemgapedia,“ [Online]. Available: http://www.chemgapedia.de/vsengine/glossary/de/sol_00045gel_00045prozess.glos.html#. [Zugriff am 4 Juni 2018].
- [20] Verband, der, keramischen, Industrie und e.V., Brevier Technische Keramik, Fahner Verlag: Lauf, 2003.
- [21] C. Burkmeister und A. Kwade, „Process engineering with planetary ball mills“ *Chem. Soc. Rev.*, 2013.
- [22] K. Birnbaum, R. Steinberger-Wilkens und P. Zapp, „Solid Oxide Fuel Cells, Sustainability Aspects, Chapter 21“ in *Fuel Cells*, New York, Springer-Verlag, 2013.
- [23] D. Grigar, „Mesh information for the Screen Printer“ Vastex International Inc., [Online]. Available: <http://www.vastex.com/Articles/Mesh-Information-for-the-Screen-Printer.php>. [Zugriff am 22 March 2020].
- [24] K. H. Screens, KOEENEN GmbH, 08 2019. [Online]. Available: https://www.koenen.de/fileadmin/user_upload/pdfs/en/Datenblatt_Polyestergewebe_ENG.pdf. [Zugriff am 24 March 2020].
- [25] M. Somalu, A. Muchtar, W. Daud und N. Brandon, „Screen-printing inks for the fabrication of solid oxide fuel cell films: A review“ *Renewable and Sustainable Energy Reviews*, 2016.
- [26] E. A. T. GmbH. [Online]. Available: <https://www.exakt.de/en/products/three-roll-mills/technology.html>. [Zugriff am 16 January 2021].
- [27] H. Scheer, Siebdruck-Handbuch, 1 Hrsg., Dräger Druck, 1999.
- [28] Anton Paar GmbH, „Basics of rheology“ Anton Paar GmbH, [Online]. Available: <https://wiki.anton-paar.com/be-en/basics-of-rheology/>. [Zugriff am 21 March 2020].

- [29] L. van der Pauw, „A method of measuring specific resistivity and Hall effect of discs of arbitrary shape“ *Philips Research Reports*, Bd. 13, Nr. 1, pp. 1-9, 1958.
- [30] H. Krischner und B. Koppelhuber-Bitschnau, Röntgenstrukturanalyse und Rietveldmethode, Wiesbaden: Springer Fachmedien, 1994.
- [31] P. Uden, „Element-specific chromatographic detection by atomic absorption, plasma atomic emission and plasma mass spectrometry“ *Journal of Chromatography*, Nr. 703, pp. 393-416, 1995.
- [32] G. Gottstein, Materialwissenschaft und Werkstofftechnik, Physikalische Grundlagen, Springer-Verlag Berlin Heidelberg, 2014.
- [33] G. Höhne, W. Hemminger und H.-J. Flammersheim, Differential Scanning Calorimetry, Berlin Heidelberg: Springer-Verlag, 2003.
- [34] L. Corporation, LECO Corporation, 2008. [Online]. Available: <http://www.usbioecuator.com/descargas/leco-inorganica/TCH600-ht.pdf>. [Zugriff am 26 March 2020].
- [35] H. Martin, „LEITFÄHIGE KERAMIK ALS ELEKTROWERKSTOFF FÜR DEN HOCHTEMPERATURBEREICH“ Fraunhofer IKTS, 2014/15. [Online]. Available: https://www.ikts.fraunhofer.de/content/dam/ikts/downloads/jahresberichte/jb2014/14_Leitfähige_Keramik_als_Elektrowerkstoff_für_den_Hochtemperaturbereich.pdf. [Zugriff am 26 March 2020].
- [36] R. de Souza, *Dissertation, Department of Materials*, Imperial College of Science, Technology and Medicine, 1996.
- [37] S. Adler, J. Lane und B. Steele, „Electrode Kinetics of Porous Mixed-Conducting Oxygen Electrodes“ *Journal of The Electrochemical Society*, Nr. 143, p. 3554–3564, 1996.
- [38] C. Endler-Schuck, J. Joos, C. Niedrig, A. Weber and E. Ivers-Tiffée, "The chemical oxygen surface exchange and bulk diffusion coefficient determined by impedance spectroscopy of porous $\text{La}_{0.58}\text{Sr}_{0.4}\text{Co}_{0.2}\text{Fe}_{0.8}\text{O}_{3-\delta}$ (LSCF) cathodes" *Solid State Ionics*, no. 269, pp. 67-79, 2015.
- [39] W. Preis, E. Bucher und W. Sitte, „Oxygen exchange measurements on perovskites as cathode materials for solid oxide fuel cells“ *Journal of Power Sources*, Nr. 106, pp. 116-121, 2002.
- [40] L. van der Haar, M. den Otter, M. Morskate, H. Bouwmeester and H. Verweij, "Chemical Diffusion and Oxygen Surface Transfer of $\text{La}_{1-x}\text{Sr}_x\text{CoO}_{3-\delta}$ Studied with Electrical Conductivity Relaxation" *Journal of The Electrochemical Society*, no. 149, 2002.
- [41] W. Preis, E. Bucher and W. Sitte, "Oxygen exchange kinetics of $\text{La}_{0.4}\text{Sr}_{0.6}\text{FeO}_{3-\delta}$ by simultaneous application of conductivity relaxation and carrier gas coulometry" *Solid State Ionics*, no. 175, pp. 393-397, 2004.

- [42] C. Berger, „Development of new materials for solid oxide fuel cell cathodes with superior performance and improved long-term stability“ PhD thesis, 2019.
- [43] G. Instruments, Gamry Instruments, [Online]. Available: <https://www.gamry.com/application-notes/EIS/basics-of-electrochemical-impedance-spectroscopy/>. [Zugriff am 29 March 2020].
- [44] M. Orazem und B. Tribollet, *Electrochemical Impedance Spectroscopy*, New Jersey: John Wiley & Sons, Inc., 2008.
- [45] J. Szász, F. Wankmüller, V. Wilde, H. Störmer, D. Gerthsen, N. H. Menzler and E. Ivers-Tiffée, "Nature and Functionality of $\text{La}_{0.58}\text{Sr}_{0.4}\text{Co}_{0.2}\text{Fe}_{0.8}\text{O}_{3-\delta}$ / $\text{Gd}_{0.2}\text{Ce}_{0.8}\text{O}_{2-\delta}$ / $\text{Y}_{0.16}\text{Zr}_{0.84}\text{O}_{2-\delta}$ Interfaces in SOFCs" *Journal of The Electrochemical Society*, vol. 165, no. 10, pp. F898-F906, 2018.
- [46] The International Union of Crystallography, „International Tables for Crystallography“ in *Volume A: Space-Group Symmetry*, P.O. Box 17, 3300 AA Dordrecht, The Netherlands, Springer, 2005, p. 15.
- [47] The International Union of Crystallography, „International Tables for Crystallography“ in *Volume A: Space-Group Symmetry*, P.O. Box 17, 3300 AA Dordrecht, The Netherlands, Springer, 2005, p. 19.
- [48] K. Hilpert, R. W. Steinbrech, F. Boroomand, E. Wessel, F. Meschke, A. Zuev, O. Teller, H. Nickel and L. Singheiser, "Defect formation and mechanical stability of perovskites based on LaCrO_3 for solid oxide fuel cells (SOFC)" *Journal of the European Ceramic Society*, vol. 23, no. 16, pp. 3009-3020, 2003.
- [49] P. Ried, P. Hotlappels, A. Wichser, A. Ulrich and T. Graule, "Synthesis and Characterization of $\text{La}_{0.6}\text{Sr}_{0.4}\text{Co}_{0.2}\text{Fe}_{0.8}\text{O}_{3-\delta}$ and $\text{Ba}_{0.5}\text{Sr}_{0.5}\text{Co}_{0.8}\text{Fe}_{0.2}\text{O}_{3-\delta}$ " vol. 155, no. 10, pp. B1029-B1035, 2008.
- [50] N. Q. Minh und T. Takahashi, *Science and Technology of Ceramic Fuel Cells*, pp. 69-116, 1995.
- [51] S. J. Hong und A. V. Virkar, *Correlation between thermal expansion and oxide ion transport in mixed conducting perovskite-type oxides for SOFC cathodes*, Bd. 78, p. 433, 1995.
- [52] P. Price, E. Rabenberg, D. Thomsen, S. Mixture und D. Butt, „Phase Transformations in Calcium-Substituted Lanthanum Ferrite“ *Journal of the American Ceramic Society*, Bd. 97, pp. 2241-2248, 2014.
- [53] A. Benali, A. Souissi, M. Bejar, E. Dhahri, M. Graça und M. Valente, „Dielectric properties and alternating current conductivity of sol-gel made $\text{La}_{0.8}\text{Ca}_{0.2}\text{FeO}_3$ compound“ *Chem. Phys. Lett.*, Nr. 637, pp. 7-12, 2015.

- [54] E. Bucher and W. Sitte, "Defect chemical analysis of the electronic conductivity of strontium-substituted lanthanum ferrite" *Solide State Ionics*, no. 173, pp. 23-28, 2004.
- [55] Y. Yamaguchi, I. Kagomiya, S. Minami, H. Shimada, H. Sumi, Y. Ogura und Y. Mizutani, „La_{0.65}Ca_{0.35}FeO_{3-δ} as a novel Sr- and Co-free cathode material for solid oxide fuel cells,“ *Journal of Power Sources*, Nr. 448, 2020.
- [56] R. Merkle, D. Poetzsch und J. Maier, „Oxygen Reduction Reaction at Cathodes on Proton Conducting Oxide Electrolytes: Contribution from Three Phase Boundary Compared to Bulk Path“ *ECS Transactions*, Bd. 66, Nr. 2, pp. 95-102, 2015.
- [57] K. Momma und F. Izumi, „VESTA 3 for three-dimensional visualization of crystal, volumetric and morphology data“ *J. Appl. Crystallogr.*, Nr. 44, pp. 1272-1276, 2011.
- [58] H. Zhu, R. Kee, M. Pillai und S. Barnett, „Modeling electrochemical partial oxidation of methane for cogeneration of electricity and syngas in solid-oxide fuel cells“ *Journal of Power Sources*, Nr. 183, pp. 143-150, 2008.
- [59] A. W. Coats und J. Redfern, „Thermogravimetric analysis. A review“ *Analyst*, Nr. 1053, 1963.
- [60] H. Ullmann, N. Trofimenko, F. Tietz, D. Stöver und A. Ahmad-Khanlou, „Correlation between thermal expansion and oxide ion transport in mixed conducting perovskite-type oxides for SOFC cathodes“ *Solid State Ionics*, Bd. 138, Nr. 1-2, pp. 79-90, 2000.
- [61] R. E. Hummel, *Electronic Properties of Materials*, New York: Springer, 2001.

9. Appendix

9.1. Synthesis and Powder

Table 20: Determination of the stoichiometric composition and molar mass of the compounds

Elements	molar mass [g/mol]	LCF82 LCFC8282 LCSF622			LCF82 LCFC8282 LCSF622		
		Stoichiometry [-]			Stoichiometry · molar mass [g/mol]		
La	138.906	0.8	0.8	0.6	111.124	111.124	83.343
Ca	40.078	0.2	0.2	0.2	8.016	8.016	8.016
Sr	87.620			0.2			17.524
Fe	55.847	1	0.8	1	55.847	44.678	55.847
Co	58.933		0.2			11.787	
O	15.999	3	3	3	47.998	47.998	47.998
					222.985	223.602	212.728

Table 21: Calculation of the theoretically required- and the actual weights during synthesis

		LCF82	LCF82_1	LCF82_2	LCFC8282	LCFC8282_1	LCFC8282_2	LCSF622	LCSF622_1	LCSF622_2
Reagent	product [g/mol]	30/0.1345			30/0.1342			30/0.1410		
chemical structure	m _{mol} [g/mol]	theo. [g]	real [g]	real [g]	theo. [g]	real [g]	real [g]	theo. [g]	real [g]	real [g]
La(NO ₃) ₃ x 6 H ₂ O	433.01	46.6051	46.6066	46.6075	46.4764	46.4770	46.4768	36.6392	36.6398	36.6397
Ca(NO ₃) ₂ x 4 H ₂ O	236.15	6.3542	6.3543	6.3551	6.4660	6.4669	6.4668	6.7965	6.7975	6.7973
Sr(NO ₃) ₂	211.63							5.9690	5.9690	5.9695
Fe(NO ₃) ₃ x 9 H ₂ O	404.00	54.3534	54.3537	54.3540	43.3627	43.3637	43.3630	56.9741	56.9741	56.9742
Co(NO ₃) ₃ x 6 H ₂ O	291.03				7.9688	7.9695	7.9696			
CA		46.0000	46.0004	46.0008	39.2102	39.2110	39.2105	41.2146	41.2154	41.2151
EDTA		35.0000	35.0001	35.0002	51.5522	51.5528	51.5530	54.1875	54.1874	54.1870

9.2. Screen printing

Table 22: Parameters for ESC BCs

Parameter	Value	Unit
Squeegee speed forwards	80	mm/s
Squeegee speed back	80	mm/s
Squeegee way start	80	mm
Squeegee way stop	-80	mm
Squeegee pressure	1.5/74	bar/N
Substrate thickness (LP)	0.2	mm
Screen gap	1.5	mm
Separation distance	3	mm
Separation speed	1	mm
Drying conditions	1/60	h/°C

Table 23: Parameters for 50x50 mm² cells

Parameter	Value	Unit
Squeegee speed forwards	110	mm/s
Squeegee speed back	110	mm/s
Squeegee way start	120	mm
Squeegee way stop	-120	mm
Squeegee pressure	1/49	bar/N
Substrate thickness (LP)	1.5	mm
Screen gap	1.3	mm
Separation distance	3	mm
Separation speed	1	mm
Drying conditions	3/60	h/°C

Table 24: Abbreviations for BC printing

Abb.	Explanation
d_0	Thickness of the substrate including GDC layer
d_1	Total thickness of dried cell
d_2	Dry cathode thickness ($d_1 - d_0$ all divided by 2)
NSD	Wet film layer, determined by sieve
DS	Drying shrinkage ($1 - (d_2/NSD)$)
T/t	Sinter temperature and sinter time
d_3	Total thickness of sintered cell
d_c	Sintered cathode thickness ($d_3 - d_0$ all divided by 2)

Table 25: Used meshes for screen-printing

No.	Properties
1	Ø 10 mm round, 18-180, 150 µm NSD
2	Ø 8 mm round taped, 36-90, VA 120-0,065 x 22,5°, 64 µm NSD
3	LSCF_CL 50x50 146µm NSD

Table 26: LCF82 printed BCs

No.	Paste	Screen	d ₀ [μm]	d ₁ [μm]	d ₂ [μm]	DS	T/t [°C/h]	d ₃ [μm]	d _c [μm]
1.1			216	314	49	67%		313	49
2.1	LCF82_V1_3_2	1	225	315	45	70%	1040/2	310	43
3.1			221	314	47	69%		313	46
4.1			220	308	44	71%		291	36
1.2			313						
2.2	LSM_cc	2	310	Not determined due to very thin LSM layer			950/2	-	
3.2			313						
4.2			291						
5			223	315	46	69%		314	46
6	LCF82_V1_3_2	1	220	307	44	71%	1060/2	315	48
7			221	315	47	69%		311	45
8			220	309	45	70%		312	46
9			225	308	42	72%		313	44
10	LCF82_V1_3_2	1	226	314	44	71%	1080/2	312	43
11			220	310	45	70%		308	44
12			226	310	42	72%		313	44
13			224	314	45	70%		296	36
14	LCF82_V1_3_2	1	220	316	48	68%	1100/2	309	45
15			223	316	47	69%		308	43
16			221	308	44	71%		295	37
17	LCF82_V1_3_2	1	218				950/2	310	46
18			218					312	47
19	LCF82_V1_3_2	1	221				950/2	317	48
	LSM_cathode	2	317					340	12
20	LCF82_V1_3_2	1	224				950/2	314	45

	LSM_cathode	2	314			342	14
21			217			284	34
22	LCF_GDC_50_50	1	219	-	950/2	289	35
23			217			286	35
24	LCF_GDC_70_30	1	217	-	950/2	282	33
33			224			224	
34	LCF82_V3	1	224	-	950/2	224	
35			230			230	
36			226			226	
37	LCF82_V3	1	227	-	1000/2	227	
38			232			232	
45			250			250	
46	LCF82_V3	1	233	-	1100-950 /0-1,5	233	

Table 27: LCFC8282 printed BCs

No.	Paste	Screen	d ₀ [μm]	T/t [°C/h]
25	LCFC8282_V1	1	221	950/2
26			217	
27			220	
28	LCFC8282_V1	1	218	900/2
29			218	
30			220	
31	LCFC8282_V1	1	220	1000/2
32			217	

Table 28: LCSF622 printed BCs

No.	Paste	Screen	d ₀ [μm]	T/t [°C/h]
39			225	
40	LCSF622_V1	1	239	950/2
41			246	
42			233	
43	LCSF622_V1	1	233	1000/2
44			234	
47	LCSF622_V1	1	228	1100-950 /0-1,5
48			248	
49	LCSF622_V1	1	-	950/2
50				

Table 29: 50x50 mm² cells

No.	Paste	Screen	d ₀ [μm]	T/t [°C/h]	d ₃ [μm]	d _c [μm]
15770_6					1627	105
15770_7	LCF82_V3	3	1522	950/2	1647	125
15770_8					1607	85
15775_4					1591	69
15775_7	LCFC8282_V1	3	1522	950/2	1553	31
15775_8					1609	87
15775_3					1639	117
15775_5	LCSF622_V1	3	1522	950/2	1575	53
15775_6					1583	61

1 ANGABEN ZU DEN ZELLEN UND ZU DEN MESSUNGEN

Tabelle 1 ZELLEN UND MESSUNGEN							
Serie	Zelle Nummer	Typ	Kathode/ Paste	Kathoden- dicke [μm]	Messung Nummer	Prüfstand	Datum
1	15770-6	lbx	LCF 82	105	9M0981	MP 08	19.08.2020
2	15770-7	lbx	LCF 82	125	9M0985	MP 08	27.08.2020
3	15775-4	lbx	LCFC 8282	69	9M0992	MP 08	18.09.2020
4	15775-7	lbx	LCFC 8282	73	9M0993	MP 08	28.09.2020
5	15775-5	lbx	LCSF 622	53	9M0995	MP 08	06.10.2020
6	15775-6	lbx	LCSF 622	61	9M0997	MP 08	16.10.2020
7	15775-8	lbx	LCFC 8282	87	9M1001	MP 08	02.11.2020

Tabelle 2 Kennlinien-Messungen während Messung Nummer 9M0981 für Zelle 15770-6

	Start	Ende	Temperatur	H ₂	N ₂	H ₂ O	LUFT
			[°C]	NI/h	NI/h	NI/h	NI/h
KL 1	21.08.2020 11:11	21.08.2020 11:28	800	60	0	15	120
KL 2	21.08.2020 17:40	21.08.2020 17:52	750	60	0	15	120
KL 3	21.08.2020 23:35	21.08.2020 23:44	700	60	0	15	120
KL 4	22.08.2020 04:01	22.08.2020 04:06	647	60	0	15	120
KL 5	24.08.2020 11:16	24.08.2020 11:20	602	60	0	15	120
KL 6	24.08.2020 17:54	24.08.2020 18:19	802	60	0	60	120
KL 7	24.08.2020 23:00	24.08.2020 23:18	747	60	0	60	120
KL 8	25.08.2020 04:59	25.08.2020 05:12	700	60	0	60	120
KL 9	25.08.2020 10:29	25.08.2020 10:37	651	60	0	60	120
KL 10	25.08.2020 17:25	25.08.2020 17:40	801	15	0	60	120
KL 11	25.08.2020 20:43	25.08.2020 20:53	748	15	0	60	120
KL 12	26.08.2020 01:22	26.08.2020 01:29	700	15	0	60	120
KL 13	26.08.2020 05:59	26.08.2020 06:03	650	15	0	60	120

Tabelle 3 Kennlinien-Messungen während Messung Nummer 9M0985 für Zelle 15770-7

	Start	Ende	Temperatur	H ₂	N ₂	H ₂ O	LUFT
			[°C]	NI/h	NI/h	NI/h	NI/h
KL 1	08.09.2020 08:22	08.09.2020 08:30	804	61	0	15	120
KL 2	08.09.2020 14:53	08.09.2020 15:00	749	61	0	15	120
KL 3	09.09.2020 06:09	09.09.2020 06:14	699	61	0	15	120
KL 4	09.09.2020 10:44	09.09.2020 10:48	650	61	0	15	120
KL 5	10.09.2020 11:40	10.09.2020 11:43	602	61	0	15	120
KL 6	11.09.2020 07:55	11.09.2020 08:09	801	61	0	59	120
KL 7	11.09.2020 12:44	11.09.2020 12:54	747	61	0	60	120
KL 8	11.09.2020 18:15	11.09.2020 18:23	700	61	0	59	120
KL 9	11.09.2020 23:44	11.09.2020 23:48	649	61	0	59	120
KL 10	12.09.2020 05:27	12.09.2020 05:35	801	16	0	59	120
KL 11	12.09.2020 08:39	12.09.2020 08:45	747	16	0	60	120
KL 12	12.09.2020 13:14	12.09.2020 13:19	699	16	0	58	120
KL 13	12.09.2020 17:48	12.09.2020 17:51	649	16	0	60	120

Tabelle 4 Kennlinien-Messungen während Messung Nummer 9M0992 für Zelle 15775-4

	Start	Ende	Temperatur	H ₂	N ₂	H ₂ O	LUFT
			[°C]	NI/h	NI/h	NI/h	NI/h
KL 1	20.09.2020 13:01	20.09.2020 13:15	799	61	0	15	120
KL 2	20.09.2020 19:16	20.09.2020 19:26	750	61	0	15	120
KL 3	21.09.2020 11:17	21.09.2020 11:24	701	61	0	15	120
KL 4	21.09.2020 15:41	21.09.2020 15:46	646	61	0	15	120
KL 5	22.09.2020 21:01	22.09.2020 21:22	800	61	0	60	120
KL 6	22.09.2020 22:28	22.09.2020 22:48	800	61	0	60	120
KL 7	23.09.2020 03:23	23.09.2020 03:39	747	61	0	59	120
KL 8	23.09.2020 09:58	23.09.2020 10:09	699	61	0	59	120
KL 9	23.09.2020 15:50	23.09.2020 15:58	649	61	0	59	120
KL 10	23.09.2020 22:17	23.09.2020 22:28	800	16	0	60	120
KL 11	24.09.2020 01:27	24.09.2020 01:36	748	16	0	60	120
KL 12	24.09.2020 06:06	24.09.2020 06:12	699	16	0	59	120
KL 13	24.09.2020 11:02	24.09.2020 11:06	648	16	0	59	120

Tabelle 5 Kennlinien-Messungen während Messung Nummer 9M0993 für Zelle 15775-7

	Start	Ende	Temperatur	H ₂	N ₂	H ₂ O	LUFT
			[°C]	NI/h	NI/h	NI/h	NI/h
KL 1	29.09.2020 11:26	29.09.2020 11:44	799	61	0	15	120
KL 2	29.09.2020 18:04	29.09.2020 18:17	750	61	0	15	120
KL 3	29.09.2020 23:37	29.09.2020 23:46	701	61	0	15	120
KL 4	30.09.2020 04:03	30.09.2020 04:08	646	61	0	15	120
KL 5	30.09.2020 12:20	30.09.2020 12:46	803	61	0	59	120
KL 6	30.09.2020 17:07	30.09.2020 17:26	746	61	0	59	120
KL 7	01.10.2020 10:33	01.10.2020 10:45	700	60	0	59	120

Tabelle 6 Kennlinien-Messungen während Messung Nummer 9M0995 für Zelle 15775-5

	Start	Ende	Temperatur	H ₂	N ₂	H ₂ O	LUFT
			[°C]	NI/h	NI/h	NI/h	NI/h
KL 1	07.10.2020 10:51	07.10.2020 11:16	799	60	0	15	120
KL 2	07.10.2020 17:16	07.10.2020 17:36	750	61	0	15	120
KL 3	07.10.2020 23:07	07.10.2020 23:22	700	61	0	15	120
KL 4	08.10.2020 03:38	08.10.2020 03:48	646	61	0	15	120
KL 5	08.10.2020 12:10	08.10.2020 12:50	802	61	0	59	120
KL 6	09.10.2020 23:17	09.10.2020 23:32	649	61	0	59	120
KL 7	12.10.2020 13:05	12.10.2020 13:29	802	16	0	60	120
KL 8	12.10.2020 16:33	12.10.2020 16:50	748	16	0	59	120
KL 9	12.10.2020 21:00	12.10.2020 21:12	699	16	0	60	120
KL10	13.10.2020 01:24	13.10.2020 01:31	649	16	0	60	120
KL11	13.10.2020 11:14	13.10.2020 11:54	801	61	0	60	120
KL12	13.10.2020 15:48	13.10.2020 16:18	747	61	0	59	120
KL13	13.10.2020 21:21	13.10.2020 21:43	699	61	0	59	120
KL14	14.10.2020 03:02	14.10.2020 03:16	649	61	0	59	120

Tabelle 7 Kennlinien-Messungen während Messung Nummer 9M0997 für Zelle 15775-6

	Start	Ende	Temperatur	H ₂	N ₂	H ₂ O	LUFT
			[°C]	NI/h	NI/h	NI/h	NI/h
KL 1	19.10.2020 05:49	19.10.2020 06:10	798	61	0	15	120
KL 2	19.10.2020 11:51	19.10.2020 12:09	752	61	0	15	120
KL 3	19.10.2020 17:19	19.10.2020 17:32	701	61	0	15	120
KL 4	21.10.2020 12:31	21.10.2020 13:05	800	61	0	59	120
KL 5	21.10.2020 17:06	21.10.2020 17:32	747	61	0	59	120
KL 5	21.10.2020 22:36	21.10.2020 22:55	699	61	0	59	120
KL 7	22.10.2020 04:02	22.10.2020 04:14	648	61	0	59	120
KL 8	26.10.2020 18:55	26.10.2020 19:14	799	16	0	60	120
KL 9	26.10.2020 22:13	26.10.2020 22:27	748	16	0	60	120
KL 10	27.10.2020 02:42	27.10.2020 02:52	698	16	0	60	120
KL11	27.10.2020 12:08	27.10.2020 12:15	649	15	0	60	120

Tabelle 8 Kennlinien-Messungen während Messung Nummer 9M1001 für Zelle 15775-8

	Start	Ende	Temperatur	H ₂	N ₂	H ₂ O	LUFT
			[°C]	NI/h	NI/h	NI/h	NI/h
KL 1	03.11.2020 12:58	03.11.2020 13:23	799	61	0	15	120
KL 2	03.11.2020 19:23	03.11.2020 19:41	750	61	0	15	120
KL 3	04.11.2020 00:54	04.11.2020 01:06	702	61	0	15	120
KL 4	04.11.2020 05:30	04.11.2020 05:37	645	61	0	15	120
KL 5	04.11.2020 15:36	04.11.2020 16:15	802	61	0	59	120
KL 5	04.11.2020 20:32	04.11.2020 20:59	747	61	0	59	120
KL 7	05.11.2020 12:01	05.11.2020 12:18	699	61	0	59	120
KL 8	06.11.2020 09:22	06.11.2020 09:33	648	61	0	59	120
KL 9	06.11.2020 15:12	06.11.2020 15:34	801	16	0	59	120
KL 10	06.11.2020 18:38	06.11.2020 18:53	747	16	0	59	120
KL11	06.11.2020 23:03	06.11.2020 23:13	699	16	0	59	120
KL12	07.11.2020 03:23	07.11.2020 03:30	648	16	0	59	120

2 ERGEBNISSE ELEKTROCHEMISCHE ZELLCHARAKTERISIERUNG

Elektrochemische Kennwerte									
Proben- kennung	Temperatur	OCV	Strom- dichte @ 0.7 V	Strom- dichte @ 1.2 V	ASR @ 0.5A/cm ²	ASR @ -0.5A/cm ²	Spannung @ 0.5 A/cm ²	Spannung @ -0.5 A/cm ²	Grenz- strom- dichte
	[°C]	[V]	[A/cm ²]	[A/cm ²]	[mΩ·cm ²]	[mΩ·cm ²]	[V]	[V]	[A/cm ²]
9M0981	800	1,000	0,429	--	638	--	0,655	--	--
	750	1,015	0,321	--	820*	--	--	--	--
	700	1,028	0,216	--	1175*	--	--	--	--
	647	1,042	0,128	--	1788*	--	--	--	--
	602	1,029	0,073	--	2897*	--	--	--	--
	802	0,935	0,294	-0,453	754*	808*	--	--	--
	747	0,952	0,212	-0,309	1002*	1142*	--	--	--
	700	0,964	0,161	-0,201	1328*	1690*	--	--	--
	651	0,985	0,098	-0,113	1929*	2827*	--	--	--
	801	0,879	--	-0,517	--	743	--	1,287	--
	748	0,899	--	-0,368	--	1100*	--	--	--
	700	0,913	--	-0,241	--	1590*	--	--	--
650	0,935	--	-0,14	--	2565*	--	--	--	
9M0985	804	0,996	0,186	--	1450*	--	--	--	-
	749	1,008	0,143	--	1792*	--	--	--	-
	699	1,027	0,095	--	2476*	--	--	--	-
	650	1,015	0,059	--	3486*	--	--	--	-
	602	0,987	--	--	--	--	--	--	-
	801	0,924	0,146	-0,252	1402*	1527*	--	--	-
	747	0,946	0,113	-0,18	1758*	2069*	--	--	-
	700	0,95	0,075	--	2304*	--	--	--	-
	649	0,952	0,045	--	3467*	--	--	--	-
	801	0,864	--	-0,28	--	1556*	--	--	-
	747	0,882	--	-0,222	--	1869*	--	--	--
	699	0,897	--	-0,15	--	2572*	--	--	--
649	0,928	--	--	--	--	--	--	--	
9M0992	799	1,002	0,336	--	797*	--	--	--	--
	750	1,011	0,251	--	1077*	--	--	--	--
	701	1,022	0,160	--	1648*	--	--	--	--
	646	1,031	0,094	-0,086*	2554*	--	--	--	--
	800	0,931	0,246	-0,369	879*	973*	--	--	--
	800	0,932	0,246	-0,363*	892*	970*	--	--	--
	747	0,948	0,188	-0,266	1168*	1327*	--	--	--
	699	0,936	0,125	-0,203	1601*	1849*	--	--	--
	649	0,927	0,070	--	2304*	--	--	--	--
800	0,87	--	-0,42	--	1025*	--	--	--	

Elektrochemische Kennwerte									
Proben- kennung	Temperatur	OCV	Strom- dichte @ 0.7 V	Strom- dichte @ 1.2 V	ASR @ 0.5A/cm ²	ASR @ -0.5A/cm ²	Spannung @ 0.5 A/cm ²	Spannung @ -0.5 A/cm ²	Grenz- strom- dichte
	748	0,874	--	-0,351	--	1216*	--	--	--
	699	0,877	--	-0,245	--	1734*	--	--	--
	648	0,862	--	-0,155	--	2819*	--	--	--
9M0993	799	1,000	0,432	--	616	--	0,657	--	--
	750	1,014	0,315	--	855*	--	--	--	--
	701	1,023	0,207	--	1245*	--	--	--	--
	646	1,032	0,117	-0,107*	2030*	--	--	--	--
	803	0,933	0,309	-0,47	713*	767*	--	--	--
	746	0,95	0,236	-0,33	961*	1067*	--	--	--
	700	0,961	0,158	-0,211	1355*	1646*	--	--	--
9M0995	799	1,002	0,649	--	429	--	0,766	--	--
	750	1,011	0,538	--	549	--	0,721	--	--
	700	1,026	0,39	--	761	--	0,615	--	--
	646	1,038	0,237	--	1281*	--	--	--	--
	802	0,937	--	--	--	--	--	--	--
	649	0,985	0,191	-0,234	1102 ²	1335 ²	--	--	--
	802	0,874	--	-0,861	--	533	--	1,109	--
	748	0,874	--	-0,634	--	676	--	1,207	--
	699	0,885	--	-0,436	--	970*	--	--	--
	649	0,933	--	-0,266	--	1552*	--	--	--
	801	0,916	0,502	-0,732	454	553	0,701	1,17	--
	747	0,951	0,39	-0,543	637	735	0,628	1,269	--
	699	0,967	0,291	-0,377	851*	868*	--	--	--
649	0,928	0,181	-0,232	1167*	1367*	--	--	--	
9M0997	798	0,978	0,565		480		0,732		
	752	1,013	0,461		596		0,677	--	
	701	1,026	0,324		805*		--	--	
	800	0,936	0,414	-0,614	560	665	0,653	1,222	
	747	0,952	0,331	-0,458	725*	739*	--	--	
	699	0,968	0,161*	-0,33	--	1116*	--	--	
	648	0,984	0,148	-0,203	1344*	1600*	--	--	
	799	0,853	--	-0,699	--	693	--	1,166	
	748	0,869	--	-0,526	--	867	--	1,276	
	698	0,913	--	-0,365	--	1165*	--	--	
	649	0,931	--	-0,23	--	1849*	--	--	

Elektrochemische Kennwerte									
Proben- kennung	Temperatur	OCV	Strom- dichte @ 0.7 V	Strom- dichte @ 1.2 V	ASR @ 0.5A/cm ²	ASR @ -0.5A/cm ²	Spannung @ 0.5 A/cm ²	Spannung @ -0.5 A/cm ²	Grenz- strom- dichte
	[°C]	[V]	[A/cm ²]	[A/cm ²]	[mΩ·cm ²]	[mΩ·cm ²]	[V]	[V]	[A/cm ²]
9M1001	799	1,002	0,672	--	388		0,767	--	--
	750	1,014	0,461	--	552		0,678	--	--
	702	1,027	0,281	--	809*		--	--	--
	645	0,938	0,134	--	1276*		--	--	--
	802	0,938	0,494	-0,698	403	551	0,697	1,192	--
	747	0,954	0,334	-0,475	644	735*	0,591	--	--
	699	0,917	0,195	-0,305	967*	1201*	--	--	--
	648	0,987	0,071*	-0,177	--	2242*	--	--	--
	801	0,858	--	-0,787	--	561	--	1,147	--
	747	0,869	--	-0,545	--	722	--	1,269	--
	699	0,866	--	-0,361	--	1215*	0,767	--	--
648	0,839	--	-0,222	--	2121*	0,678	--	--	

*extrapoliert

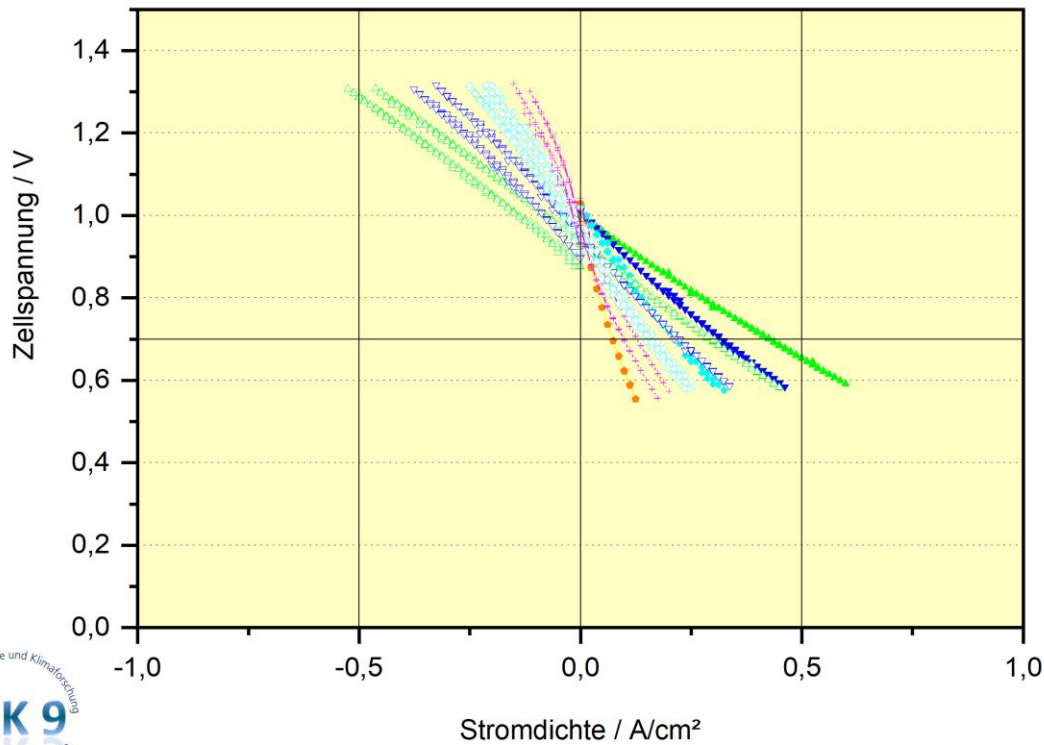
**mit 50% Befeuchtung

² Wert maskiert

Wert nicht bestimmt, wegen abweichender Befeuchtung

SOFC Zelle 15770-6 Messung Nr:9M0981
 Projekt: F & E

Kennlinien



Kathodenmaterial: LCF 82
 Zelle: 15770-6
 Startdatum: 20.08.2020
 Prüfstand: MP08
 Gehäuse: Al₂O₃
 Anodenkontakt: Ni- Netz
 Kathodenkontakt: Pt- Netz
 Dichtung: Gold 0,89 mm

aktive Fläche: 40 x 40 mm²
 Elektrolytdicke: 10 µm
 Funktionsschichtdicke: 105 µm Kathode

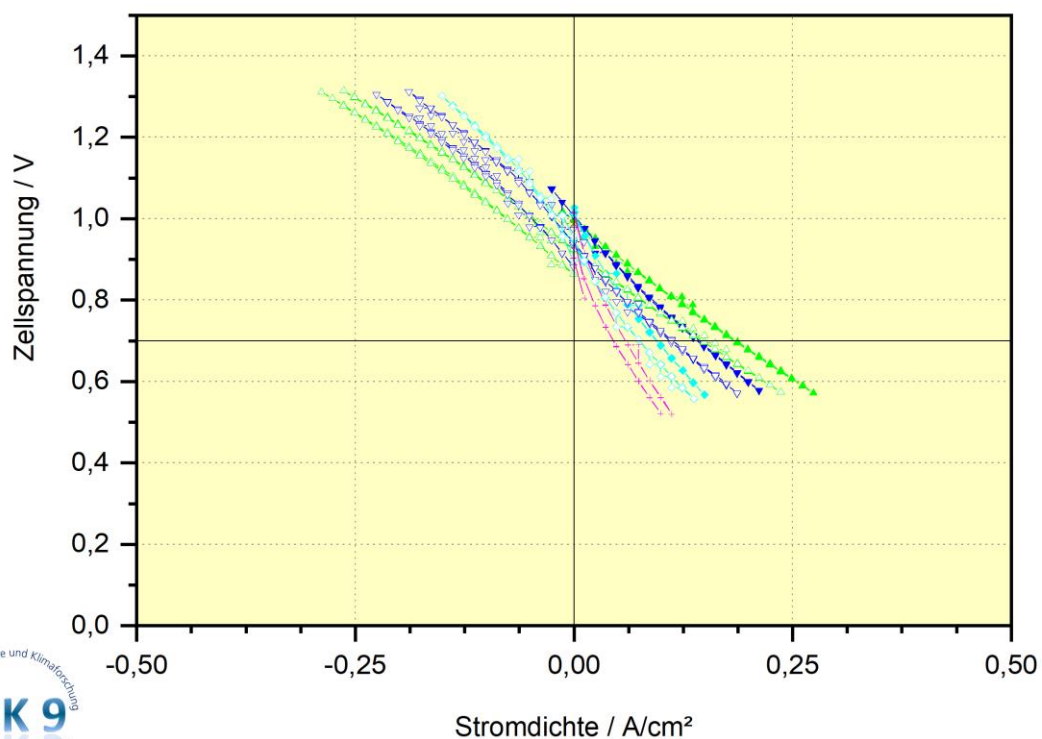
	T °C	H ₂	N ₂ Nl/h	FG	H ₂ O	Luft
—●—	800	60	0	0	15	120
—▲—	750	60	0	0	15	120
—◆—	700	60	0	0	15	120
—◇—	647	60	0	0	15	120
—●—	602	60	0	0	15	120
—◇—	802	60	0	0	60	120
—◇—	747	60	0	0	60	120
—◇—	700	60	0	0	60	120
—◇—	651	60	0	0	60	120
—◇—	801	15	0	0	60	120
—◇—	748	15	0	0	60	120
—◇—	700	15	0	0	60	120
—◇—	650	15	0	0	60	120

TB, IEK-9/HTEC
 9M0981.OPJ. neuKennlinie
 20.10.2020



SOFC Zelle 15770_7 Messung Nr:9M0985
 Projekt: F & E

Kennlinien



Kathodenmaterial: LSFC
 Zelle: 15770_7
 Startdatum: 27.08.2020
 Prüfstand: MP08
 Gehäuse: Al₂O₃
 Anodenkontakt: Ni- Netz
 Kathodenkontakt: Pt- Netz
 Dichtung: Gold 0,89 mm

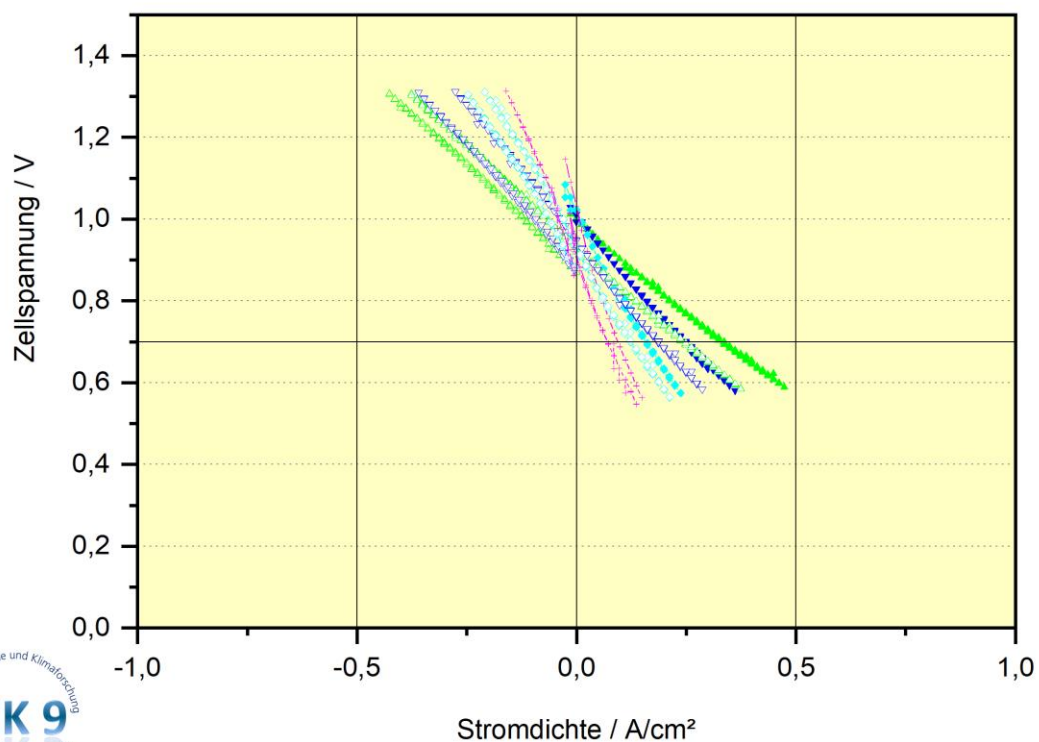
aktive Fläche: 40 x 40 mm²
 Elektrolytdicke: 10 µm
 Funktionsschichtdicke: 125 µm

	T °C	H ₂	N ₂	FG NI/h	H ₂ O	Luft
—▲—	804	61	0	0	15	120
—▼—	749	61	0	0	15	120
—◆—	699	61	0	0	15	120
—◇—	650	61	0	0	15	120
—○—	602	61	0	0	15	120
—◊—	801	61	0	0	59	120
—◊—	747	61	0	0	60	120
—◇—	700	61	0	0	59	120
—◇—	649	61	0	0	59	120
—◇—	801	16	0	0	59	120
—◇—	747	16	0	0	60	120
—◇—	699	16	0	0	58	120
—◇—	649	16	0	0	60	120

TB, IEK-9/HTEC
 9M0985.OP.J, neuKennlinie
 20.10.2020

SOFC Zelle 15775-4 Messung Nr:9M0992
 Projekt: F & E

Kennlinien



Kathodenmaterial: LCFC 8282
 Zelle: 15775-4

Startdatum: 19.09.2020
 Prüfstand: MP08
 Gehäuse: Al₂O₃
 Anodenkontakt: Ni- Netz
 Kathodenkontakt: Pt- Netz
 Dichtung: Gold 0,88 mm

aktive Fläche: 40 x 40 mm²
 Elektrolytdicke: 10 µm
 Funktionsschichtdicke: 69 µm Kathode

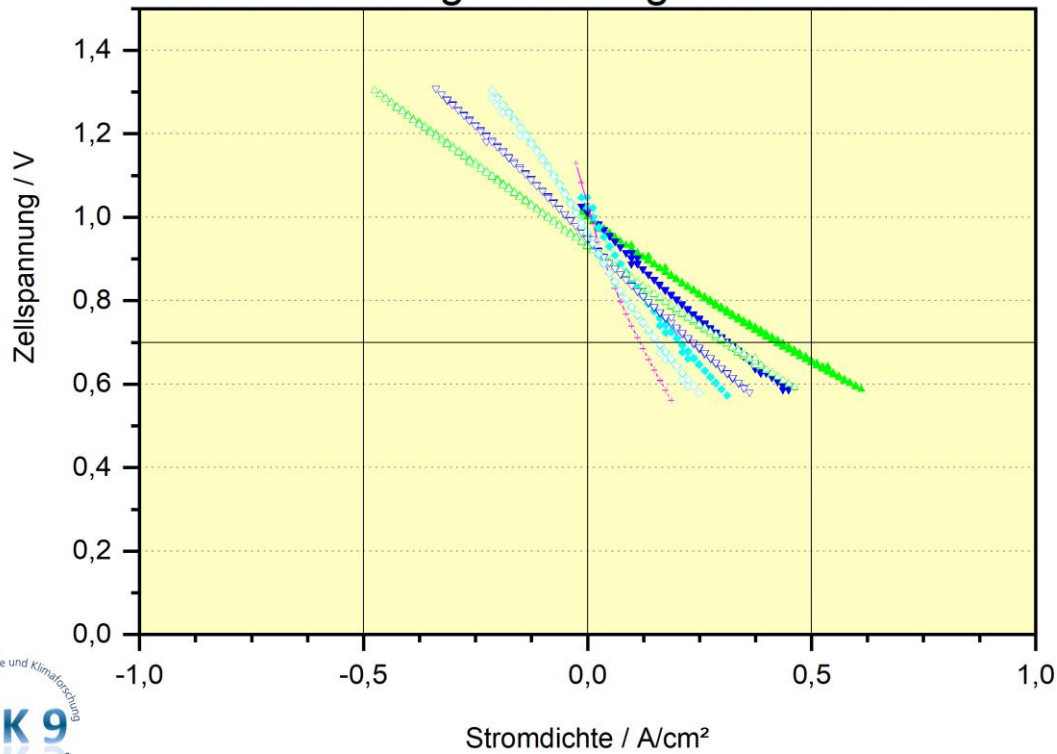
	T °C	H ₂	N ₂	FG	H ₂ O	Luft
		Nl/h				
—▲—	799	61	0	0	15	120
—▼—	750	61	0	0	15	120
—◆—	701	61	0	0	15	120
—◇—	646	61	0	0	15	120
—◇—	800	61	0	0	60	120
—◇—	800	61	0	0	60	120
—◇—	747	61	0	0	59	120
—◇—	699	61	0	0	59	120
—◇—	649	61	0	0	59	120
—◇—	800	16	0	0	60	120
—◇—	748	16	0	0	60	120
—◇—	699	16	0	0	59	120
—◇—	648	16	0	0	59	120

TB IEK-9/HTEC
 9M0992.OPJ_neuKennlinie
 20.10.2020



SOFC Zelle 15775_7 Messung Nr:9M0993
 Projekt: F & E

Kennlinien
 Datenaufzeichnungsschwierigkeiten ab 01.10.2020



Kathodenmaterial: LCSF 622
 Zelle: 15775_7
 Startdatum: 28.09.2020
 Prüfstand: MP08
 Gehäuse: Al₂O₃
 Anodenkontakt: Ni- Netz
 Kathodenkontakt: Pt- Netz
 Dichtung: Gold 0,88mm

aktive Fläche: 40 x 40 mm²
 Elektrolytdicke: 10 µm
 Funktionsschichtdicke: 73 µm

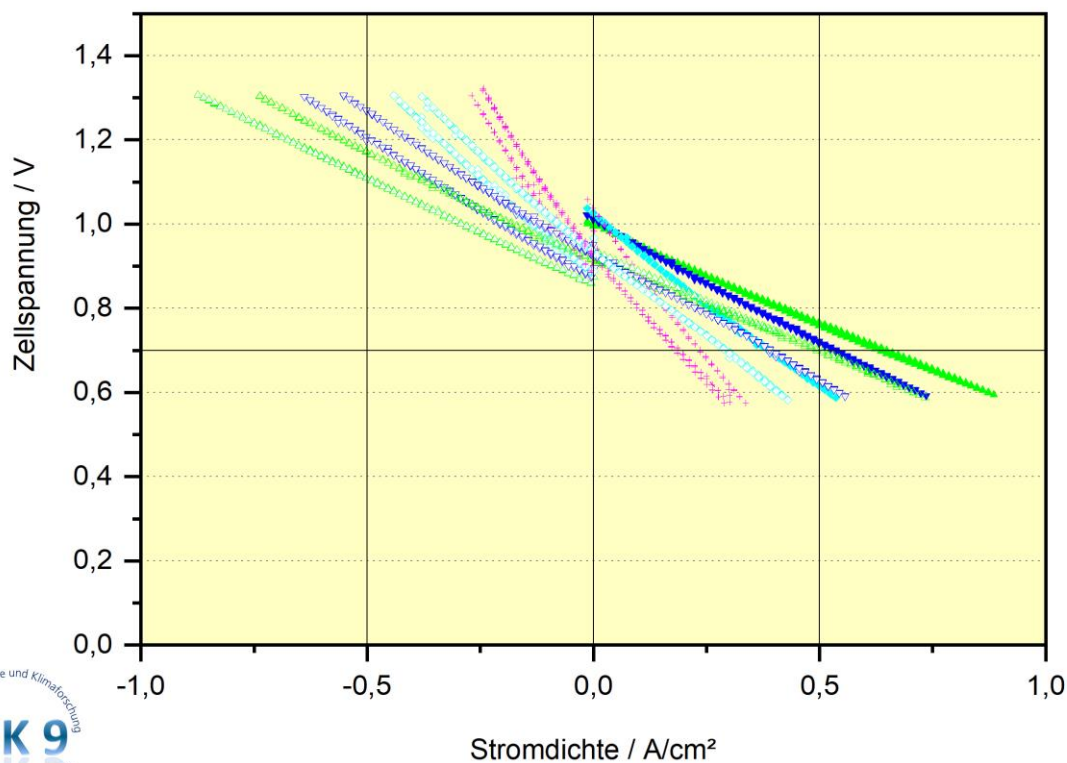
	T	H ₂	N ₂	FG	H ₂ O	Luft
	°C			Nl/h		
—▲—	799	61	0	0	15	120
—▼—	750	61	0	0	15	120
—◆—	701	61	0	0	15	120
—▲—	646	61	0	0	15	120
—▲—	803	61	0	0	59	120
—▲—	746	61	0	0	59	120
—▲—	700	700	0	0	59	120

TB, IEK-9/HTEC
 9M0993.OPJ, neuKennlinie
 20.10.2020



SOFC Zelle 15775-5 Messung Nr:9M0995
 Projekt: F & E

Kennlinien



Kathodenmaterial: LCSF 622
 Zelle: 15775-5
 Startdatum: 06.10.2020
 Prüfstand: MP08
 Gehäuse: Al₂O₃
 Anodenkontakt: Ni- Netz
 Kathodenkontakt: Pt- Netz
 Dichtung: Gold 0,87-0,88 mm

aktive Fläche: 40 x 40 mm²
 Elektrolytdicke: 10 µm
 Funktionsschichtdicke: 53 µm

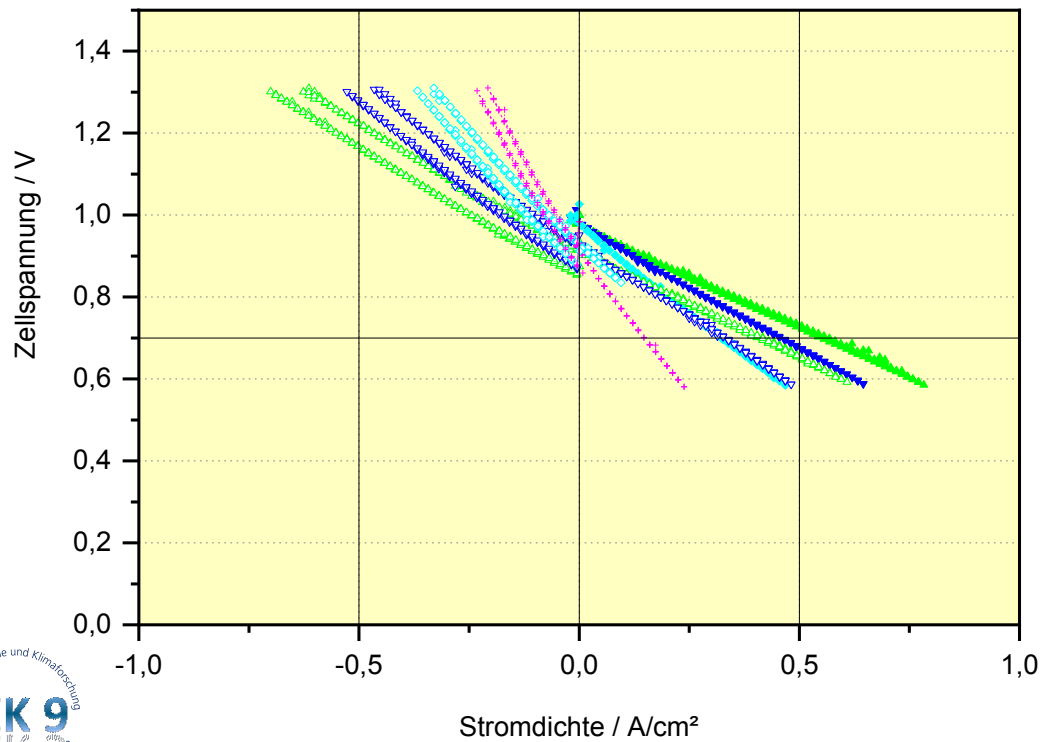
	T °C	H ₂	N ₂	FG	H ₂ O	Luft
—▲—	799	799	0	0	15	120
—▼—	750	61	0	0	15	120
—◆—	700	61	0	0	15	120
—▲—	646	61	0	0	15	120
—▲—	802	61	0	0	59	120
—▲—	649	61	0	0	59	120
—▲—	802	16	0	0	60	120
—▲—	748	16	0	0	59	120
—▲—	699	16	0	0	60	120
—▲—	649	16	0	0	60	120
—▲—	801	61	0	0	60	120
—▲—	747	61	0	0	59	120
—▲—	699	61	0	0	59	120
—▲—	649	61	0	0	59	120

TB IEK-9/HTEC
 9M0995.OP1, neuKennlinie
 20.10.2020



SOFC Zelle 15775-6 Messung Nr:9M0997
 Projekt: F & E

Kennlinien



Kathodenmaterial: LCSF622
 Zelle: 15775-6
 Startdatum: 17.10.2020
 Prüfstand: MP08
 Gehäuse: Al₂O₃
 Anodenkontakt: Ni- Netz
 Kathodenkontakt: Pt- Netz
 Dichtung: Au 0,87-0,88 mm

aktive Fläche: 40 x 40 mm²
 Elektrolytdicke: 10 µm
 Funktionsschichtdicke: 61 µm Kathode

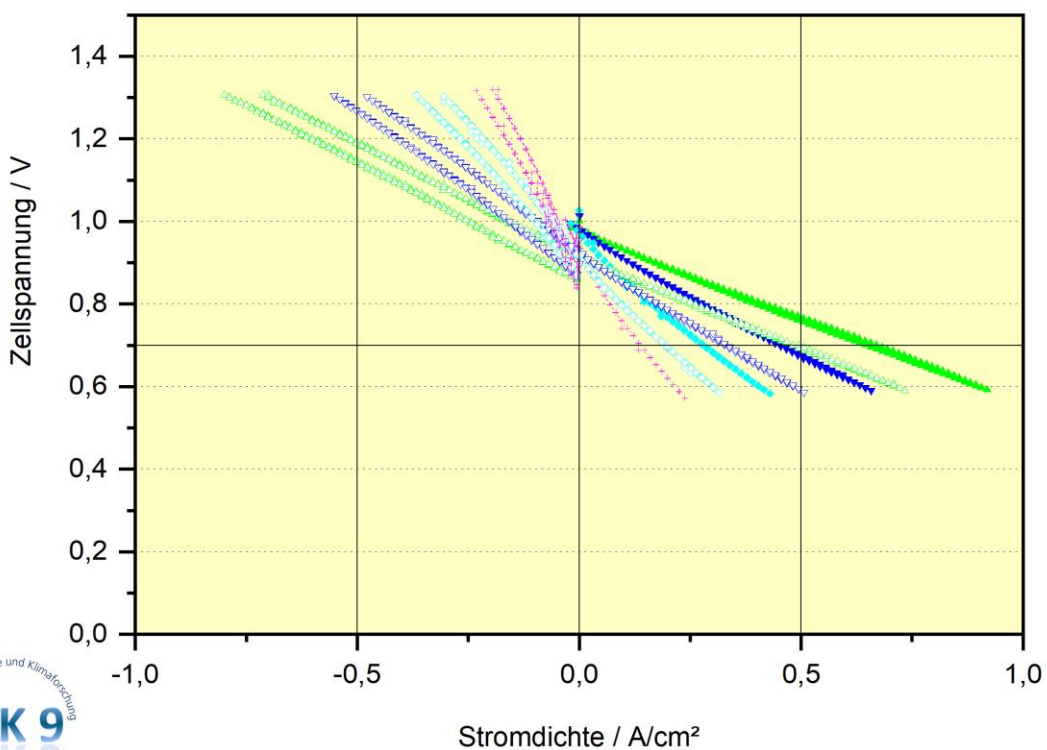
	T °C	H ₂	N ₂	FG	H ₂ O	Luft
—▲—	798	61	0	0	15	120
—▼—	752	61	0	0	15	120
—◆—	701	61	0	0	15	120
—△—	800	61	0	0	59	120
—▽—	747	61	0	0	59	120
—◇—	699	61	0	0	59	120
—+—	648	61	0	0	59	120
—△—	799	16	0	0	60	120
—▽—	748	16	0	0	59	120
—◇—	698	16	0	0	60	120
—+—	649	16	0	0	59	120

CT, IEK-9/HTEC
 9M0997_OPJ_neuKennlinie
 02.11.2020



SOFC Zelle 15775-8 Messung Nr:9M1001
 Projekt: F & E

Kennlinien

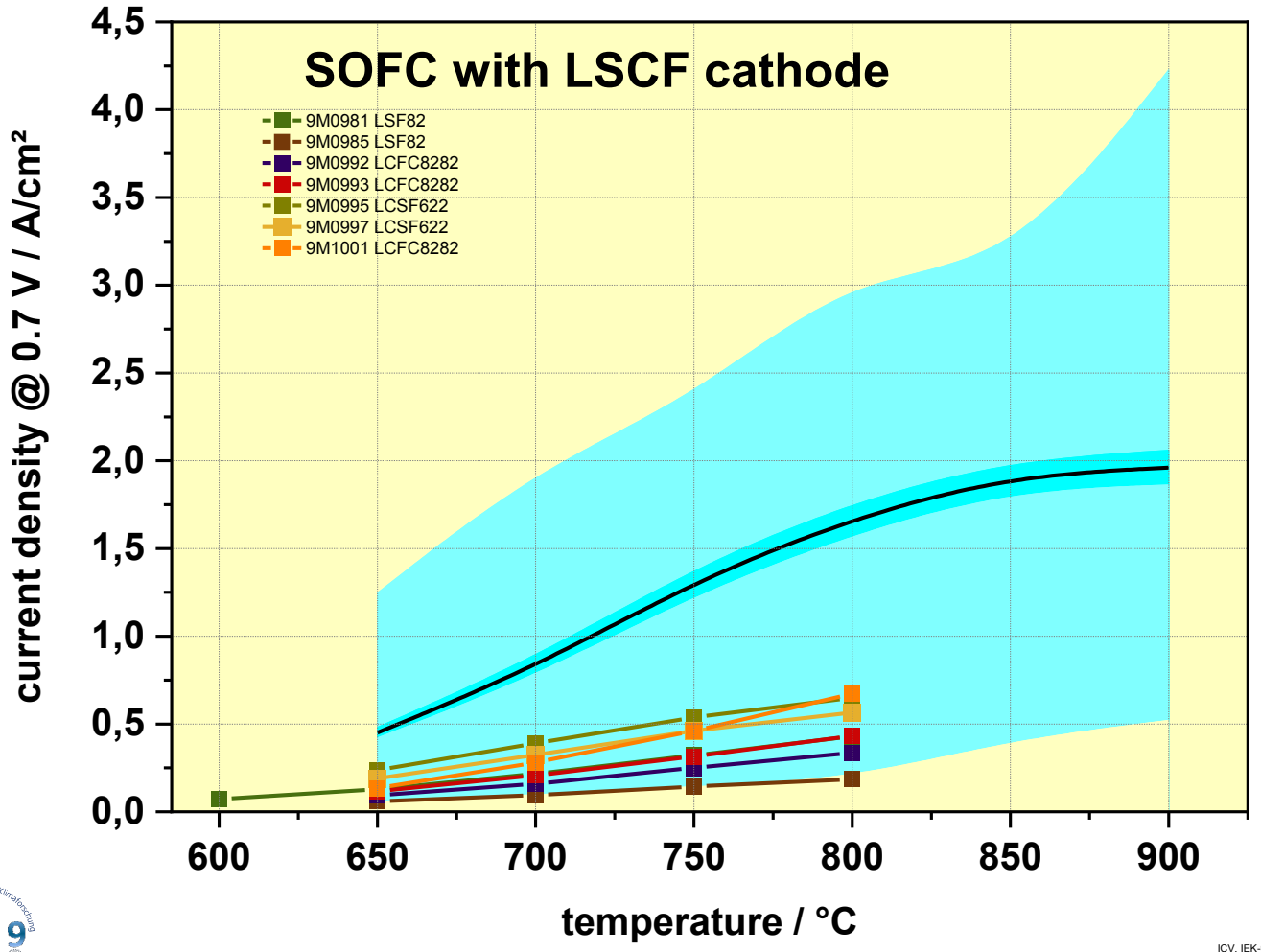


Kathodenmaterial: LFC8282
 Zelle: 15775-8
 Startdatum: 29.10.2020
 Prüfstand: MP08
 Gehäuse: Al₂O₃
 Anodenkontakt: Ni- Netz
 Kathodenkontakt: Pt- Netz
 Dichtung: Gold 0, 89 mm

aktive Fläche: 40 x 40 mm²
 Elektrolytdicke: 10 µm
 Funktionsschichtdicke: 87 µm Kathode

	T °C	H ₂	N ₂	FG Nl/h	H ₂ O	Luft
—▲—	799	61	0	0	15	120
—▼—	750	61	0	0	15	120
—◆—	702	61	0	0	15	120
—◇—	645	61	0	0	15	120
—○—	802	61	0	0	59	120
—◇—	747	61	0	0	59	120
—◇—	699	61	0	0	59	120
—◇—	648	61	0	0	59	120
—◇—	801	16	0	0	59	120
—◇—	747	16	0	0	59	120
—◇—	699	16	0	0	59	120
—◇—	648	16	0	0	59	120

TB, IEK-9/HTEC
 9M1001.OPJ, neuKennlinie
 11.11.2020



ICV, IEK-9/HTEC
LSFC_CS-TB.OPJ, Graph2
16.11.2020

